12-2021

Interplay Between the Lattice and Spin Degrees of Freedom in Magnetoelectric and Magnetic Materials

Temuujin Bayaraa
University of Arkansas, Fayetteville

Interplay Between the Lattice and Spin Degrees of Freedom in Magnetoelectric and Magnetic Materials

This dissertation is submitted in partial fulfillment
of the requirements for the degree of
Doctor of Philosophy in Physics

by

Temuujin Bayaraa
National University of Mongolia
Bachelor of Science in Nuclear Technology, 2012
University of Arkansas
Master of Science in Physics, 2018

December 2021
University of Arkansas

This dissertation is approved for recommendation to the Graduate Council.

Laurent Bellaiche, Ph.D.
Dissertation Director

William (Lin) Oliver, Ph.D.
Committee Member

Sergey Prosandeev, Ph.D.
Committee Member

Hugh Churchill, Ph.D.
Committee Member

Abstract

This dissertation contains several investigations on the cross-coupling between structural and spin degrees of freedom in multiferroic and ferrimagnetic compounds by means of first-principles calculations and *ab-initio*-based Monte-Carlo simulations. We start with the reviews of magnetoelectricity, ferrimagnetism, strain engineering, followed by a brief introduction to first-principles computational methods, magnetic effective Hamiltonians, and other techniques that are utilized here. The results section of the dissertation can be divided into two parts. The first half focuses on magnetoelectric effects arising from different sources, while the second half is about the ferrimagnetic nature of materials. In the first part, we examine the epitaxial strain effect on magnetoelectric coupling through lattice mediation and study the underlying mechanism behind the magnetic domain-wall-induced magnetoelectric effect in a non-polar cubic structure. Through the investigation of epitaxial strain effect in the multiferroic $Sr_{0.5}Ba_{0.5}MnO_3$ compound, a large enhancement of linear magnetoelectric coupling coefficient was found at the edge of the so-called morphotropic phase boundary. Such enhancement was studied (at the microscopic level) and found to be related to the large enhancement in the electric susceptibility tensor at this morphotropic phase boundary. Furthermore, we investigate the magnetoelectric effect arising from the magnetic domain wall in Rare-earth Iron Garnet systems. Our results reveal that such domain-wall induced magnetoelectric effect neither requires the existence of magnetism at the rare-earth sites nor non-collinear magnetism to exist, which is in contrast to what was previously proposed in various studies. It is rather found to originate from a (magnetoelectric) symmetric exchange-striction mechanism involving ferromagnetic interactions between two different iron sublattices at the domain wall. In the second half, we study the epitaxial strain effect on magnetic properties (e.g. the magnetization compensation temperature) of ferrimagnetic Rare-earth Iron Garnets and investigate magnetic and topological properties of anti-perovskite ferrimagnet Mn_4N. The introduction of the epitaxial strain effect in Rare-earth Iron Garnets

is found to significantly affect its magnetic properties and our results reveal that one can tune the magnetization compensation temperature to be at room temperature using a common substrate, which is beneficial for application purposes. Furthermore, our study on the anti-perovskite ferrimagnet Mn_4N shows that there is a previously overlooked magnetization compensation temperature in this system and nano-metric sized topological states were also identified from our simulations. Such topological states were found to be stabilized by frustrated exchange coupling interactions between long-distance Mn pairs.

Acknowledgements

I still remember the days of excitement when I received a Fulbright scholarship to study for my Master's degree in the USA. And there was also some fear that I would be walking into something that was unknown to me. At the start of my journey, I remember falling into despair when I found out that my physics knowledge was no way near the minimum for the graduate courses and to do fundamental research. But as a famous Mongolian proverb says "Эзэн хичээвэл, заяа хичээнэ" which roughly translates to "Life provides to those who strive", all is wonderful at the end of this journey of mine. There are many people whom I am very thankful for and would like to acknowledge.

First, I would like to express my sincere gratitude to my advisor, Dr. Laurent Bellaiche, for his lessons, guidance, willingness to help, and providing me with an excellent environment to learn, get motivated, and collaborate. His understanding, modest, gentle, and overall professional characteristics guided and inspired me to understand how to be a physicist and a respectful, humble person. This work has not been possible without his patience, encouragement, time, creative ideas, guidance, and knowledge. I really appreciate all the things he has done for me and his trust, and for giving me the freedom to explore on my own and at my own pace. He is always encouraged me to attend workshops, conferences which ultimately lead me to become a better listener and presenter. I am always amazed by his productivity and fast responses to my questions even though he has a large academic research group to lead which inspired me, even more, to learn from him.

I am forever thankful to my family for their unyielding support, care, and belief in me. I am extremely grateful for my beloved wife and son for the understanding nature, support, and joys they provided to me during the hard times.

I am also thankful to all the research group members for their encouragement and comments during my talks and would like to express my sincere gratitude to my postdoc fellows, Dr. Yurong Yang, Dr. Charles Paillard, Dr. Hongjian Zhao, and Dr. Changsong Xu, for

their time, teachings and inspirations. Furthermore, my many thanks to my fellow friends and graduate students for their time, laughter, companionship, and encouragements.

I thank my committee members, Dr. William Oliver Lin, Dr. Sergey Prosandeev, and Dr. Hugh Churchill, for their time, great questions, and feed-backs.

Dedication

For my beloved parents and family

Contents

List of Tables

List of Figures

List of Published Papers

Large parts of Chapters 3, 4, 5 and 6 were originally published as follows and copyright information can be found in Appendix.

- (Chapter 3) Bayaraa, T., Yang, Y., Ye, M., and Bellaiche, L. (2021). Giant linear magnetoelectric effect at the morphotropic phase boundary of epitaxial $Sr_{0.5}Ba_{0.5}MnO_3$ films. Physical Review B, 103(6), L060103.

- (Chapter 4) Bayaraa, T., Xu, C., Yang, Y., Xiang, H., and Bellaiche, L. (2020). Magnetic-Domain-Wall-Induced Electrical Polarization in Rare-Earth Iron Garnet Systems: A First-Principles Study. Physical Review Letters, 125(6), 067602.

- (Chapter 5) Bayaraa, T., Xu, C., Campbell, D., and Bellaiche, L. (2019). Tuning magnetization compensation and Curie temperatures in epitaxial rare earth iron garnet films. Physical Review B, 100(21), 214412.

- (Chapter 6) Bayaraa, T., Xu, C., and Bellaiche, L. (2021). Magnetization compensation temperature and frustration-induced topological defects in ferrimagnetic antiperovskite Mn_4N. Physical Review Letters, 127(21), 217204 (2021).

1 Introduction

1.1 Introduction

Magnetism and electricity are two fundamental physical phenomena that led to the broad technological evolution toward the modern human civilization. Even today, they remain at the frontier of the scientific exploration and still attract considerable amount of attention within the scientific community for their indispensable scientific value in both theory and application. In solids, electricity and magnetism originate from the charge degrees of freedom and the spin of the electrons, respectively. The cross-coupling between these two fascinating phenomena is highly desirable since it may solve the difficulties with generating a large magnetic field and the problems with heat generations by electron scattering. However, such cross-coupling is not trivial due to the fact that in most magnetic materials, the magnetic moment originates from unpaired electrons in partially occupied d orbitals and/or f orbitals but the spontaneous electric polarization usually needs empty d orbitals as a condition of having a coordinate bond (dipole-dipole interaction). Furthermore, the strain can also couple with the polarization and magnetization which leads to various cross-couplings including some shown in Figure 1.1. Such cross-coupling between polarization, magnetization and strain brings to the rich interplay between charge, spin, lattice and orbital orders. In this dissertation, our motivation is to study and understand the interplay between the lattice and spin degrees of freedom in magnetoelectric and magnetic materials. In this chapter, important fundamental understandings are covered.

1.2 Multiferroicity and Magnetoelectricity

Multiferroics simultaneously possess two or more primary ferroic orders, such as (anti)ferromagnetic, ferroelectric, ferroelastic and ferrotoroidic orders [10]. Cross-coupling among these orders would result in new properties, paving the way to realizing cross-control of various ordered

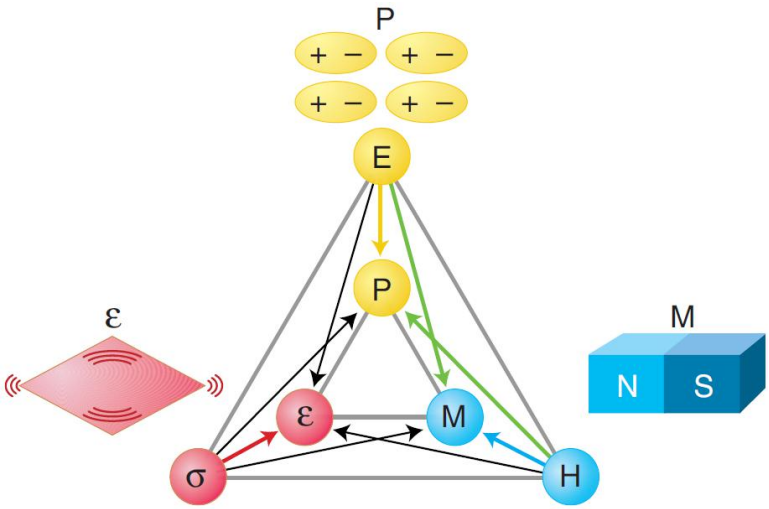

Figure 1.1: The cross coupling between polarization, magnetization, and strain. The electric field **E**, magnetic field **H**, and stress σ control the electric polarization **P**, magnetization **M**, and strain ε, respectively. The figure is taken from [1].

parameters. The most compelling and enticing of such cross-control is the switching of the magnetization via electric field or *vice versa*, ferroelectric polarization via magnetic field - magnetoelectric effect. In general, magnetoelectric effects can exist/develop in many systems, even in some nonmagnetic systems. However, most systems with magnetoelectric effects are found to be not applicable (too small) for practical use but multiferroics seem to be the best playground for finding one.

Since their discovery in the 1960s, multiferroic materials have constantly attracted attention and, it became even more enticing since the publication of the two seminal papers on $TbMnO_3$ and $BiFeO_3$ in 2003 [11, 12]. Since then, a large number of materials have been studied to show multiferroicity and magnetoelectric coupling, and these materials can be roughly classified into categories according to the microscopic mechanisms and Eerenstein *et al.* [2] show the relationship and overlap of the multiferoic and magnetoelectric materials in Figure 1.2.

Magnetoelectric (ME) materials are of fundamental interest and promising for advanced electronic technological applications. The search for materials displaying a large ME effect is still a hot topic even though the discovery of ME effect was accomplished at the end of

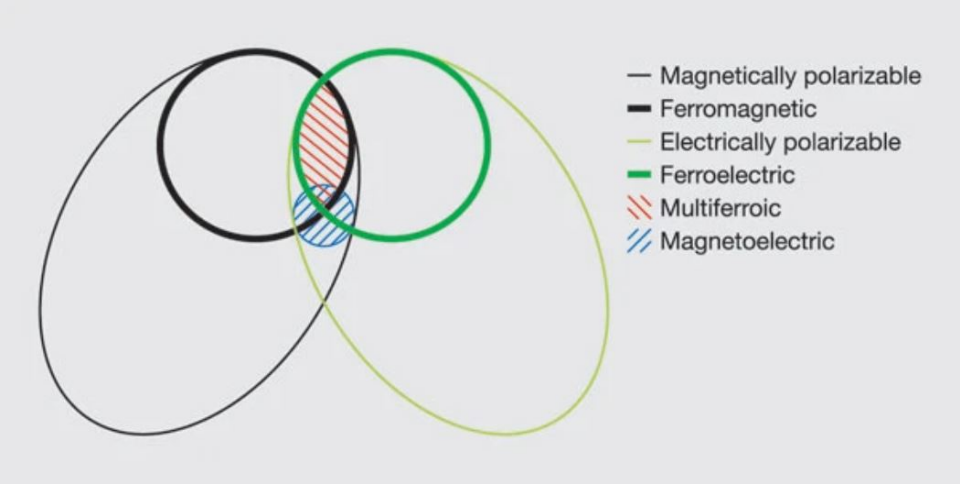

Figure 1.2: The relationship between multiferroic and magnetoelectric materials. The figure is taken from [2].

the 19th century.

ME effect describes the coupling between electricity and magnetism: the electric polarization **P** (magnetization **M**) responds to an applied magnetic field **H** (applied electric field **E**) [13]. Since it is a coupling between **E** and **H**, ME effect is the lowest order coupling between them in the free energy:

$$F = F_0 - \frac{1}{2}k_{ij}E_iE_j - \frac{1}{2}\chi_{ij}H_iH_j - \alpha_{ij}E_iH_j \tag{1.1}$$

where i, j are spatial directions, k and χ are the dielectric and magnetic susceptibility, respectively, and α is the linear magnetoelectric tensor. More precisely, the linear ME tensor α is defined as

$$\alpha_{ij} = \left(\frac{\partial P_i}{\partial H_j}\right)_E = \mu_0 \left(\frac{\partial M_i}{\partial E_j}\right)_H \tag{1.2}$$

where μ_0 is the vacuum permeability, and it can be written as the sum of three (electronic, ionic and strain) terms:

$$\alpha = \alpha^{ion} + \alpha^{elec} + \alpha^{strain} \tag{1.3}$$

where the first term is ionic contribution, the second electronic and last term the strain-mediated ME responses, respectively. Furthermore, if we consider that magnetization can have spin and orbital origins, α can be written as the sum of six terms (see Figure1.3).

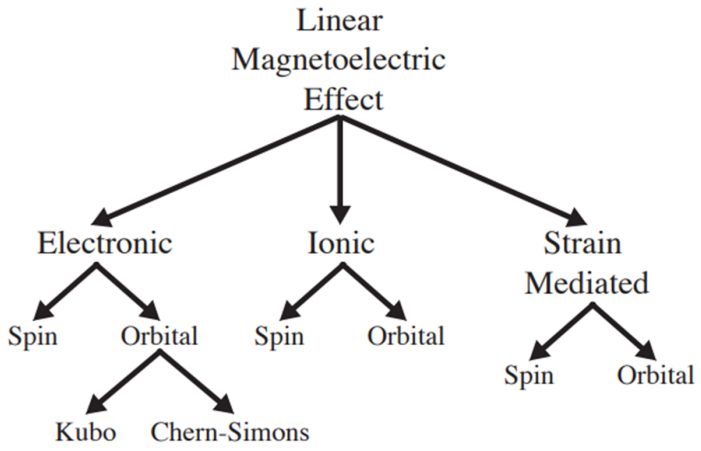

Figure 1.3: Different contributions to the linear ME coefficient at 0K.

Recently, five of six terms have become accessible from first-principles calculations: electronic contribution from spin and orbital origins, ionic contributions from spin and orbital origins and strain-mediated contribution from spin origin.

The first development of the first-principles methodologies to compute α tensor was done by Iniguez [14] on the ionic contribution to the α tensor from spin origin α_s^{ion} assuming it is the dominant term. Afterward the method was extended to include the strain contribution [15], and the α tensor in Eq. (1.3) from spin origin was found as

$$\alpha_{ij,S} = \alpha_{ij,S}^{elec} + \Omega_0^{-1}\mu_0 Z_{mi}^{e}(K^{-1})_{mn}Z_{nj}^{m} + e_{im}(C^{-1})_{mn}h_{jn} \tag{1.4}$$

where Ω_0 is the unit cell volume, Z^e is the dynamical Born electric charge, K^{-1} is the inverse force-constant matrix, Z^m is the dynamical magnetic charge, e_{im} and h_{jn} are the piezoelectric and piezomagnetic tensors, and $(C^{-1})_{mn}$ is the inverse of the elastic constants matrix. Eq. (1.4) provides an insight into the microscopic origin of the ionic and strain contribution to the ME tensor α.

Alternatively, Bousquet *et al.* proposed a different approach for calculating the α tensor [16] which we utilized to compute α tensor in our work and more details about this method can be found in the Methods section of this dissertation. This method made the calculation of

the electronic contribution to the α coefficient achievable from first principles, although in the multiferroics, ionic contribution is expected to dominate over other terms.

The calculation of α coefficients due to orbital magnetic response from first principles was done slightly later than that of the spin magnetization thanks to recent developments in the modern theory of magnetization [17–19]. Using this theory, α_o^{elec} and α_o^{ion} was computed for Cr_2O_3 [20] and α_o^{ion} was computed for $LiFePO_4$ [21]. However, α_o^{strain} has not yet been evaluated from first-principles calculations probably because of the technical difficulty in extracting such subtle response.

All the above findings are at 0K and as the temperature increases, spins fluctuate and give rise to a so-called exchange-striction mechanism. Mostovoy *et al.* studied this on Cr_2O_3 using a combination of Density Functional Theory (DFT) calculations and Monte Carlo (MC) simulations [22]. They reported that the exchange-striction mechanism can induce a large ME response and it is one order higher than ME response from spin-orbit origin at a given temperature. Also, for $BiFeO_3$ (BFO), the calculation of linear and non-linear ME coefficients at a finite temperature and the origin of the spin spiral was done in the framework of an effective Hamiltonian [23, 24].

The enhancement of linear ME effect was studied by Wojdel and Iniguez using the idea of "structural softness" (strain influence) in their first-principles study of ME effect in compressively strained BFO films [25]. They report that the compound becomes structurally soft with large ME response near the region of critical strain and structural softness also occurs within the isosymmetric transition region between rhombohedral and tetragonal phases of BFO films. Such enhancement in ME coefficients near such phase transition was also reported in the second-principles study of Prosandeev et al. and compressive strain is also expected to significantly enhance the quadratic ME coupling in $BiFeO_3$ films. Furthermore, the linear and quadratic ME coefficients were studied via general phenomenological model and the linear ME coefficient was found as

$$\alpha_{ij} = \alpha_{ij}^{(1)} + \alpha_{ij}^{(2)} \tag{1.5}$$

with

$$\alpha_{ij}^{(1)} = -4\varepsilon_0 \sum_{pq} \lambda_{pq} P_p \chi_{pi}^{P} M_q \chi_{qi}^{M} \tag{1.5.1}$$

$$\alpha_{ij}^{(2)} = -\sum_{pqr} g_{pqr} \chi_{ri}^{P} L_q \chi_{pj}^{M} \tag{1.5.2}$$

where λ_{pq} and g_{pqr} being second and third-rank tensors that are dependent on the material by itself but also on the symmetry of the crystal. M_q, P_p and L_q are the q, p, and r-component of magnetization, polarization, and the antiferromagnetic vector, respectively. ε_0 is the dielectric permittivity of vacuum, and χ_{pi}^{P} and χ_{qj}^{M} are elements of the dielectric and magnetic susceptibility tensors, respectively. Equations (1.5.1) and (1.5.2) show that the linear ME coefficient can only manifest in structural states that are magnetically ordered and for ferromagnetic and anti-ferromagnetic systems, only non-zero components are $\alpha_{ij}^{(1)}$ and $\alpha_{ij}^{(2)}$, respectively. However, if there is a weak ferromagnetism that coexists with a strong antiferromagnetic vector in a spin-canted magnetic structures (e.g BFO films below 640K), both term can simultaneously be activated.

1.3 Ferrimagnets

Magnetic properties of materials can be understood by the existence of orbital and spin magnetic moments of electrons. Interactions between electrons are the basis behind the macroscopic ordering that has various behaviors when external magnetic field is applied to them. Generally, magnetic properties of materials are characterized by their magnetization M and magnetic susceptibility χ,

$$M = \frac{m}{V} \tag{1.6}$$

$$\chi = \frac{M}{H} \tag{1.7}$$

where m is the magnetic moment, V is volume, H is the magnetic field. The variation of these parameters with respect to the temperature ($M(T), \chi(T)$) and external magnetic field ($M(H)$) is studied and used to describe the magnetic properties of various materials.
In general, magnetic materials are differentiated on how strongly the magnetic moments are interacting and if there is any collective interaction between each other. Magnetic materials are classified into a few major groups depending on their magnetic properties (see Figure 1.4):

- Diamagnetism - a weak magnetism which is characteristic to materials with no magnetic moments
- Paramagnetism - a randomly arranged unpaired electrons
- Ferromagnetism - all parallelly aligned unpaired electrons
- Antiferomagnetism - all anti-parallelly aligned unpaired electrons with zero net magnetization
- Ferrimagnetism - all anti-parallelly aligned unpaired electrons with non-zero net magnetization (due to an inequality in the magnitude of the magnetic moments in each orientation)

Diamagnetic and paramagnetic materials exhibit no collective magnetic interactions and show no ordering, thus considered as "non-magnetic". In contrast, materials with ferromagnetic, antiferromagnetic, and ferrimagnetic properties exhibit a long-range magnetic ordering below a certain critical temperature and usually considered as magnetic materials.
Since spins of ferromagnets are aligned parallel to each other and provide a single magnetization vector, it can be manipulated using external stimuli such as magnetic fields and spin transfer from electrical currents. Such a property gives rise to a range of physical effects such as giant magnetoresistance [26–28], spin Hall [29] and Rashba–Edelstein effects [30, 31], thus making ferromagnets the focus of attention in the spintronics community (a field of study

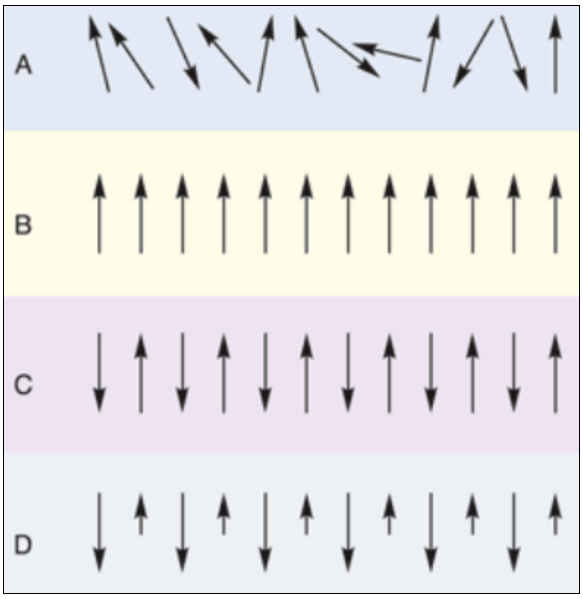

Figure 1.4: Types of magnetism. a) paramagnetism, b) ferromagnetism, c) antiferromagnetism, d) ferrimagnetism

with a goal of using the spin degree of freedom to create new devices which are superior to electronic devices [32]). However, ferromagnets are found to be not the ideal candidate due to fundamental limitations such as stray-field interactions and slow dynamics limiting the operating speed [33]. These stray fields are often the limiting factor in how small and densely packed magnetic bits can be in spintronic devices and the switching speed is usually governed by the underlying law of angular momentum conservation. Hence in order to increase the switching speed one can try to decrease the total angular momentum of the system which makes antiferromagnets the natural candidates to realize fast dynamics. Antiferromagnets are composed of magnetic sublattices with spins that are aligned antiparallel to each other which makes the net magnetization zero. On top of having faster dynamics, the reduced magnetization of the antiferromagnets makes the stray fields smaller thus leading to a smaller bit size and higher device density. Despite these advantages, the usage of antiferromagnets is limited due to the lack of mechanisms for realizing efficient reading and writing because antiferromagnets typically have a weaker response to magnetic fields which makes them hard to get perturbed by an external magnetic field [34].

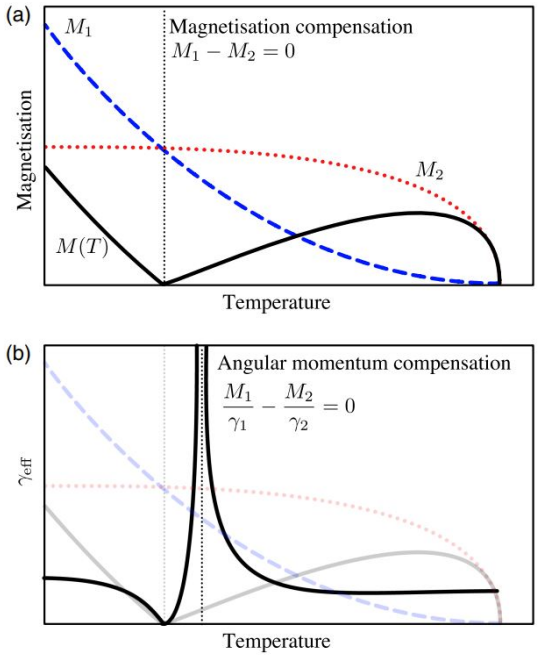

Figure 1.5: Diagram of the (a) magnetization and (b) angular momentum compensation points in ferrimagnets. M_1 and M_2 are the magnetisations of the antiparallel sublattices, which have different gyromagnetic ratios γ_1 and γ_2, respectively. Figure taken from [3]

On the other hand, ferrimagnetic materials were generally used because of its desirable material properties such as a low magnetic damping and high magneto-optical coupling. With time and a research progress, the unique properties of the ferrimagnets are getting exploited to overcome the drawbacks of ferromagnets and antiferromagnets in spintronics. Ferrimagnets have special properties or points in their phase diagram called magnetization and angular momentum compensation points. Since ferrimagnets have two sublattices that have different magnetization and alligned antiparallel to each other, there is a magnetization compensation point when $M_1(T) = M_2(T)$. Thus there is zero net magnetization since magnetization from the two sublattices cancel each other at that point (see Figure 1.5a). And, if the gyromagnetic ratios of two sublattices are different, the angular momentum compensation temperature is different from the magnetization compensation temperature, $\frac{M_1(T)}{\gamma_1} = \frac{M_2(T)}{\gamma_2}$ (see Figure 1.5b).

Such compensation points are getting exploited in order to impart the desirable properties

of both ferromagnets and antiferromagnets that are a measurable net magnetization and high speed dynamics, respectively. The hope is to investigate and exploit ferrimagnets in order to achieve ultrafast dynamics with the potential to overcome the gigahertz frequency limitations of ferromagnetic based technologies and realize terahertz spintronics [35, 36].

1.4 Strain engineering

Strain engineering refers to the mechanical deformation of a material for the purpose of improving one or more of its properties. In fact, the modern transistors are made using thin-film growth technologies that utilizes strain engineering. Thin films growth methods made a huge impact in decreasing the size of transistors to reach modern demand and other fields such as multiferroics and spintronics.

When stress is applied to a crystal lattice, the strain is observed as a change in lattice parameters. Strain can be defined as a ratio of change in the lattice parameter (due to stress, $\triangle a$) to the lattice parameter of the strain-free material (a_0): $\varepsilon = \triangle a/a_0$. Depending on the origin, the sources of strain can be internal and external. Internal sources can include a small lattice deformation due to the crystal imperfection such as vacancies. External sources of strain are usually taken as the lattice mismatch between the material and the substrate that the material grown on top of it. Also, external strain arises during cooling and heating due to having different thermal expansion coefficients for the material and substrate, and from applying mechanical stress by bending the film and substrate. A schematic of emergent strain engineering approaches is shown in Figure 1.6, which includes freestanding thin film, interface layer, nanostructure, growth conditions, thermal expansion mismatch,chemical doping, defect and ultrafast optical excitation induced strain.

Strain engineering can also modify the properties of multiferroic thin films. In fact, one of the groundbreaking findings of 2003 on multiferroics was a $BiFeO_3$ thin film grown by pulsed laser deposition technique [12] and a compressive strain on the tetragonal phase of $BiFeO_3$ with a c/a value of more than 1.25 is reported to possess a spontaneous polarization up

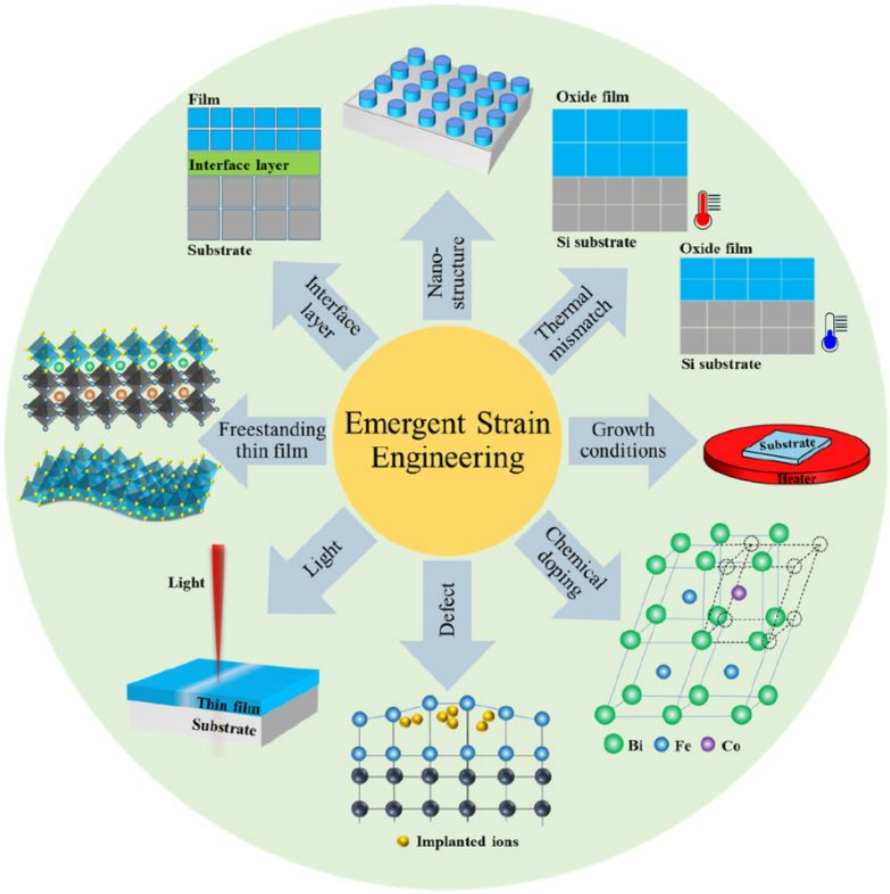

Figure 1.6: A schematic of emergent strain engineering approaches. Figure taken from [4]

to 150 $\mu C/cm^2$ [37–40]. Furthermore, strain engineering can increase the superconducting, ferroelectric, or ferromagnetic transition temperatures, and it can also induce ferroelectric or ferromagnetic states in materials where these features are not present in the bulk [41–44].

1.5 Outline of the present work

The rest of this dissertation is organized as follows.

Here, we utilize the state-of-art, first-principles density functional theory calculations to predict various properties of multiferroics and ferrimagnets, such as the total energy, polarization, and magnetization. In Chapter 2, we give a brief introductions to the computational methods that are used in this dissertation. The Chapter 2 covers (i) the basic ideas of the density functional theory; (ii) the magnetic effective Hamiltonian used in the Monte Carlo simulations ; and (iii) brief explanations on the method of extracting the magnetic exchange coupling parameters, polarization and implementation of the external magnetic field in the density functional theory calculations.

In Chapter 3, we study the epitaxial strain effect on the linear magnetoelectric coupling coefficient in $Sr_{0.5}Ba_{0.5}MnO_3$ compound. Using density functional theory calculations, we find a huge enhancement in the linear magnetoelectric coefficient at the phase transition points from high-symmetry phase to low-symmetry phase. Such enhancement was found to be directly correlated with the sudden increase in the dielectric susceptibility at the phase transition points.

In Chapter 4, we focus on a magnetoelectric coupling at the magnetic domain wall in rare-earth iron garnets. Rare-earth iron garnets were found to have electric polarization when a magnetic domain wall was introduced in the system. Such magnetoelectric coupling was found to be not spin-orbit coupling driven and not related to the rare-earth elements but rather it was found to be driven by ferromagnetic interactions between octahedral and tetrahedral Fe ions at the domain walls, and the mechanism behind is found to be a symmetric exchange-striction mechanism.

In Chapter 5, we look at how epitaxial strain affects the magnetic properties of Gadolinium Iron Garnet, such as magnetization compensation temperature and Curie temperature. Furthermore, we study how different growth directions (along pseudo-cubic [001] or [111]) or epitaxial strain affect the magnetic properties of Rare-earth Iron Garnet films such as perpendicular magnetic anisotropy.

In Chapter 6, we study the properties of metallic ferrimagnet Mn_4N. Note tat Mn_4N is found to have anti-perovskite structure with three different Mn atoms in its unit cell. Magnetic interactions between its three different Mn atoms lead to an interesting funding such as (i) a sizable magnetization compensation temperature; and (ii) nano-metric sized topological phase - Hedgehog-Anti-Hedgehog Pair. Such topological phase was found to be stabilized by the fourth nearest-neighbor interaction between Mn atoms.

In Chapter 7, we summarize our works from Chapters 3 to 6, and point out several promising research directions for future investigation in the field of magnetoelectricity and ferrimagnetism.

The contents of Chapters 3 to 6 are mainly based on the following papers:

- Bayaraa, T., Yang, Y., Ye, M., and Bellaiche, L. (2021). Giant linear magnetoelectric effect at the morphotropic phase boundary of epitaxial $Sr_{0.5}Ba_{0.5}MnO_3$ films. Physical Review B, 103(6), L060103.

- Bayaraa, T., Xu, C., Yang, Y., Xiang, H., and Bellaiche, L. (2020). Magnetic-Domain-Wall-Induced Electrical Polarization in Rare-Earth Iron Garnet Systems: A First-Principles Study. Physical Review Letters, 125(6), 067602.

- Bayaraa, T., Xu, C., Campbell, D., and Bellaiche, L. (2019). Tuning magnetization compensation and Curie temperatures in epitaxial rare earth iron garnet films. Physical Review B, 100(21), 214412.

- Bayaraa, T., Xu, C., and Bellaiche, L. (2021). Magnetization compensation temperature and frustration-induced topological defects in ferrimagnetic anti-perovskite

Mn_4N. Physical Review Letters, 127(21), 217204.

2 Computational Methods

2.1 Introduction

Material science is currently one of the most popular fields of research due to its huge demand for invention and development of more structural and functional materials that are faster, stronger, lighter, and cheaper. For a particular application of a material we need to predict the crystallographic structure and its various properties under different conditions.
In this chapter we explain the theory of electrons in solids and the computational methods that were used in this dissertation. Everything around us, atoms, molecules, clusters or solids are systems composed of mutually interacting electrons and nuclei. The non-relativistic time-dependent Hamiltonian of a system with mutual interaction through Coulomb forces, can be defined via the Schrödinger equation as [45]

$$H_{tot} = \sum_i \frac{\mathbf{p}_i^2}{2m_e} + \sum_I \frac{\mathbf{p}_I^2}{2M_I} + \sum_{Ii} \frac{z_I e^2}{|\mathbf{R}_I - \mathbf{r}_i|} + \frac{1}{2}\sum_{i\#j} \frac{e^2}{|\mathbf{r}_i - \mathbf{r}_j|} + \frac{1}{2}\sum_{I\#J} \frac{z_I z_J e^2}{|\mathbf{R}_I - \mathbf{R}_J|} \qquad (2.1)$$

where $\mathbf{P}_I$ and $\mathbf{p}_i$ are the momenta of nuclei and electrons; $\mathbf{r}_i$ and $\mathbf{R}_I$ coordinates of the electrons and nuclei; m_e, M, and z_I are the mass of the electrons, the mass of the nuclei and the charge of the nuclei, respectively.

However, utilizing this powerful equation in many-body system is an almost impossible task. For solids (that consists of ions and electrons), solving the exact Hamiltonian would require us to treat ions and electrons of the order of, at least, $\sim 10^{23}$ and the Coulomb interaction between electrons in the system. Thus, throughout history, approximations have been used to overcome the hurdle of many-body interactions. The first and most well-known approximation is the Born-Oppenheimer approximation which suggests to neglect the kinetic energy term of the nuclei in Eq. (2.1) which implies that nuclear and electronics degrees of freedom can be taken as separate when the electronic mass is much smaller than that of the

nuclei. Thus, nuclear positions become classical variables and the nuclei can be considered as fixed when considering electronic degrees of freedom. Furthermore, this approximation also considers the nuclear repulsion as a constant for any fixed configuration.

2.2 Density Function Theory

A full quantum mechanical treatment is necessary in order to know the electronic and structural properties of a material. In quantum mechanics, all the information regarding the properties of the system is contained in its wavefunction which requires us to solve the Schrödinger equation for that system. However, for a many-body system consisting of N particles, the total wavefunction is a function of all the spatial degrees of freedom of the particles (3N) times the spin degrees of freedoms. Such task is unfeasible and impossible with current technology and computational power. Here, density functional theory (DFT) becomes handy and provides a favorable way to approach this computational problem. The basic idea behind DFT, is to consider much more convenient factor, the ground state one-body electron density, instead of the ground state many-body wavefunction. In doing so, the function to be considered becomes of only 3 variables plus spin-degree of freedom. Such idea began with Hohenberg-Kohn theorem [46] and the Kohn-Sham [47] approach and they form the basis of DFT.

2.2.1 Hohenberg-Kohn Theorems

According to Quantum Mechanics, one can determine all properties of an interacting system, including density, if external potential (V_{ext}) is known. However, it was not clear whether knowing the density is sufficient to obtain the external potential until the Hohenberg-Kohn theorems. These theorems are as follows [46]

Theorem I. (Uniqueness) *Total ground state energy of a quantum mechanical system is a unique functional of the electron density:* $E = E[n(\boldsymbol{r})]$*, where* $n(\boldsymbol{r})$ *is the electron den-*

sity [46]

Thus one can uniquely determine the ground state observables without finding the many-body wavefunctions, by knowing the density. According to this, the ground state energy of a system can be expressed as a functional, and it is as follows

$$E[n] =< \Psi[n]|T + V_{ee}|\Psi[n] > \tag{2.2}$$

where T is the kinetic energy of electrons, V_{ee} is the electron-electron interaction and V_{ext} is the external potential experienced by the electrons from nuclei. According to Eq. (2.2), the external potential uniquely determines the Hamiltonian which implies that there is a one-to-one correspondence between the external potential and the density (i.e., no two external potentials can lead to the same ground state density).

Theorem II. (Variational Principle and Universality) *The electron density that minimizes the overall functional is the true ground state electron density:* $E[n(\boldsymbol{r})] > E_0[n_0(\boldsymbol{r})]$, *where* $n_0(\boldsymbol{r})$ *is the ground state density.* [46]

Thus the exact $n_0(\mathbf{r})$ minimizes the total energy functional in Eq. (2.2).

Furthermore, for a given potential v_{ext} the total energy as a unique functional of $n_{\mathbf{r}}$ is

$$E[n] = F[n] + \int d\mathbf{r} v_{ext}(\mathbf{r}) n(\mathbf{r}) \tag{2.3}$$

where $F[n]$ is a new functional containing the kinetic energy and the electron-electron interaction energy and $V_{ext} = \sum_i v_{ext}$.

$F[n]$ is *universal* functional that does not depend on V_{ext} and can be expressed as

$$F[n] = T_s[n] + \frac{1}{2} \int d\mathbf{r} d\mathbf{r'} \frac{n(\mathbf{r} n(\mathbf{r'}))}{|\mathbf{r} - \mathbf{r'}|} + E_{xc}[n] \tag{2.4}$$

where $T_s[n]$ is the kinetic energy of a system of non-interacting electrons. The second term represents the Coulomb interaction energy and the functional $E_{xc}[n]$ is called the exchange-

correlation energy.

The exact expression of $E_{xc}[n]$ is not known (approximations are needed) and all the many-particle effects are contained in it.

2.2.2 Kohn-Sham Approach

Although Hohenberg-Kohn theorems makes many-body problem more approachable, it does not give an explicit way to find the ground state density. Later on, Kohn and Sham (KS) came up with their approach to address this issue [47]. Main idea behind the approach is to find an auxiliary non-interacting system exposed to an effective potential V_{eff}, such that this system gives the same density as for the interacting system with the external potential V_{ext}.

Thus, the new Hamiltonian of the non-interacting system is

$$H_{eff} = T_s + V_{eff} \tag{2.5}$$

with an energy functional of

$$E_{eff}[n] = T_s[n] + \int d\mathbf{r} v_{eff}(\mathbf{r}) n(\mathbf{r}) \tag{2.6}$$

where the effective KS potential is

$$v_{eff}(\mathbf{r}) = v_{ext}(\mathbf{r}) + \int d^3r' \frac{n(\mathbf{r'})}{|\mathbf{r} - \mathbf{r'}|} + \frac{\delta E_{xc}[n]}{\delta n(\mathbf{r})} \tag{2.7}$$

The last term in Eq. (2.7) is called the exchange-correlation potential

$$v_{xc}(\mathbf{r}) \equiv \frac{\delta E_{xc}[n]}{\delta n(\mathbf{r})} \tag{2.8}$$

Equations (2.6) and (2.7) are called Kohn-Sham equations and they can be solved in a

self-consistent manner. Generally, in DFT, Kohn-Sham equations are run in self-consistent cycle until certain threshold and the final density is the correct ground state density of the non-interacting system but also for the interacting system by construction. However, no definitive form for the exchange-correlation potential is known yet, thus one has to obtain it approximately.

2.2.3 Local density and general gradient approximations

One of the most common and the simplest approximation is the local density approximation (LDA). In this approximation, the exchange-correlation functional E_{xc} is assumed to be local and the exchange-correlation energy per electron corresponds to a homogeneous/uniform electron gas [48].

In LDA,

$$E_{xc}[n(\mathbf{r})] = \int \epsilon_{xc}[n(\mathbf{r})]n(\mathbf{r})dr \tag{2.9}$$

where $\epsilon_{xc}[n(\mathbf{r})]$ is exchange-correlation energy per electron in a homogeneous electron gas of density $n(\mathbf{r})$. For systems where the density varies slowly, the LDA tends to perform well but the accuracy breaks down when the system becomes strongly correlated.

The more accurate type of approximations is called Generalized Gradient Approximation (GGA) where it considers the gradient of the electron density in addition to the local density [49].

In GGA,

$$E_{xc}[n(\mathbf{r})] = \int f(n(\mathbf{r}), \bigtriangledown n(\mathbf{r}))dr \tag{2.10}$$

where $f(n(\mathbf{r}), \bigtriangledown n(\mathbf{r}))$ is a function of the density $n(\mathbf{r})$ and its gradient $\bigtriangledown n(\mathbf{r})$.

There are some other approximation that go beyond GGA and they are called meta-GGA and hybrid functionals. Meta-GGA is an approximation which takes into consideration the Kohn-Sham kinetic energy density in addition to the density and its derivatives in the right side of the Eq. (2.10). Hybrid functionals are different combinations of different exchange-

correlation functionals.

2.2.4 The Relativistic Effect - Spin-Orbit Coupling

For electronic structure calculations, the starting point is the Schrödinger equation which is a non-relativistic equation. However, depending on the system, the relativistic effects can become very important and they need to be taken into account in order to have a reasonable description of the system. The well-known and most significant correction due to the relativistic effect is the spin-orbit coupling (SOC). In solids, SOC derives the spin-splitting for electrons and if the symmetry permits, it leads to the coupling between the orientation of the electron spin and its crystal momentum. This symmetry-permitted coupling can give rise to spin-dependent band structures and well-known examples are the Dresselhaus [50] and Rashba [51] effects.

$$H_{SOC} = -\frac{e}{2c^2 m_e^2 r}\frac{dV_{eff}(\mathbf{r})}{dr}\mathbf{S}\cdot\mathbf{L} = \alpha\mathbf{S}\cdot\mathbf{L} \tag{2.11}$$

where $S = \sigma/2$ is the spin of the electron, $\mathbf{L} = \mathbf{r}\times\mathbf{p}$ is is the orbital angular momentum operator, and α is the SOC constant.

2.2.5 On-Site Coulomb correction (Hubbard U and Hund J)

Despite its huge success, DFT fails when one considers a class of material containing not fully occupied or unoccupied shells of localized electrons such as d and f orbitals [52–55]. In these orbitals, the motion of electrons is strongly entangled to each other which makes DFT not able to express well enough their kinetic and the Coulomb energies due to the fact that a DFT exchange-correlation functional is based on a homogeneous electron gas. Thus, one needs to find a way to treat these electrons in a correct manner and one such way is done with the Hubbard Model [56] . Hubbard model is one of the famous models used nowadays

and it assumes the interaction between electrons to be purely local as

$$\hat{H}_{Hub} = -\sum_{\mathbf{r},\mathbf{r'},\sigma} (t_{\mathbf{r},\mathbf{r'}} \hat{c}^{\dagger}_{\mathbf{r},\sigma} \hat{c}_{\mathbf{r'},\sigma} + h.c.) + U \sum_{\mathbf{r}} \hat{n}_{\mathbf{r},\uparrow} \hat{n}_{\mathbf{r},\downarrow} \tag{2.12}$$

where $t_{\mathbf{r},\mathbf{r'}}$ is the energy that electrons gains when jumping from site $\mathbf{r}$ to $\mathbf{r'}$, $\hat{c}\dagger$ and $\hat{c}$ are the creation and annihilation operators, respectively, and $\hat{n}_{\mathbf{r},\uparrow}$ and $\hat{n}_{\mathbf{r},\downarrow}$ are the number operators for spin up and down at site $\mathbf{r}$, respectively. The amplitude of t directly corresponds to the bandwidth of the valence electrons states and this term relates to the single-particle term of the total energy. In the strongly correlated systems, the partially screened Coulomb repulsion affects mainly the electrons on the same atom through a term that is called the "Hubbard U". Particularly, this U parameter expresses the penalty you pay for having two electrons with opposite spins on the same site. For metallic systems, $t >> U$ (for which DFT can describe well the system) but for systems with dominating short-range Coulomb interactions, $t << U$, thus, pure DFT method is not a wise choice to treat the system.

Main features of Hubbard model can be included into DFT functional as a correction and this approach is called DFT+U approach [52, 53]. With this approach, more accurate description of the ground state of correlated systems becomes possible. The correction is considered when describing strongly-correlated electronic states such as localized d and f orbitals but treats the other valence electrons with the standard DFT functional. In general, the energy term in DFT+U approach can be described as $E_{DFT+U} = E_{DFT} + E_{Hub}[n] + E_{dc}[n]$ where E_{Hub} contains the electron-electron interactions described by the Hubbard Hamiltonian for localized electrons, and E_{dc} is the double counting term.

The Hubbard U corrections can be introduced into DFT in different ways. The two main branches are the one introduced by Liechtenstein et al. [57], where U and J take as independent corrections in the calculations, and the one suggested by Dudarev et al. [58], where only a single effective parameter, $U_{eff} = U - J$, is considered for the Coulomb interaction. The main difference between these two approach is that the extra correlations in the Du-

darev approach depends only on U_{eff} in isotropic screened on-site Coulomb interaction and is equivalent to the Liechtenstein approach with J = 0. In practice, the U and J parameters are often chosen to fit one experimental quantity (i.e. the band gap or the magnetic moment) of the studied system. However there is no guaranteed way to obtain these parameters yet.

2.3 Magnetic Effective Hamiltonian

Transition metals and rare-earth systems have a dual nature thanks to their d and f orbital electrons. These electrons have both itinerant nature that defines their charge conductivity and localized character that triggers the local magnetic moments in them. The magnetic properties of a system can be described by using a spin Hamiltonian defined in terms of a few spin exchange parameters. Such a spin Hamiltonian is used to describe the essence of the underlying physics and chemistry behind the magnetic interactions in the system, while utilizing a minimal set of magnetic bonds. A general spin Hamiltonian can be expressed as

$$\hat{H}_{spin} = \sum_{i<j} J_{ij}\hat{S}_i \cdot \hat{S}_j + \sum_{i<j} \overrightarrow{D}_{ij} \cdot (\hat{S}_i \times \hat{S}_j) + \sum_i A_i S_{iz}^2 + \sum_{i<j} K_{ij}(\hat{S}_i \cdot \hat{S}_j)^2 \tag{2.13}$$

where the first term represents the symmetric exchange interaction which is usually known as the Heisenberg exchange interaction, the second term represents the antisymmetric exchange interaction describing the Dzyaloshinskii–Moriya (DM) spin exchange term, the third term represents the single-ion anisotropy (SIA), and the last term represents the biquadratic interaction. Both the DM interaction (DMI) [59] and SIA are a consequence of spin–orbit coupling. The biquadratic interaction (the last term) can be derived by applying the fourth-order perturbation to the Hubbard model. Note that a spin Hamiltonian of a system does not need to have all four terms to describe its magnetic properties because some terms may not be allowed by symmetry or can be negligibly small.

The following spin Hamiltonian is adopted in the studies of this dissertation:

$$H_{spin} = H^{DEC} + H^{DMI} + H^{SIA}, \tag{2.14}$$

with

$$H^{DEC} = \sum_{<i,j>} J_{ij}\mathbf{S}_i \cdot \mathbf{S}_j$$

$$H^{DMI} = \sum_{<i,j>} \mathbf{D} \cdot (\mathbf{S}_i \times \mathbf{S}_j)$$

$$H^{SIA} = \sum_{i} A_i\mathbf{S}_i \cdot \mathbf{S}_i$$

where H^{DEC}, H^{DMI}, H^{SIA} represent energies from the diagonal exchange coupling, Dzyaloshinskii-Moriya interaction (DMI), and single ion anisotropy (SIA), respectively. The sum over $< i, j >$ denotes the different magnetic pairs considered in the studies. The sum over i runs through all magnetic sites.

H^{DEC} describes the energy of an isotropic magnetic system because it has only three Cartesian components that are non-zero due to $\mathbf{S}_1 \cdot \mathbf{S}_2 = S_{1x}S_{2x} + S_{1y}S_{2y} + S_{1z}S_{2z}$. Thus, the lowest energy occurs when $J > 0$ and angle θ between the two spins is 180° (i.e. AFM spin arrangement), and when $J < 0$ and $\theta = 0°$ (i.e. FM spin arrangement). In both case, such spin Hamiltonian leads to a collinear spin arrangement. J is the magnetic exchange coupling parameter.

H^{DMI} allows one to include canting of the spins from their collinear arrangement in the total Hamiltonian by incorporating DMI. The term $\mathbf{S}_i \times \mathbf{S}_j$ is proportional to sinθ where θ is the angle between two spin vectors and it is non-zero only if spins are not aligned collinearly. Thus, H^{DMI} introduces spin canting in the total Hamiltonian. Here, $\mathbf{D}$ is the Dzyaloshinskii–Moriya vector.

H^{SIA} represents the magnetocrystalline anisotropy energy rising from the preferred spin orientation of the magnetic ions. This magnetic anisotropy can be introduced to the spin Hamiltonian by utilizing the constant A_i which is related to the energy difference between two perpendicular spin orientations (i.e. $E_i(\| z)$ and $E_i(\perp z)$).

The values of J_{ij}, $\mathbf{D}$ and A_i can be extracted from first principles calculations. Then, the

spin Hamiltonian of Eq. (2.14) can be utilized to study the thermodynamic properties as well as the spin dynamics of the system. In theoretical studies, they can be extracted from electronic structure calculations by different methods that have their own advantages and disadvantages. Here, 4-state energy mapping method is utilized to extract J_{ij}, $\mathbf{D}$ and A_i parameters from DFT calculations [60].

2.4 The calculation of the magnetic parameters and beyond

2.4.1 Four-state Energy Mapping Method

This method helps one to make energy-mapping analysis based on a four different ordered spin states. The total-energy differences are used to calculate the different magnetic parameters. Advantages of this method are that no knowledge of the underlying exchange mechanism is necessary and the accuracy is only dependent on the quality of the exchange-correlation functional used in the study (i.e., how well the exchange-correlation functional can describe the system). On the other hand, the method requires one to use quite a large number of spin configurations, large supercell, and the result is just a number, which is hard to analyze if one wants to know the specific orbital contributions to the magnetic parameters. In general, if we restrict ourselves to a single type of magnetic atom and its nearest neighbor interactions only, J_{ij}, $\mathbf{D}$ and A_i parameters can be express as

$$J = \frac{(E_{\uparrow\uparrow} + E_{\downarrow\downarrow}) - (E_{\uparrow\downarrow} + E_{\downarrow\uparrow})}{NS^2}$$

$$\pm D = \pm\frac{(E_{\uparrow\uparrow} + E_{\downarrow\downarrow}) \mp (E_{\uparrow\downarrow} + E_{\downarrow\uparrow})}{NS^2}$$

$$A = \frac{(E_{\uparrow\uparrow} + E_{\downarrow\downarrow}) - (E_{\uparrow\downarrow} + E_{\downarrow\uparrow})}{NS^2}$$

where $E_{\uparrow\uparrow}(E_{\downarrow\downarrow})$ and $E_{\uparrow\downarrow}(E_{\downarrow\uparrow})$ are the energies of the ferromagnetic and antiferromagnetic configuration between the studied magnetic ions. Note that all the other magnetic ions in the supercell should be aligned perpendicular to the spin alignment of the studied magnetic ions. N is the total number of the magnetic configurations used and S is the spin number. Here, in the studies presented, spins (S) are set to be 1 and their values are absorbed by the magnetic exchange coupling (J) parameters. For further information about the method, we refer to the original review article [60].

2.4.2 Monte Carlo Simulations

Once, all the magnetic parameters are calculated, one can utilize Eq. (2.14) and Monte Carlo (MC) simulations to study thermodynamic properties of systems such as ordering temperature, evolution of magnetic moment with respect to temperature, finding of metastable phases, etc.. MC simulation method is one of the most powerful and widely used method in condensed matter physics, science and engineering sectors. Generally, MC method is utilized to calculate high-dimensional integrals and handles systems with several degrees of freedom. MC is based on an evolutionary search of the equilibrium ground state and the core idea behind the search is to estimate the integral of a quantity based on a random sampling of the integration volume at the cost of a statistical error. Thus, in every MC step, if the randomly selected step lowers the energy of the system, then this step is accepted and if not, it is rejected (note that it can be different depending on the temperature). In this way, the system can be brought into thermal equilibrium for any given temperature.

2.4.3 Polarization

Throughout this dissertation and in all of its studies, the electric polarization has been calculated using the "Berry Phase Method" of the modern theory of polarization [61–63].
Until the development of modern theory of polarization [61–63], calculation of the electric polarization from first-principles perspective was problematic. In general, electric polariza-

tion is defined as the total dipole moment per unit volume but this definition is not applicable if one is considering a quantum mechanical system of periodic solids. For example,

$$P_{dipole} = \frac{1}{V_{cell}} \int_{cell} \overrightarrow{r} \rho(\overrightarrow{r}) d^3 r \tag{2.15}$$

represents the dipole moment of the charge distribution inside one unit cell. However, this formula of polarization is heavily dependent on the choice and the size of the unit cell, thus it is a poor choice for infinite systems.

In experiment, during the polarization switching, the current flow $\mathbf{j}$ is measured and the accumulated current flow is used to define the change in polarization $\Delta\mathbf{P}$ as

$$\Delta\mathbf{P} = \mathbf{P}(\Delta t) - \mathbf{P}(0) = \int_0^{\Delta t} \mathbf{j}(t) \tag{2.16}$$

The spontaneous polarization is determined as $\mathbf{P}_s = \Delta\mathbf{P}/2$. Thus, in experiment, the spontaneous polarization itself is not measured but the change in polarization is measured in order to obtain the spontaneous polarization. Hence, it is more meaningful to study the change in polarization during an adiabatic evolution and it is the important conceptual foundation of the modern theory of polarization:

$$\Delta\mathbf{P}_{i\to f} = \int_i^f \partial_\lambda \mathbf{P} d\lambda \tag{2.17}$$

where λ is the parameter that changes slowly in time and, for ferroelectrics, λ can represent the sublattice displacement which drives the system from a centrosymmetric state to the ferroelectric state. However, this Eq. (2.17) does not give the same answer when two different paths are chosen when going from $i \to f$. In order to avoid this issue, the modern theory of polarization formulated the change in polarization contributed by electrons as an integrated current across the Brillouin zone in the form of a Berry phase (Berry phase is a phase angle (0-2π) that describes the global phase evolution of a complex vector as it is

carried around a path in its vector space) as

$$\partial_\lambda P_n = \frac{-e}{2\pi}\int_0^{2\pi a} \Omega_n^{\lambda k} dk \tag{2.18}$$

Thus, the first-order change in polarization is proportional to the Brillouin zone integral of the Berry curvature, $\Omega_n^{\lambda k}$, in (λ, k) space. Now, if we plug this expression into the Eq. (2.17):

$$\Delta P_{n,i\to f} = \frac{-e}{2\pi}\int\int_s \Omega_n^{\lambda k} d\lambda dk = \frac{-e}{2\pi}\Phi_{s,n}^{(\lambda k)} \tag{2.19}$$

So, ΔP_n is just a Berry flux of band n passing through the (λ, k) space. Thus,

$$\Delta P_{n,i\to f} = \frac{-e}{2\pi}\sum_n^{occ}(\Phi_n(\lambda_t) - \Phi_n(\lambda_i)) \tag{2.20}$$

This equation does not contain unoccupied states and is gauge invariant. Plus, no detailed knowledge of the path is necessary.

In fact,

$$\Delta P_{i\to f} = P(\lambda_f) - P(\lambda_i) \tag{2.21}$$

$$P = \frac{-e}{2\pi}\sum_n^{occ}\Phi_n \tag{2.22}$$

Above equations are the central results of the modern theory of polarization. Now, if we include the ionic part of the polarization and generalize it to three dimensions

$$\Delta \mathbf{P}_{i\to f} = \Delta \mathbf{P}_{ionic} + \mathbf{P}(\lambda_f) - \mathbf{P}(\lambda_i) \tag{2.23}$$

and

$$\Delta \mathbf{P}_{ionic} = \frac{e}{\Omega}\sum_s Z_s^{ion}\mathbf{r}_s \tag{2.24}$$

where eZ_s^{ion} is the nominal charge of the ion located at $\mathbf{r}_s$ and Ω is the volume of the unit cell.

2.4.4 Implementation of external magnetic field in DFT calculations

Here, the linear magnetoelectric coupling coefficients α_{ij} are extracted from the DFT calculation results by applying an uniform Zeeman magnetic field in the crystal. In other words, α_{ij} coefficients are extracted from the change in the macroscopic polarization in a finite magnetic field, which is included by adding a Zeeman potential term ΔV_{Zeeman} (only applied to the spins) to the external potential V_{ext}:

$$V_{Zeeman} = \frac{-g}{2}\mu_B\mu_0 \begin{pmatrix} H_z & H_x + iH_y \\ H_x - iH_y & -H_z \end{pmatrix} \tag{2.25}$$

where H is the applied magnetic field. Once Eq. (2.25) is implemented in DFT, α_{ij} coefficients can be found using the following equation:

$$\alpha_{ij,S} = \frac{\Delta P_i}{\Delta H_j} \tag{2.26}$$

For further information, we refer to the original article [16].

3 Giant enhancement of magnetoelectric coupling at the morphotrophic phase boundary of SBMO films

3.1 Introduction

As introduced in Chapter 1.2, the search for materials having a strong magnetoelectric (ME) coupling has attracted great interest in last two decades [2, 64], for technological and fundamental purposes. In addition, the understanding of the underlying mechanism behind ME coupling is a crucial line of research.

However, a single-phase multiferroics usually has a weak ME coupling or it is only significant at very low temperatures [65] and such obstacle is one of the biggest hurdles for technological applications. Thus, the research on novel multiferroic systems and methods to enhance ME coupling is receiving considerable attention [66–71]. Among the various families of multiferroics, perovskite oxides with chemical formula of ABO_3 are under extensive research and a strong ME response has been predicted in the $BiFeO_3 - BiCoO_3$ solid compound from a first-principles study [72]. Such study revealed that the transition between two structural polymorphs of rhombohedral $R3c$ and tetragonal $P4mm$ symmetries is related to the strong ME coupling. Electric-field driven transition between these two structural polymorphs leads to the rotation of the easy magnetic axis with a change in direction and magnitude of spontaneous polarization. Afterwards, the experimental verification of such polarization rotations with composition and temperature was realized in the $BiCo_{1-x}Fe_xO_3$ system adopting the monoclinic Cm symmetry [73]. Furthermore, a region so-called morphotropic phase boundary (MPB), for which the systems exhibit several different phases, was found experimentally to be magnetoelectric in the chemically designed $BiFeO_3 - BiMnO_3 - PbTiO_3$ ternary system [74, 75] and $(1-x)BiTi_{(1-y)/2}Fe_yMg_{(1-y)/2}O_3 - xCaTiO_3$ compound [76]. Such results suggest that MPB is a promising approach to achieve a large magnetoelectric coupling in multiferroics. Moreover, as mentioned in Chapter 1.2, an enhancement of magnetoelectric response was predicted to be correlated with the softening of the lattice by Wojdel et al.

[25]. Thus, a question arises on whether it is possible to induce large magnetoelectricity in simpler materials and in a simpler way (i.e., that does not involve the mixing between three or more systems, and does not require to apply electric fields, or change composition, to break the symmetry of the system towards lower-in-symmetry phases), using the concept of MPB – that is known to make the lattice softer or lowering of the symmetry. Then, such a hypothetical possibility would make applications more feasible. Plus, revealing the precise microscopic physical quantity responsible for a large enhancement of magnetoelectricity is also of fundamental interest.

Our previous first-principles calculation results [5] on $Sr_{0.5}Ba_{0.5}MnO_3$ (SBMO) films under different epitaxial strain (compressive and tensile) showed that SBMO films go through different structural and magnetic phase transitions under epitaxial strain and it is accompanied by a large jump in polarization and c/a value (see Fig. 3.1). This large polarization enhancement occurs when there is a change in magnetic state (spin configuration) which originates from a strong coupling between electric and magnetic properties in this system. Also, we have found that there is a strain-induced morphotropic phase boundary (MPB) that is bridging the known high-symmetry tetragonal and orthorhombic states with a low-symmetry monoclinic phase having, e.g., a large piezoelectric response. Therefore, this monoclinic phase shows signs of structural softness and having a large piezoelectric response which could lead to a large response in the third term in Eq. (1.4).

In this work, we will employ a first-principles methods discussed in Chapter 2 to study spin originated ME coefficients in SBMO films under different strains (orbital magnetism is neglected here because it typically yields much smaller response than the one associated with spins). Our motivations are (i) study and understand the linear ME coupling in SBMO films; (ii) test the general strategy of employing strain-engineering to induce a large enhancement in ME coupling in the MPB region; and (iii) reveal the microscopic physical quantity behind the enhancement of ME coupling, if any.

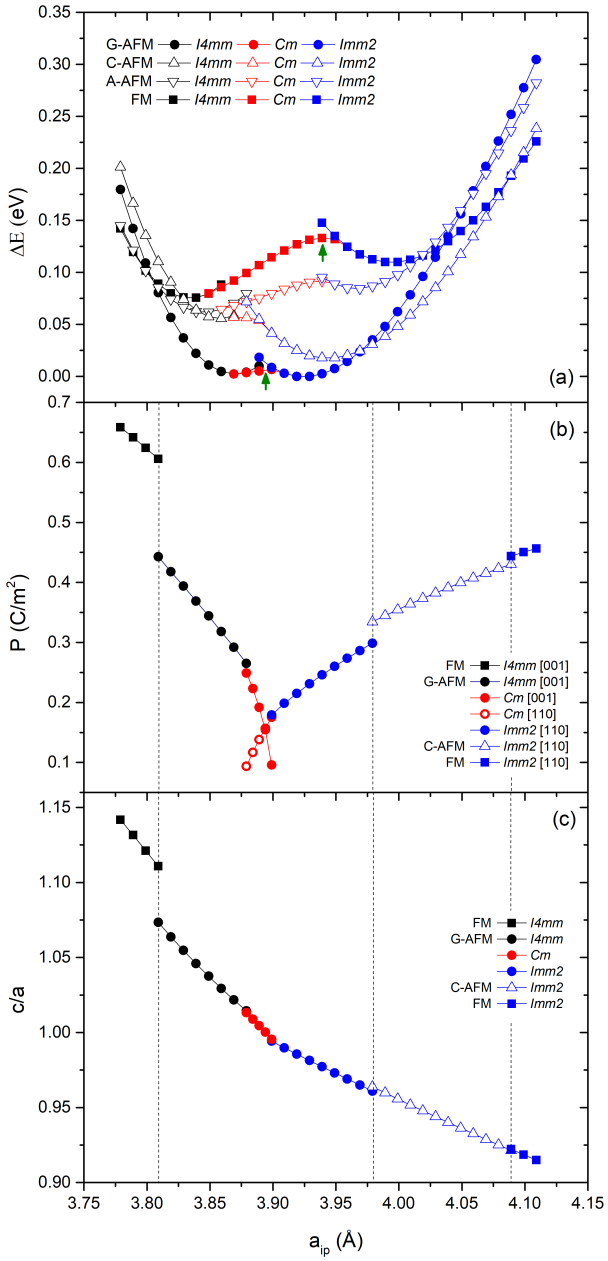

Figure 3.1: Properties of the SBMO films. Panel (a) shows the total energy of the $I4mm$, Cm and $Imm2$ states, for the four AFM magnetic arrangements. The arrows show the local maxima of the monoclinic structure for the G-AFM and FM orderings. Panel (b) displays the out-of-plane and in-plane components of the polarization in the different ground states, while Panel (c) reports the associated evolution of the axial ratio. The vertical dashed lines denote the magnetic transitions in Panels (b) and (c). The figure is taken from [5].

3.2 Methods

All first-principles DFT calculations are carried out by the Vienna ab initio simulation package (VASP) [77] and simulated by the projector augmented-wave potentials [78]. The exchange-correlation functional PBE+U+J functional is used [49, 57] and the Hubbard U and Hund J values on Mn atoms are chosen to be 3.0 eV and 1.0 eV, respectively. We use a $\sqrt{2} \times \sqrt{2} \times 2$ simulation cell that has 20 atoms to adapt G-type AFM magnetic orderings and an energy cutoff of 550eV is used along with a 6x6x4 Monkhorst-Pack k-point mesh. Berry phase method [63] is used to calculate the polarization and space groups are identified using the Isotropy software [79]. The structures are relaxed imposing frozen in-plane lattice parameter a_{ip} and in-plane lattice vectors, with noncollinear spin arrangements and spin-orbit coupling (SOC). In our calculations, we carefully converge magnetic properties with a small tolerance factor ($< 2\mu eV/\mathring{A}$) and a small energy error threshold of 10^{-9} eV. The linear magnetoelectric coupling coefficients are computed by applying an external magnetic field as described in Chapter 2.4.4. This method was found to be valid and accurate in various systems [16, 80–82]. For example, for Cr_2O_3 – the typical prototype of magnetoelectric, the linear magnetoelectric coupling coefficient was found to be 1.45ps/m [16] which is in good agreement with experimental result of 1.58ps/m [83]. Note that the computed linear ME coupling in our study includes both ionic and electronic contributions. All first-principles calculations are performed under external magnetic fields ranging from 0T to 30T, including spin-orbit coupling. Furthermore, we also calculated vibrational properties by the linear response method as implemented in the Phonopy code [84], the dielectric susceptibility is calculated by density functional perturbation theory implemented in VASP, and the magnetic susceptibility is determined by analyzing the slope of change in the total magnetic moment when an external magnetic field is applied.

3.3 Structure and Magnetic Symmetry

Bulk SBMO structure is tetragonal with ferroelectric distortion and an elongation of the c-axis with $T_C \approx 400K$ [85]. This elongation allows magnetic Mn^{4+} (S=3/2) ions to displace from the center of the surrounding oxygen octahedron, leading to a ferroelectric phase. The experimentally determined space group is $P4mm$, in-plane lattice constant $a_{ip} = 3.85\mathring{A}$ with a c/a value of 1.0035 at low temperature. At a temperature below $T_N \approx 185K$, Mn magnetic moments order in the antiferromagnetic (AFM) structure with order parameter $G = m_1–m_2 + m_3–m_4$ where m_i is the magnetization of the ith magnetic sublattice (G-type AFM). Our previous first-principles study [5] of an epitaxial strain of SBMO showed that with tensile strain, the structure becomes orthorhombic with a space group of $Imm2$ that is bridged with its tetragonal $I4mm$ phase by a low symmetry monoclinic Cm phase (The chemical ordering of Sr and Ba atoms are taken as Rock-Salt ordering) [1]. As shown in Fig. (3.1) and (3.2(a)), SBMO films go through two structural phase transitions, via the MPB bridging two high-symmetry states. In the a_{ip}, in-plane lattice constant, regime below $3.869\mathring{A}$, SBMO films favor the tetragonal $I4mm$ state with an electric polarization lying along the pseudo-cubic [001] direction and are found to have an easy magnetic axis along the in-plane b-axis (pseudo-cubic [110] direction). On the other hand, for the a_{ip} regime above $3.9\mathring{A}$, SBMO films favor the orthorhombic $Imm2$ state with an electric polarization pointing along the b-axis and a magnetic easy-axis lying along the in-plane a-axis (pseudo-cubic [1-10] direction). Thus, both tetragonal and orthorhombic phases having a magnetic point group of $m'm2'$ (only 58 of 122 magnetic point groups allow non-zero linear ME effect [6]). Furthermore, the bridging monoclinic Cm phase has its electric polarization direction rotating from the out-of-plane pseudo-cubic [001] axis to the in-plane [110] direction as aip increases, and the easy magnetic axis of SBMO films in this region found to be rotating from the b-axis to the a-axis as a_{ip} increases, with a corresponding magnetic space group m. The inset of Fig. 3.2(a) shows the computed lowest optical frequency at the Γ-point as a function of a_{ip}. Such frequency is found to drop sharply near the phase transition points, indicating

that the high-symmetry tetragonal and orthorhombic structures are becoming dynamically unstable and thus wish to transition to the lower-symmetry associated with the monoclinic state within the MPB region.

According to this point group, $m'm2'$, the $\alpha_{ij} \in i, j = x, y, z$ tensor has only two non-zero and different α tensor components allowed by its symmetry:

$$\alpha_{ij} = \begin{bmatrix} 0 & 0 & 0 \\ 0 & 0 & \alpha_{yz} \\ 0 & \alpha_{zy} & 0 \end{bmatrix} \tag{3.1}$$

According to the equation, $P_i = \alpha_{ij} H_j$, if α_{yz} is non-zero, there should be a change in polarization along the y-axis direction when a magnetic field is applied along the z-axis direction. Similarly, if α_{zy} is not zero, there should be a change in polarization along the z-axis direction when a magnetic field is applied along the y-axis direction. Thus, in our case, α_{yz} should be determined by applying different magnitudes of a magnetic field along the c-axis and analyzing the slope of the change in the polarization results along the b-axis and a-axis in tetragonal and orthorhombic states, respectively. Similarly, α_{zy} should be determined by extracting the change in the polarization along the c-axis when applying different magnitudes of a magnetic field along the b-axis and a-axis in tetragonal and orthorhombic states, respectively. In the monoclinic state, α_{yz} and α_{zy} values are determined by the same method but with the y-axis varying from the b-axis for smaller a_{ip} to the a-axis for larger a_{ip} since the magnetic easy-axis changes around a_{ip} of 3.89 $\mathring{A}$ because the magnetic easy axis rotates within the MPB.

Figure 3.3 shows the polarization change along the y-axis (left panels) and z-axis (right panels) when a magnetic field is applied along the z-axis and y-axis, respectively, for SBMO films with the following in-plane lattice constants, a_{ip}: 3.859$\mathring{A}$ ($I4mm$), 3.869$\mathring{A}$ (Cm), 3.889$\mathring{A}$ (Cm), 3.905$\mathring{A}$ (Cm), and 3.929$\mathring{A}$ ($Imm2$). Then, α_{yz} and α_{zy} values are calculated by extracting the slope of the overall linear change in the polarization with respect to the

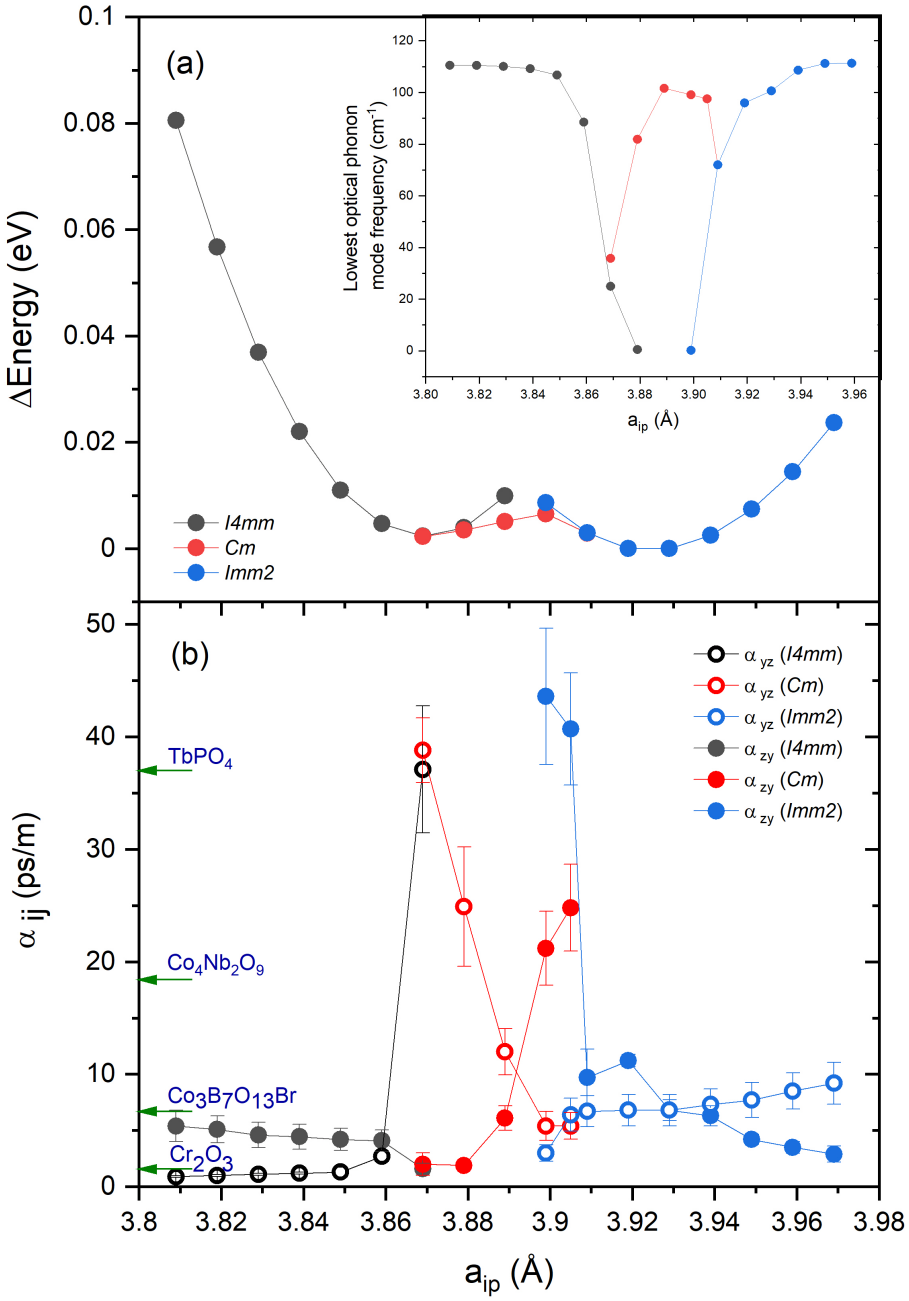

Figure 3.2: Properties of SBMO films as a function of their in-plane lattice parameter in the $I4mm$, Cm, and $Imm2$ structural states: (a) the total energy; and (b) linear magnetoelectric coupling components. The zero of energy in Panel (a) corresponds to the lowest energy structure, having $a_{ip} = 3.919\mathring{A}$. The inset in Panel (a) shows the lowest optical frequency at the Γ-point as a function of the in-plane lattice parameter. α values of four representative materials are also indicated by arrows on the vertical axis of Panel (b) [6, 7].

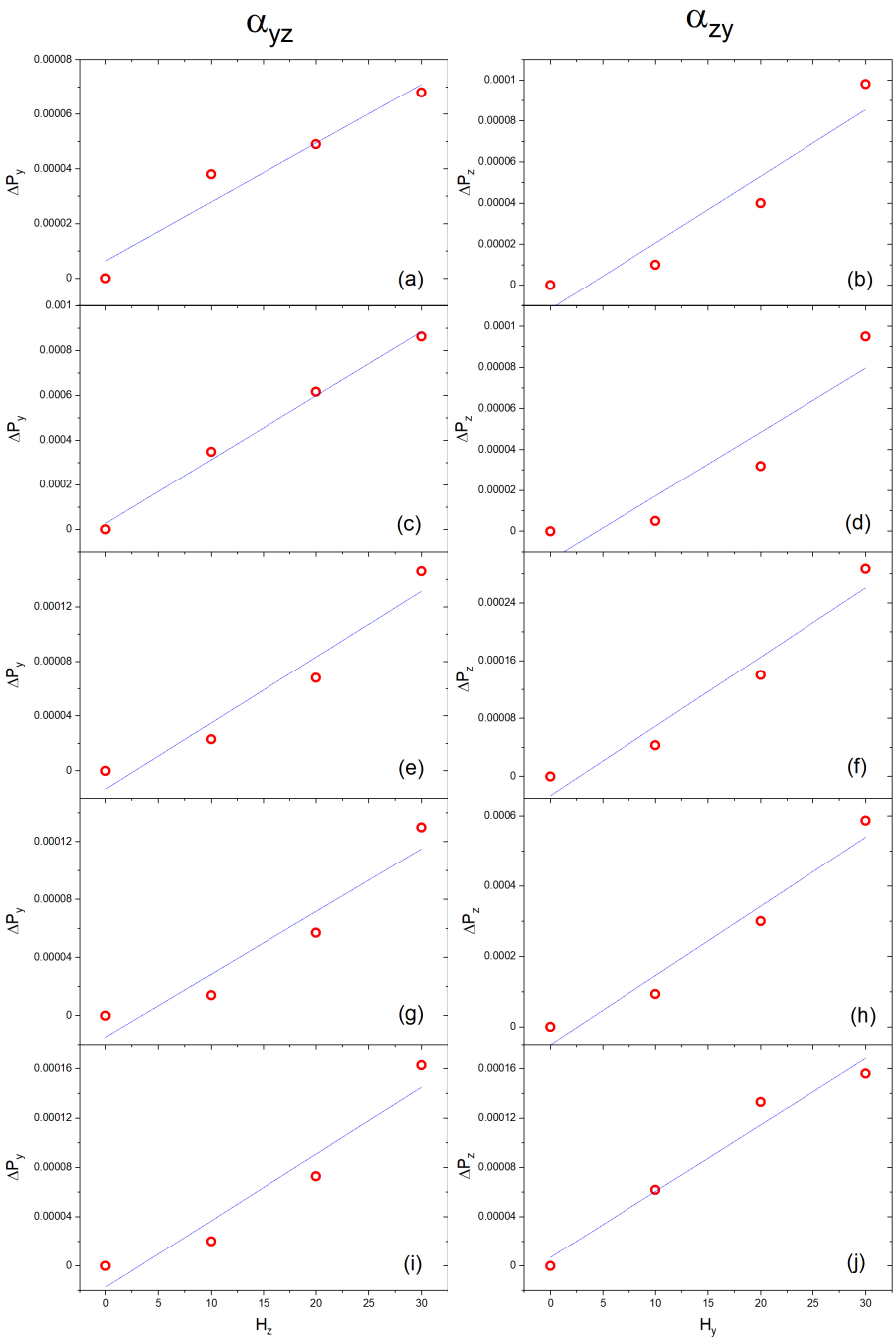

Figure 3.3: The change in polarization along the y-axis (left panels) and the z-axis (right panels) when magnetic fields are applied along the z-axis and y-axis, respectively, for SBMO films with in-plane lattice constants: (a,b) a_{ip}, of 3.859$\mathring{A}$ ($I4mm$); (c,d) 3.869$\mathring{A}$ (Cm); (e,f) 3.889$\mathring{A}$ (Cm); (g,h) 3.905$\mathring{A}$ (Cm); and (i,j) 3.929$\mathring{A}$ ($Imm2$).

applied magnetic fields at each a_{ip}. Such slopes are reported in Fig. 3.2(b) and Figure 3.4. Note that the error bars shown in Fig. 3.2(b) and Figure 3.4 are estimated errors in this slope. Note also that we have considered quite strict convergence criteria where we did structural relaxation calculations until Hellmann-Feynman forces are less than 2 $\mu eV/\mathring{A}$ on each ion, in order to make such errors minimum and thus have a polarization change as linear as possible.

3.4 Results

Fig. 3.2(b) shows that α_{zy} values in the orthorhombic state increase sharply when decreasing the a_{ip} near the structural phase transition point to the Cm phase, and then strongly decrease within this monoclinic state when further reducing a_{ip}. Similarly, α_{yz} values go through a sharp increase within Cm when decreasing the a_{ip} until approaching the transition to the tetragonal $I4mm$ phase and then is significantly gets reduced within this tetragonal state when the system is further epitaxially compressed. Thus, α_{zy} and α_{yz} cross with each other around a_{ip} of 3.895$\mathring{A}$ within the monoclinic state. Furthermore, Fig. 3.2(b) reveals a remarkable quantitative result of our simulations, namely the linear ME couplings in SBMO films can be practically enhanced to reach values as large as 40 ps/m near the phase transition points (tetragonal to monoclinic and orthorhombic to monoclinic). In order to put our results in perspective, we show several representative materials that have been previously studied and reported to have giant ME coupling and their values are indicated in Fig. 3.2(b): (i) $TbPO_4$ single crystal is the strongest known ME material with an α value of about 37 ps/m [6]; (ii) $Co_4Nb_2O_9$ with an α about 18.4 ps/m [7]; (iii) $Co_3B_7O_{13}Br$ with an α about 6.7 ps/m [6]; and (iv) the typical prototype of ME materials, Cr_2O_3, with α about 1.58 ps/m [83]. As one can clearly see, the linear ME coefficients of SBMO films within a certain range of epitaxial strains can thus be comparable to the α's the strongest known ME material (note that our computed values are at 0K while the 37 ps/m value of $TbPO_4$ has been achieved at 2K). Our computed a_{ip} of films with the highest α coefficients are 3.869$\mathring{A}$ and 3.909$\mathring{A}$

which, after rescaling by the expected overestimation of 0.34% (such value was obtained by comparing the fully relaxed a_{ip} of the bulk structure with the experimental value of Ref. [85]), become 3.856$\mathring{A}$ and 3.896$\mathring{A}$, respectively. Interestingly, these corrected lattice constants are very close to the pseudo-cubic lattice constants of $NdGaO_3$ [86] and $SrTiO_3$ [87], which are 3.86$\mathring{A}$ and 3.905$\mathring{A}$, respectively. Such a fact suggests that the growth of SBMO films on these substrates should lead to the observation of our predicted giant α values.

Now that we have shown that ME coupling coefficient can be largely enhanced in the MPB region as suggested by the general strategy of employing strain-engineering to induce softening of the lattice. Let us now try to understand the results of Fig. 3.2(b) and uncover the microscopic reason or the origin of such a large enhancement in ME coupling coefficients. In order to do that, let us take into account the analytical derivation of α coefficients from a phenomenological model which we briefly covered in Chapter 1.2.

According to Eq. (1.5), $\alpha_{ij} = \alpha_{ij}^{(1)} + \alpha_{ij}^{(2)}$ and since we numerically found a weak ferromagnetism ($M_y = 0.0001\mu_B$, $M_z = 0.002\mu_B$ and $M_z = 0.005\mu_B$ in the I4mm, Cm, and Imm2 states, respectively) along with a strong G-AFM configuration in SBMO films, we need consider both terms of Eq. (1.5) in our study. Such findings are consistent with the magnetic space groups of SBMO films, $m'm2'$ and m, which allows weak ferromagnetism [6]. Then, if we use Eqs. (1.5.1) and (1.5.2), our α_{yz} and α_{zy} are as follows:

$$\alpha_{yz} = \alpha_{yz}^{(1)} + \alpha_{yz}^{(2)} = -g_{zxy}\chi_{yy}^{P}L_x\chi_{zz}^{M} - 4\varepsilon_0\lambda_{yz}P_y\chi_{yy}^{P}M_z\chi_{zz}^{M} \tag{3.2}$$

$$\alpha_{zy} = \alpha_{zy}^{(1)} + \alpha_{zy}^{(2)} = -g_{yxz}\chi_{zz}^{P}L_x\chi_{yy}^{M} - 4\varepsilon_0\lambda_{zy}P_z\chi_{zz}^{P}M_y\chi_{yy}^{M} \tag{3.3}$$

Figures 3.4 (a-f) shows the DFT-computed α_{yz} and α_{zy} values as a function of a_{ip} in Cm, $I4mm$, and $Imm2$ phases. Such figures also report the corresponding fitted values of Eqs. (3.2) and (3.3) for which we employ the dielectric and magnetic susceptibility tensor components and polarization values as computed from DFT (and that are depicted in Fig. 3.5) and allow λ_{yz}, λ_{zy}, g_{zxy} and g_{yxz} to be free fitting parameters. Note that, since there is

a weak ferromagnetism M_y in SBMO system but along the y-direction in $I4mm$, $\alpha_{yz} = \alpha_{yz}^{(1)}$ in $I4mm$. Similarly, $\alpha_{zy} = \alpha_{zy}^{(1)}$ in both Cm and $Imm2$ states because only M_z is non-zero in these two states. One can see that the DFT-obtained linear ME coefficients are well fitted by Eqs. (3.2) and (3.3), which demonstrate their relevance and applicability. As also shown by Figs. 3.4(a,d,f), using both terms, rather than the only first one, of Eqs. (3.2) and (3.3) typically allows to better reproduce the computed linear ME coupling coefficients, α_{zy} in $I4mm$, α_{yz} in Cm and α_{yz} in $Imm2$, as also found for the case of $BiFeO_3$ [23]. However, such agreement between the DFT-obtained and fitting has to be taken with a grain of salt, once considering the error bars of the DFT values.

Now that we can see that Eqs. (3.2) and (3.3) can reproduce the DFT-obtained linear ME coefficients quite well, one would need to look in details into the strain-induced behaviors of the dielectric and magnetic susceptibility tensors components, in order to understand large values of ME coefficients since Eqs. (3.2) and (3.3) show that linear ME coefficients are linearly proportional to the dielectric and magnetic susceptibility tensors components. In order to look in details, we show the calculated dielectric susceptibility tensor components χ_{yy}^P and χ_{zz}^P of SBMO films throughout the studied epitaxial strain range in Fig. 3.5(a). One can see that χ_{yy}^P and χ_{zz}^P adopt large values at the $I4mm$ to Cm and Cm to $Imm2$ phase transition points, respectively, which is also in-line with the softening of the zone-center optical frequency displayed in the inset of Fig. 3.2(a). However, χ_{yy}^M and χ_{zz}^M values adopt their minimum values at these transition points and remain mostly unchanged throughout the Cm phase (see Fig. 3.5(b)). χ_{yy}^M and χ_{zz}^M values are found by extracting the slope of the overall linear change in the total magnetic moment with respect to the applied magnetic fields at each a_{ip}. For that, we show in Fig. 3.6, the change in the total magnetic moment along the y-axis (left panels) and z-axis (right panels) when a magnetic field is applied along the y-axis and z-axis, respectively, for SBMO films with the following in-plane lattice constants, a_{ip}: 3.859$\mathring{A}$ ($I4mm$), 3.869$\mathring{A}$ (Cm), 3.889$\mathring{A}$ (Cm), 3.905$\mathring{A}$ (Cm), and 3.929$\mathring{A}$ ($Imm2$). Overall and as demonstrated here, the large values of the α_{yz} of 38.8 ps/m and α_{zy} of 24.8 ps/m linear ME

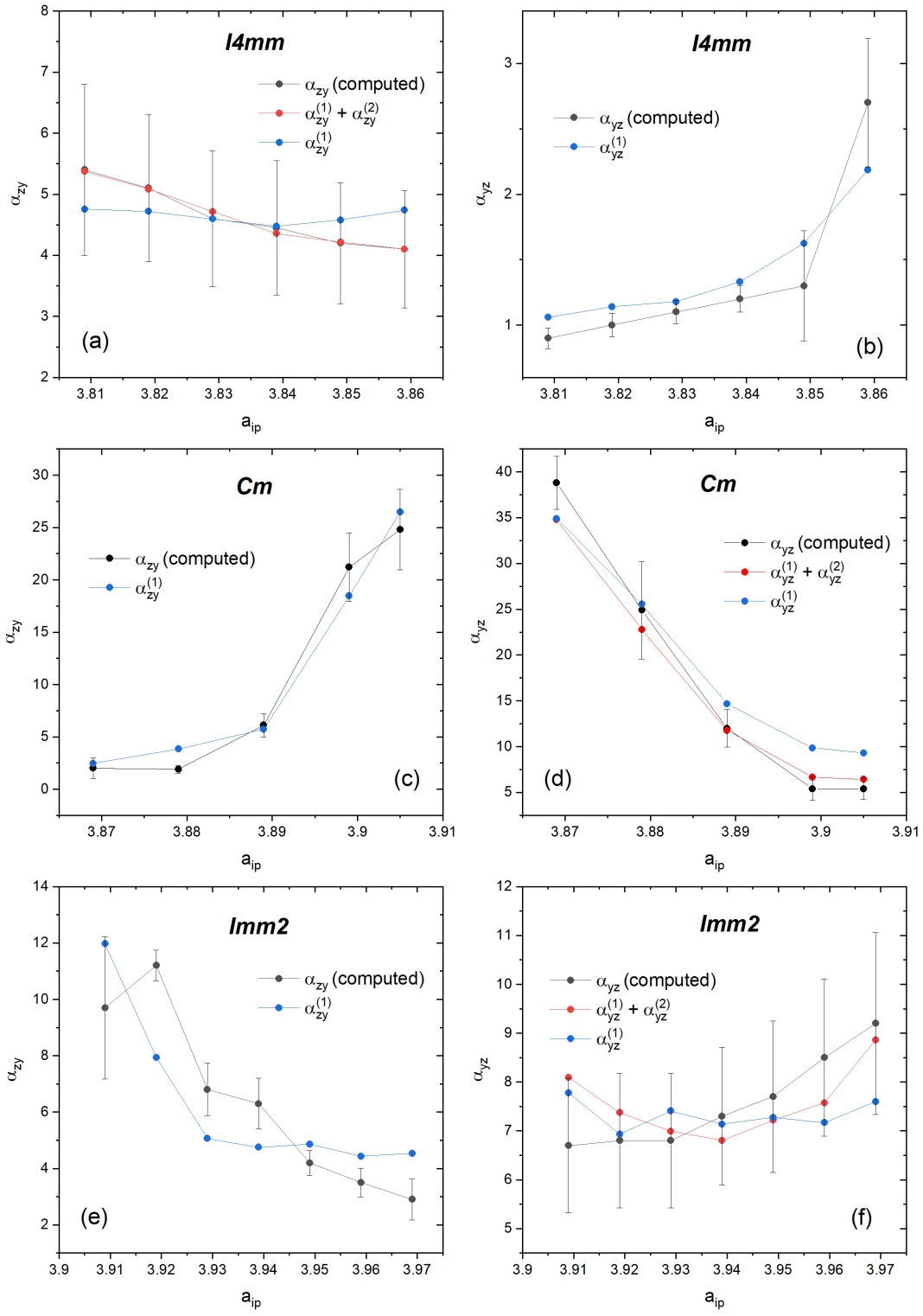

Figure 3.4: Computed linear magnetoelectric coupling coefficients, α_{yz} and α_{zy}, as a function of a_{ip} with its corresponding fitted values from Eqs. (3.2) and (3.3) in the $I4mm$, Cm, and $Imm2$ phases

coefficients are found to be directly correlated with the large values of χ^P_{yy} and χ^P_{zz} near phase transition points, respectively. Note that it is known that many structural phase transitions associated with lattice softening result in the divergence of the dielectric susceptibility due to the softening of the force-constant matrix at the phase transition, and that such divergence is also consistent with the electrical polarization acquiring/annihilating some of its components. For example, the creation/annihilation of the z-component of the polarization can lead to a large χ^P_{zz}, while a large χ^P_{yy} can originate from the appearance/disappearance of the y-component of the polarization. In other words, Eqs. (3.2) and (3.3) tell us that one can design multiferroic materials with a high linear magnetoelectric coefficient when inducing structural transitions that are accompanied by large changes in dielectric susceptibilities, as numerically confirmed here and as implied by previous works [16, 23, 25, 88–90]. Also, it is worth to note that Eqs. (3.2) and (3.3) imply that large linear ME coupling can also be reached at magnetic phase transitions that are accompanied by a dramatic increase in the magnetic susceptibility, which is not the case in the present study.

Furthermore, Fig. 3.5(a) shows that χ^P_{yy} in $Imm2$ and χ^P_{zz} in $I4mm$ decrease when a_{ip} is larger than $3.91\mathring{A}$ and smaller than $3.86\mathring{A}$, respectively. However, in contrast, as shown in Fig. 3.2(b), α_{yz} in $Imm2$ state and α_{zy} in $I4mm$ state are found to concomitantly increase at these a_{ip} regimes. Such results is found to be related to the magnetic susceptibility and polarization. In fact, Fig. 3.5(b) shows the magnetic susceptibility tensor components χ^M_{yy} and χ^M_{zz} of SBMO films under epitaxial strain while its inset shows the polarization as a function of a_{ip}. As one can see, all magnetic susceptibility tensor components increase as a_{ip} decreases below $3.859\mathring{A}$, and as a_{ip} increases above $3.909\mathring{A}$ (note that this is also in agreement with our previous study [5] that magnetic phase transition points are getting close as a_{ip} decreases below $3.859\mathring{A}$, and as a_{ip} increases above $3.909\mathring{A}$). Moreover, P_z in $I4mm$ and P_y in $Imm2$ also increase as a_{ip} decreases below $3.859\mathring{A}$ and increases above $3.909\mathring{A}$, respectively. The increases in χ^M_{yy} and P_z in the $I4mm$ state and of χ^M_{zz} and P_y in the $Imm2$ state are fully consistent with the corresponding increase in α_{zy} in the $I4mm$ state and α_{yz} in the

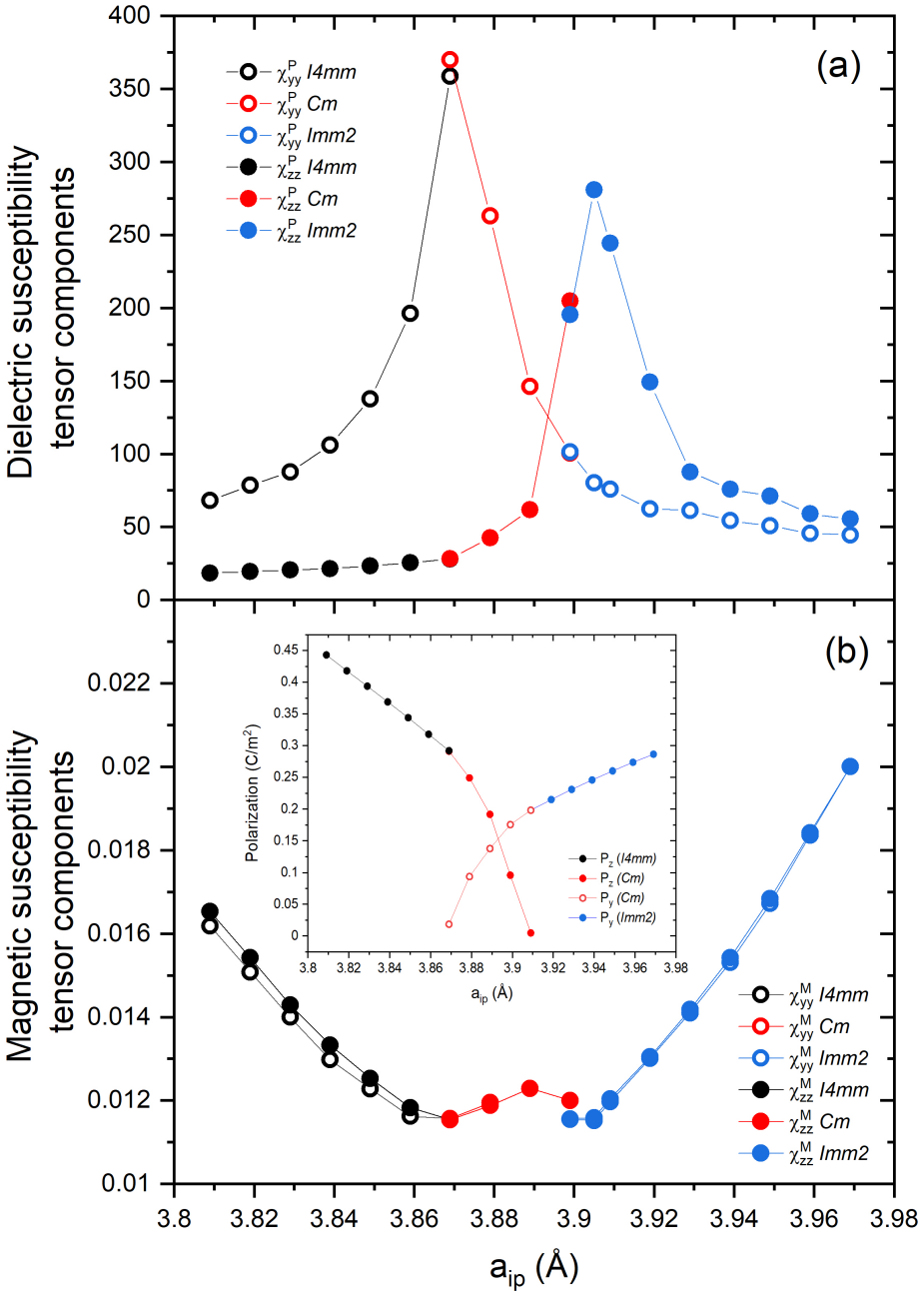

Figure 3.5: Dielectric (a) and magnetic susceptibility (b) tensor components of epitaxial (001) SBMO films as a function of a_{ip} in $I4mm$, Cm and $Imm2$ states. The inset in Panel (b) shows the polarization values of SBMO films as a function of a_{ip}.

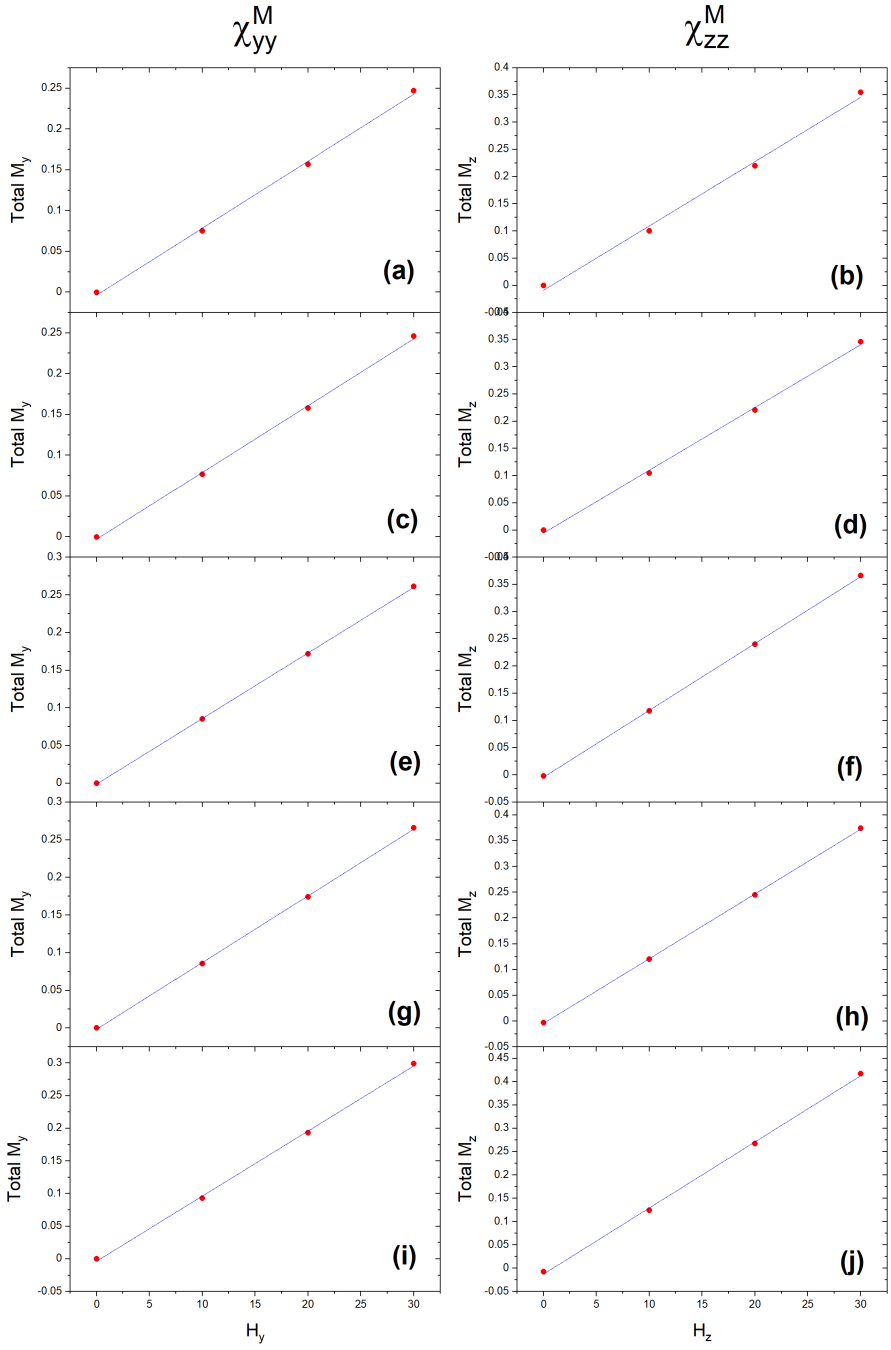

Figure 3.6: The change in total magnetic moment along the y-axis (left panels) and the z-axis (right panels) when magnetic fields are applied along the y-axis and z-axis, respectively, for SBMO films with in-plane lattice constants: (a,b) a_{ip}, of 3.859$\mathring{A}$ ($I4mm$); (c,d) 3.869$\mathring{A}$ (Cm); (e,f) 3.889$\mathring{A}$ (Cm); (g,h) 3.905$\mathring{A}$ (Cm); and (i,j) 3.929$\mathring{A}$ ($Imm2$).

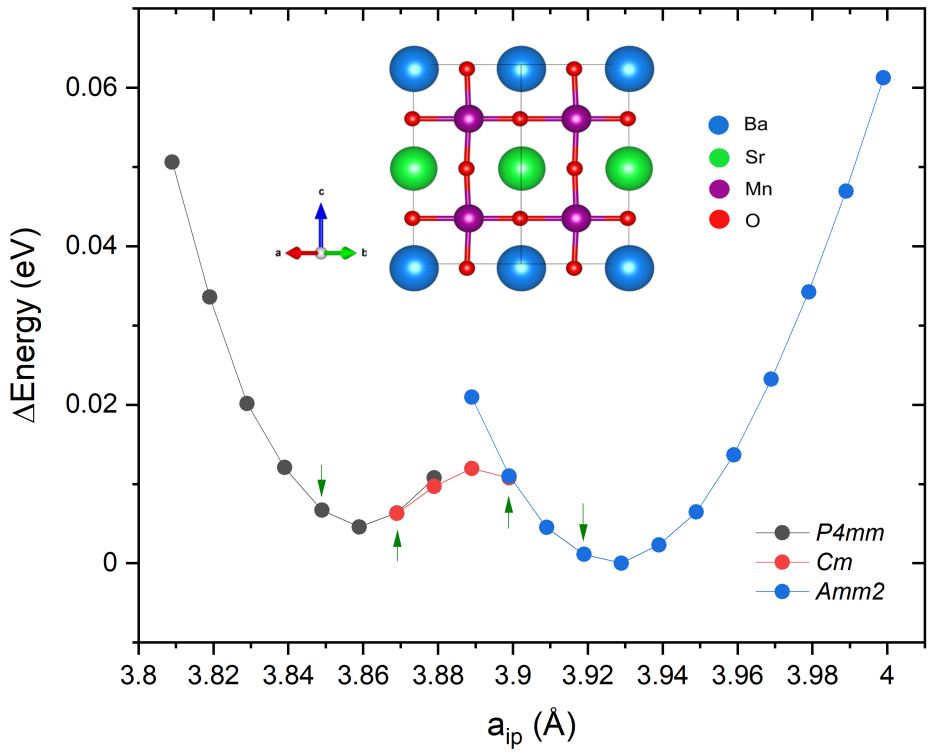

Figure 3.7: The total energy of SBMO films as a function of their in-plane lattice parameter in the $P4mm$, Cm, and $Amm2$ structural states, for the layered chemical arrangement (DL) as shown in the inset. The zero of energy corresponds to the lowest energy structure, having $a_{ip} = 3.929\mathring{A}$. Note that the a axis shown here lies along the pseudocubic [–1–10] direction, while the b axis is along [1–10]. The c axis is parallel to the out-of-plane [001] direction.

$Imm2$ state, according to the Eqs. (3.2) and (3.3).

Lastly, we considered an another chemically-ordered structure with alternating (001) layers made of Ba or Sr atoms, which is denoted as DL (double layers). Such structure is depicted as the inset of Fig. (3.7). Figure (3.7) shows the total energy as a function of the in-plane lattice constant for the G-AFM magnetic configuration of such structure. Structures with in-plane lattice constants of $3.849\mathring{A}$, $3.869\mathring{A}$, $3.899\mathring{A}$, and $3.919\mathring{A}$ were chosen to study their linear ME coupling coefficient and are indicated by arrows in Fig. (3.7). Furthermore, we also found that the α coefficients sharply get enhanced near the borders of the MPB, exactly as we revealed in the structure with Rock-Salt ordering. Specifically, α_{yz} is predicted

to be 4.5 ps/m, 1.6 ps/m, 82,8 ps/m, and 7.1 ps/m for in-plane lattice constants of 3.849$\mathring{A}$, 3.869$\mathring{A}$, 3.899$\mathring{A}$, respectively. Moreover, α_{zy} is predicted to be 1.3 ps/m, 56.3 ps/m, 2.0 ps/m, and 6.5 ps/m for in-plane lattice constants of 3.849$\mathring{A}$, 3.869$\mathring{A}$, 3.899$\mathring{A}$, respectively. Both α_{yz} and α_{zy} get therefore significantly enhanced at different in-plane lattice constants (at the two different borders of the MPB) which is the same qualitative result as we found for the Rock-Salt ordered structure. Such results reveal that the enhancement of ME coupling at the phase transition point near the borders of the MPB is not dependent on the chemical ordering of the system.

3.5 Summary

In this work, we have computed the linear magnetoelectric coupling coefficients of epitaxial (001) SBMO films as a function of their a_{ip} arising from substrates. In particular, we found a large enhancement of α_{yz} and α_{zy} values at the phase transition points from $I4mm$ to Cm and $Imm2$ to Cm states, respectively. With that, we verified the general approach of employing strain-engineering to induce a large enhancement in ME coupling in the MPB region. Such enhancements are found to be directly related to the sudden increase of the dielectric susceptibility at the phase transition points. Magnetic susceptibility was also determined to influence the linear magnetoelectric coupling, but for smaller linear magnetoelectric coefficients. However, it is noteworthy to mention that the linear magnetoelectric coupling can also be enhanced with the increase in magnetic susceptibility such as the one found in ferromagnetic MPB [91]. Note also that the effect of the interface with the substrate on the electronic, magnetic properties and magnetoelectric coupling coefficient is ignored in this study and it may be a topic of future study. We hope that our predictions in this study would help in further understanding magnetoelectric effects, in general, and bring attention to single-phase multiferroics with MPB, in particular, to achieve highly-desired colossal magnetoelectric responses.

4 Magnetoelectricity at the domain wall of Rare-earth Iron Garnet systems

4.1 Introduction

As mentioned in Chapter 1.2 and shown in Fig. (1.2), magnetoelectric coupling does not have to manifest in multiferroics and one of the exemplary systems is studied in this chapter. As mentioned previously in Chapter 1.2, the ME coupling effect of bulk materials is typically either small or achievable at low cryogenic temperatures [92]. Thus, the search for high-temperature ME material has led to new trends such as magnetoelectricity on the level of domain [93–95] and domain wall [96–104]. The magnetic domain walls (DW) are the natural interfaces between regions that are homogeneously magnetized, and it was previously predicted that Néel-type DW should have an electric polarization and react to an electric field in ferrite garnets [105]. Controlling the properties of DW offers great potential for technological applications such as memory devices, spintronics, and communications [98, 106]. Recently, there have been reports of experimental observations of a giant ME effect in epitaxial rare-earth iron garnet (RIG) films [15,17–20] [105, 107–110] and such ME effect was demonstrated as optical nanoshutter in Ref. [111].

Despite its experimental observation, it is striking to find out that the microscopic origin and mechanism behind such ME effect at the magnetic DW of RIG systems is still in dispute and there are several hypotheses: (i) Dzyaloshinskii-Moriya-like interactions [112] such as inhomogeneous magnetoelectric interaction due to the chirality of magnetic spin arrangements [110, 113, 114], or (ii) the local decompensation of the antiferroelectric structure in the DW, which involves rare-earth and iron ions exchange interaction [10,14,37] [100, 104, 115]. One can also wonder if there is any other mechanism driving such ME effect and what are the precise contributions of each ions, and of their possible magnetic moments, on such electrical polarization.

In this work, our objective is to use a first-principles approach to further confirm that

magnetic DW does possess an electric polarization in RIG systems, as well as, to resolve all the issues of dispute on the mechanism behind the ME effect. In particular, our objectives are to: (1) find out whether the magnetism of the rare-earth element is not crucial for this magnetoelectric effect; (2) determine the main contributing element to the electrical polarization at the DW; (3) reveal whether such ME effect can be explained with the aforementioned mentioned hypothesis, and, if not, uncover the driving mechanism thanks to our first-principles results.

4.2 Structural and Magnetic Properties

Rare-earth Iron Garnets (RIG) with chemical formula of $Re_3Fe_5O_{12}$ is a insulator with a ferrimagnetic ordering. RIG have been extensively studied, due to their complex magnetic structure, high Curie temperature ($T_C > 500K$), relatively large band gap (≈0.8eV) and chemical stability [8, 100, 116–125]. Ferrimagnetic ordering in RIG originates from (i) the strong antiferromagnetic coupling between an inequivalent number of Fe ions that occupy the tetrahedral and octahedral sites in a unit cell (ratio 3:2), and (ii) rare-earth ions that sit at the dodecahedral sites with a finite magnetic moment that has been reported to be coupled antiferromagnetically with the tetrahedral Fe moment [121, 126]. Furthermore, the temperature dependence of the magnetic sublattices of RIG is different, thus as temperature decreases the magnetization of the Re sublattice increases greatly (it is more sensitive to temperature than the Fe sublattice) and can lead to the appearance of the so-called compensation temperature (T_M) in some RIGs (some rare-earth do not have strong magnetic moments from f-electrons), where the net magnetization vanishes [8, 118, 121]. Compensation of magnetization has recently gained interest due to its possible applications in information storage, thermomagnetic switching and laser induced switching [127–129]. Note that we studied the magnetization compensation temperature properties of RIGs under epitaxial strain and report the result in Chapter 5.

In this study, we chose to study $2 \times 1 \times 1$ and $4 \times 1 \times 1$ supercells of Gadolinium Iron

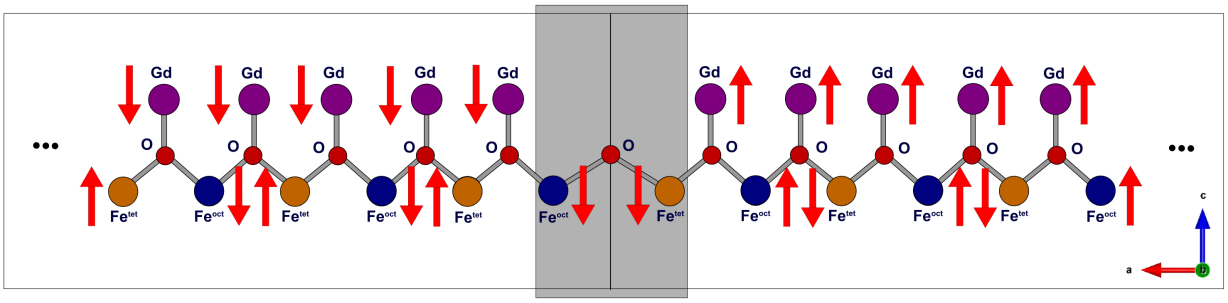

Figure 4.1: Simple sketch of magnetic arrangement used for all supercells with DW at the center for RIG systems (Note that this sketch is a much-simplified version of the more complex magnetic interactions in RIG systems). Arrows represent the magnetic moments of both octahedral and tetrahedral Fe and Gd ions (in "without-f" case, spins at the Gd sites are not considered). The gray area in the middle and three dots at both ends represent the DW and continuation of magnetic arrangement within that domain.

Garnet (GIG) systems that have a magnetic DW in the middle (along the pseudo-cubic [100] a-axis) of these supercells. Figure 4.1 shows a simplified sketch of spin arrangements that are considered in the supercells of this study. The gray area at the center represents the DW and the magnetic configuration inside each domain (left and right sides of the DW) consists of tetrahedral Fe (Fe^{tet}) ions being arranged antiferromagnetically with respect to the other two sublattices (octahedral Fe, Fe^{oct}, and Gd ions). Such spin arrangement was reported to be the lowest energy collinear spin configuration for GIG bulk [119] and is in agreement with experiments [121, 126]. Furthermore, as shown in Fig. 4.1, the two domains of the studied supercells have a reversed magnetic configurations respect to each other (thus, the net magnetization of the supercell is zero) and the a axis is the direction that is normal to the DW.

4.3 Methods

Here, all calculations are carried out within the framework of DFT as implemented in VASP [130] using the projector augmented-wave potentials [131]. The following electrons are always treated as valence states: O 2s and 2p, and Fe 3d. On the other hand, we used two different schemes for the valence electrons of Gd: 4f, 5s, 5p, 5d and 6s where f-electrons are thus

treated as valence electrons (and, consequently, magnetization arising from Gd ions can occur) versus "only" 5p, 5d and 6s where f-electrons are treated as core electrons and thus magnetic ordering of Gd ions is not accounted for. The generalized gradient approximation (GGA) together with the revised Perdew-Burke-Ernzerhof exchange-correlation functional for solids (PBEsol) [132] is employed with an effective Hubbard U parameter of 4eV for the localized 3d electrons of Fe ions and U = 4eV for the localized 4f electrons of Gd ions when these 4f electrons are treated as valence electrons. Such values were demonstrated to provide accurate results [119, 129, 133–135]. We performed all our calculations at a collinear level, implying that spin-orbit coupling effects (such as Dzyaloshinskii-Moriya-like interactions [59, 136]) are not incorporated in the simulations. As we show here which is at odds with previous beliefs [92, 100, 104, 115, 137], such choices of our calculations does not prevent the occurrence of electrical polarization at the DW of the studied supercell. All structural degrees of freedom are allowed to relax. Moreover, the energy cutoff of 500 eV is used, and Monkhorst-Pack k-point mesh is chosen to be $2 \times 4 \times 4$ for the $2 \times 1 \times 1$ supercell and $1 \times 4 \times 4$ for the $4 \times 1 \times 1$ supercell. Structural relaxations are performed until the Hellmann-Feynman force on each atom is less than 0.005 $eV/\mathring{A}$, and the polarization is calculated by the Berry-phase method [63].

4.4 Results

We show the polarization of the studied GIG supercells when we consider f-electrons and do not consider f-electrons of the Gd ions as valence electrons in Table (4.1). We denote both cases as the "with-f" and the "without-f", respectively. Surprisingly, in both cases and for both considered supercells, the existence of magnetic DM in GIG system gives rise to a electric polarization. Such polarization was further numerically found to develop along the normal to the DW, thus inducing an orthorhombic $Iba2$ space group. In addition to the above-mentioned supercell sizes, we also considered a GIG supercell possessing DW lying along the pseudo-cubic [110] direction and found a DW-induced polarization there along

such normal too. In that case, the crystallographic space group is monoclinic $P2$. Such results reveal that there is a magnetic DW induced polarization in GIG system regardless of the normal direction of the formed DW and found that the polarization is consistent with previous works on RIGS [92, 100, 104, 105, 108, 110, 113, 115, 137–146] and contrasts with the paraelectric nature of GIG monodomain.

Table 4.1: Polarizations of different supercells of RIG systems with DW at the center of the supercells.

	Supercell size		Polarization (mC/m^2)
GIG	$2 \times 1 \times 1$	with-f	-2.133
		without-f	-5.117
	$4 \times 1 \times 1$	with-f	-1.100
		without-f	-2.553
LuIG	$2 \times 1 \times 1$	filled f-shell	-2.458
YIG	$2 \times 1 \times 1$	empty f-shell	-2.157
GIG	$1 \times 1 \times 2$	with-f	-2.250

Most importantly, Table (4.1) shows that the "without-f" case also yields an electric polarization, and it is more than twice as large as that of the "with-f" case. For example, the $4 \times 1 \times 1$ supercell of GIG where f-electrons are considered as valence electrons ("with-f" case) has a total polarization of 0.001 C/m^2 but, when f-electrons are frozen as core electrons ("without-f" case), the total polarization increases to 0.003 C/m^2. It is also noteworthy to mention that for the latter case, the polarization is larger by one order of magnitude than the polarization typically induced in improper ferroelectrics ($< 100\mu C/m^2$) [11, 147]. Furthermore, one can see that the polarization of the $4 \times 1 \times 1$ supercell is about half of the polarization of the $2 \times 1 \times 1$ supercell in both cases (with and without f-electrons cases), which clearly confirms a DW-induced mechanism. Note that an increase in the magnitude of the polarization with a decrease of the ratio of the DW volume over the total volume was also reported in Refs. [115, 148]. The resulting fact that the polarization induced and is even enhanced in the "without-f" case with respect to the "with-f" situation automatically implies that the DW-induced polarization in RIG systems does not have to mainly arise

from the magnetism of rare-earth ions, and such fact is in contrast to the assumptions made in Refs. [92, 100, 104, 115, 137]. Moreover, to definitely assert and confirm such important point, we conducted similar calculations of $2 \times 1 \times 1$ supercells made of Yttrium Iron Garnet (YIG) and Lutetium Iron Garnet (LuIG) systems and reported their results in Table (4.1). Recalling that Yttrium and Lutetium have an empty f-shell and a filled f-shell, respectively, and therefore cannot possess magnetism from the f-shell electrons. Thus, as revealed in Table (4.1), the existence of polarization in the $2 \times 1 \times 1$ supercells of YIG and LuIG systems (i) indeed indicates that the DW-induced polarization in RIG systems does not originate from the magnetism of rare-earth ions, and (ii) it further confirms that such DW-induced polar effect should likely occur in any RIG systems with DW.

Now, let us study this mechanism behind this DW-induced polarization effect in RIG systems. In order to do that, we analyzed the atomic displacements of the relaxed $4 \times 1 \times 1$ supercell structure of GIG with the DW at the center, with respect to its corresponding high-symmetry structure (supercell structure without DW at the center). Note that such $4 \times 1 \times 1$ supercell is our largest studied supercell and can thus technically have the widest DW. All ions are found to have displacements along all three Cartesian directions, but the net displacement of any type of ion along the direction that is not normal to the DW nullifies each other when averaging over the entire supercell. Such finding was further confirmed with the fact that the Berry phase calculations not yielding any macroscopic polarization along the b (pseudo-cubic [010]) and c (pseudo-cubic [001]) directions. The ionic displacements along a-direction (pseudo-cubic [100]) which is normal to the DW, are shown at the top panels of Fig. (4.2). Results show that any type of ion that is located near the DW center is getting largely displaced, unlike the ions that are located away from the DW. Furthermore, let us look at the relative displacement of these Fe^{oct} ions with respect to those of the monodomain case. Each Fe^{oct} is surrounded by six Fe^{tet} ions that are its first-nearest neighbors as shown in Fig. (4.3(a)) and, in the high-symmetry centrosymmetric structure, bulk structure, this coupling is antiferromagnetic in nature. However, when a DW is introduced in the system,

symmetry breaks and some antiferromagnetic couplings at the DW become ferromagnetic (see Fig. (4.3(b)), realizing that the normal of the DW is along the a-axis). As shown in Figs. (4.3 (b,c,d)), with the introduction of the DW, Fe^{oct} ions are getting displaced away from their ferromagnetic nearest-neighbor Fe^{tet} ions. More precisely, Fe^{oct} ions at one side of the DW are getting displaced further than the Fe^{oct} ions that are on the other side of the DW because one type has two ferromagnetic neighbors while the other type has only one ferromagnetic neighbor (see Fig. (4.3(b))b). Figures (4.3 (c) and (d)) also further confirm that the net displacement of Fe ions along the b and c directions is getting canceled when averaging over the entire supercell.

Next, we also compute the $Fe^{oct}-O-Fe^{tet}$ angles (see Fig. (4.1) for the schematization of these angles) and report them on the bottom panels of Fig. (4.2) for both with (Panel c) and without f-electrons (Panel d) cases. Such angles are also compared with the corresponding angles for a GIG monodomain and they are 126.78° and 126.25° for both with and without f-electrons cases, respectively. The results reveal a significant change in $Fe^{oct} - O - Fe^{tet}$ angle near the DW. In particular, this angle can be reduced by about 1.2-1.3 degrees from the aforementioned monodomain values when the involved octahedral and tetrahedral Fe ions are ferromagnetically (FM) coupled to each other at the DW. Note that the magnetic interaction between first-nearest neighbor octahedral and tetrahedral Fe ions is predicted to be the strongest among all interactions in GIG monodomain [135]. We further found that such decrease in the $Fe^{oct} - O - Fe^{tet}$ angle is accompanied by an increase in the distance between Fe^{oct} and Fe^{tet} ions at the DW, and among all oxygen ions, the ones involved in these $Fe^{oct} - O - Fe^{tet}$ angles at the DW are those that are displaced the most. Now, let us look at the estimation of ionic part of the polarization for the $4 \times 1 \times 1$ supercell by multiplying the net displacement of each ion along the a-direction by its ideal ionic charge and the results are reported in Fig. (4.4). The estimated ionic parts of the polarization (along the a-direction) of Fe and Gd ions have opposite signs and almost identical values, therefore nearly nullifying each other. Thus, in the first approximation, the main contributor

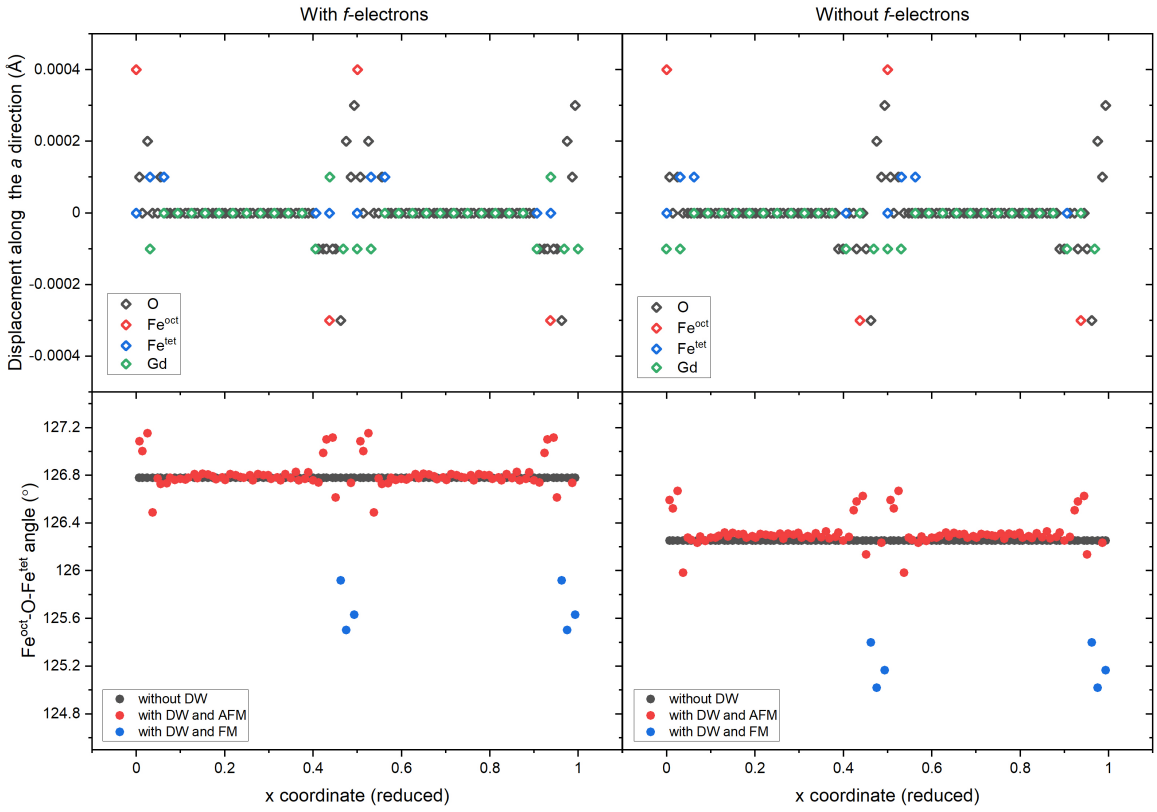

Figure 4.2: Results for the GIG 4x1x1 supercell: Top panels (a,b) show the displacements of all ions along the a direction (which is normal to the DW) when f-electrons are treated as valence and core electrons, respectively; bottom panels (c,d) show the $Fe^{oct}-O-Fe^{tet}$ angles when f-electrons are treated as valence and core electrons, respectively. In panels c and d, "without DW" corresponds to $Fe^{oct}-O-Fe^{tet}$ angles in a monodomain; "with DW and AFM" characterizes the antiferromagnetic $Fe^{oct}-O-Fe^{tet}$ angles in the multidomain; and "with DW and FM" display the ferromagnetic $Fe^{oct}-O-Fe^{tet}$ angles in the multidomain.

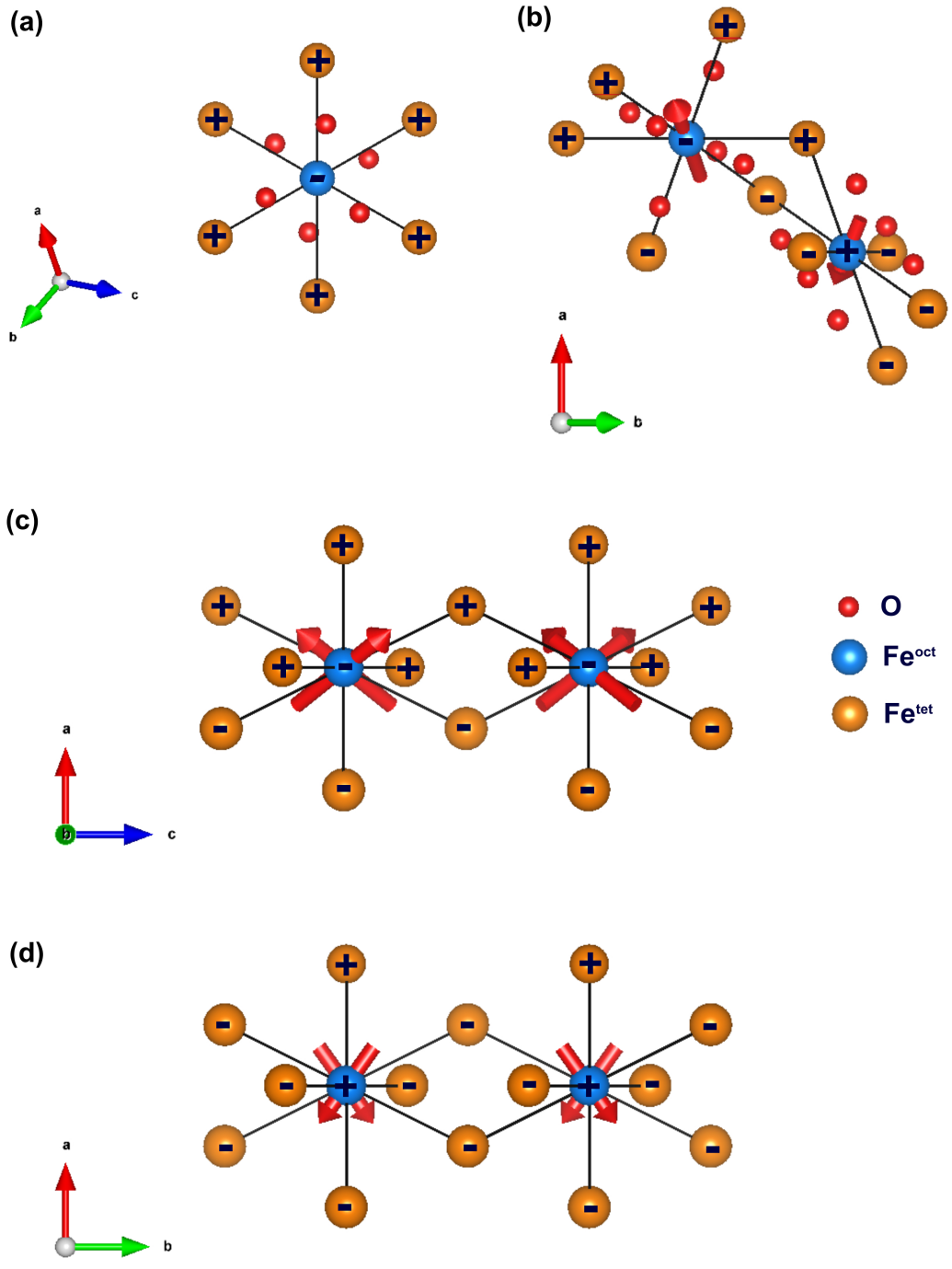

Figure 4.3: The relative displacement of Fe^{oct} ions, that are depicted by utilizing red arrows in (a) the high-symmetry centrosymmetric structure of GIG monodomain versus (b) near the DW; (c) at one side of the DW; (d) at the other side of the DW in a GIG multidomain. The oxygen ions are further indicated in Panels (a) and (b) but are omitted for clarity in Panels (c) and (d). The positive and negative signs refer to the up and down directions of the magnetic moments of the Fe ions.

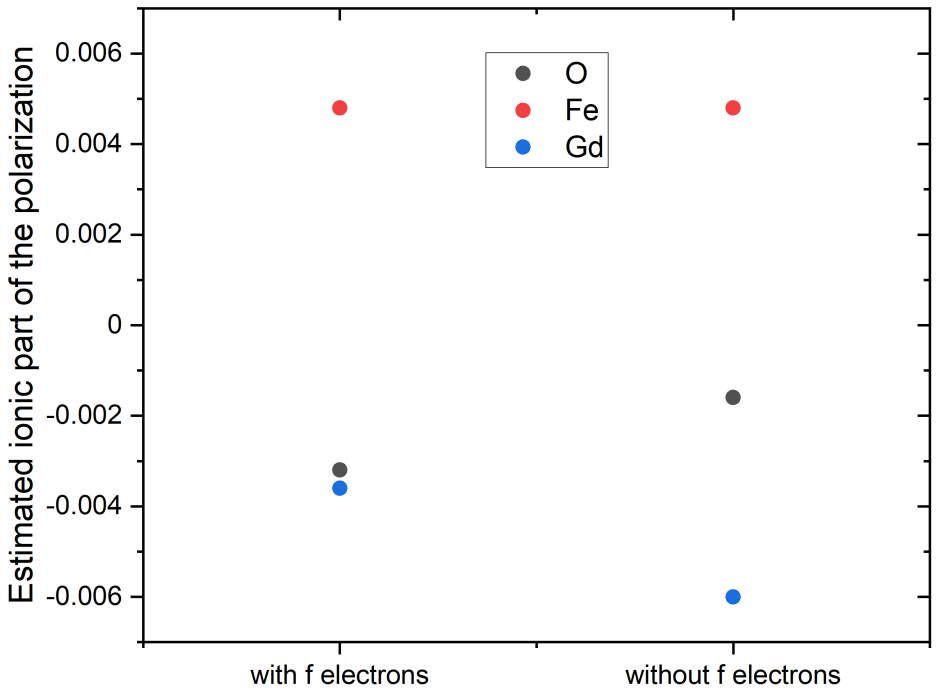

Figure 4.4: Estimated contribution of each type of ion to the ionic part of the polarization along the a direction. Left and right sides are when f-electrons are treated as valence and core electrons, respectively.

to DW-induced polarization is predicted to be the displacement of O ions.

So far, we have shown that DW-induced polarization effect in RIG systems (i) can manifest in any RIG system with DW, (ii) does not originate from the magnetism of rare-earth ions, and (iii) at first approximation, the displacement of O ions are the main contributor to this DW-induced polarization effect. Now let us look at the origin of this effect and try to reveal the microscopic mechanism behind it. In order to do that we employ the unified model for the spin-order induced ferroelectricity [149–151]. However, as we shown before, spin-orbit coupling is not necessary to induced such ME effect and is not considered our calculations. Thus, the spin-order-induced polarization can be written as $\overrightarrow{P} = \sum_{<i,j>} \overrightarrow{P}_{es}^{ij} \overrightarrow{S}_i \cdot \overrightarrow{S}_j$ where the summation is over all the spin pairs and $\overrightarrow{P}_{es}^{ij}$ is the polarization coefficient vector associ-

ated with the $< i, j >$ spin pair. The results from Fig. (4.2) hint toward a link between the DW-induced polarization and the ferromagnetic interaction between octahedral and tetrahedral Fe ions, thus we only look at such ferromagnetic interactions at the DW and only take into account these ferromagnetic pairs in $\overrightarrow{P} = \sum_{<i,j>} \overrightarrow{P}_{es}^{ij} \overrightarrow{S}_i \cdot \overrightarrow{S}_j$ equation. Hence, in order to calculate the main component, $\overrightarrow{P}_{es}^{ij}$, we constructed a 160-atom supercell of a GIG system where f-electrons are treated as core electrons (no magnetization from f-shell electrons) and with a DW at the center. Note that including f-electrons does not prevent the polarization from happening and such calculations are computationally heavy. We relax this supercell with the DW and then used the four-state energy mapping method [60, 150] to find the polarization coefficient vectors for all the ferromagnetic interactions between octahedral and tetrahedral Fe ions at the DW. We overall calculated 12 polarization coefficient vectors that involved in three different four-fold-degenerate-pairs. For all ferromagnetic spin pairs at the DW, we let $\overrightarrow{S}_i \cdot \overrightarrow{S}_j = 1$. Our results for the spin-order-induced polarization equation, $\overrightarrow{P} = \sum_{<i,j>} \overrightarrow{P}_{es}^{ij} \overrightarrow{S}_i \cdot \overrightarrow{S}_j$, yield a net polarization of 0.01 C/m^2 along the a-direction (a direction normal to the DW) with all other components vanishing. Such polarization compares very well with the result from the Berry-phase method [63] (directly calculated with DFT) of this supercell – which is found to be 0.0102 C/m2. Such comparison, therefore, demonstrates the accuracy of our calculations and the validity of the model/equation. The polarization results found using the 160-atom supercell are about twice as larger as that of a $2 \times 1 \times 1$ supercell (320 atoms supercell) shown in Table (4.1) since this latter has a smaller ratio of DW volume over the volume of the supercell. Overall, the value of polarization induced by DW is found to be inversely proportional to the size of the supercell, i.e. $\overrightarrow{P}_{n\times1\times1} = \overrightarrow{P}_{1\times1\times1}/n$.

Furthermore, we show the polarization coefficient vector (in blue colors) and the displacement of O ions (in red colors) that are involved in the ferromagnetic $Fe^{oct} - O - Fe^{tet}$ angles at the DW in Fig. (4.5). One can see that $\overrightarrow{P}_{es}^{ij}$ and oxygen displacements in Fig. (4.5) are basically along the same direction for any of such oxygen ions. Such fact confirms

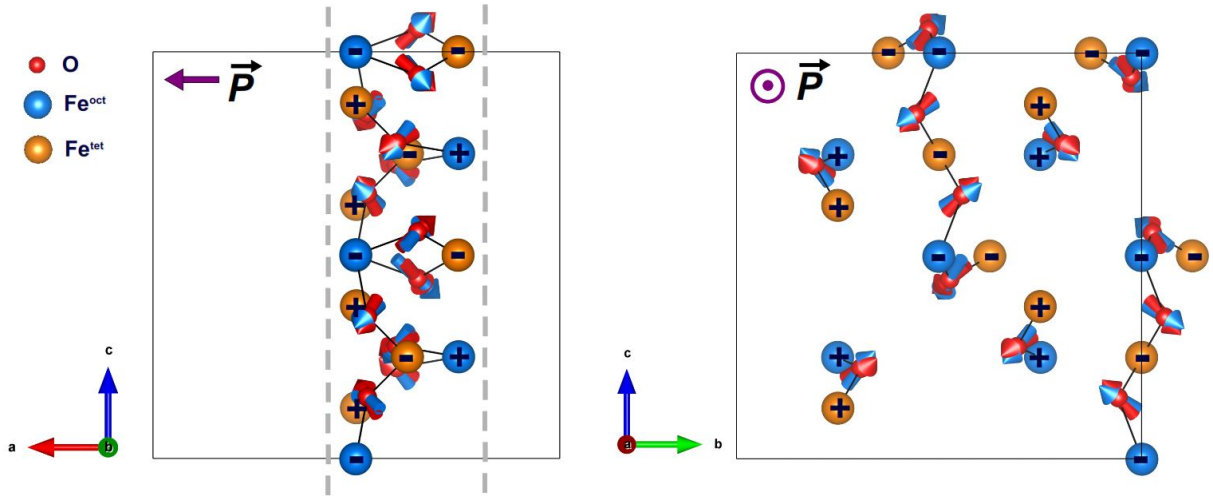

Figure 4.5: The polarization coefficient vectors (blue) and displacement vectors (red) of O ions around the DW, having a normal along the a-axis, of a 160-atom supercell. The left panel concerns the (a,c) plane (thus possessing the DW's normal) while the right panel displays the (b,c) plane (that is thus perpendicular to the DW's normal). The "+" and "-" signs refer to the up and down directions of the magnetic moments of the Fe ions. The gray dashed line and purple arrows represent the DW region and direction of the electric polarization, respectively.

that the displacements of O ions that are involved in the ferromagnetic $Fe^{oct} - O - Fe^{tet}$ angles at the DW are the main contributors to the polarization and such effect found to be originated from the ferromagnetic interaction between two types of Fe ions (octahedral and tetrahedral) at the DW. Thus, such facts reveal that the symmetric exchange-striction mechanism described by $\overrightarrow{P} = \sum_{<i,j>} \overrightarrow{P}_{es}^{ij} \overrightarrow{S}_i \cdot \overrightarrow{S}_j$, is the mechanism behind the formation of DW-induced electric polarization in RIG systems.

Now that we show the origin of the DW-induced electric polarization in RIGs is due to the ferromagnetic interaction between octahedral and tetrahedral Fe ions at the DW and such effect does not require complex explanations involving chirality or spin-orbit coupling. Let us employ a simple model of magnetic DW to explain the experimental findings of Ref. [108]. Electric polarization estimated from such experimental observation is $\approx 3 \times 10^{-7} C/m^2$ [108]. Our simple model takes into consideration magnetic moments that are gradually decreasing in magnitude to the center of the DW (in this case, one can only consider the component of

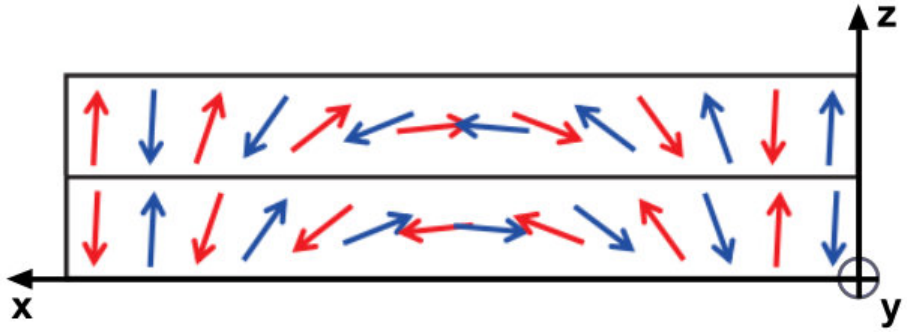

Figure 4.6: Sketch of synthetic antiferromagnetic structure. Blue and red arrows represent the spin directions of both octahedral and tetrahedral Fe ions, respectively.

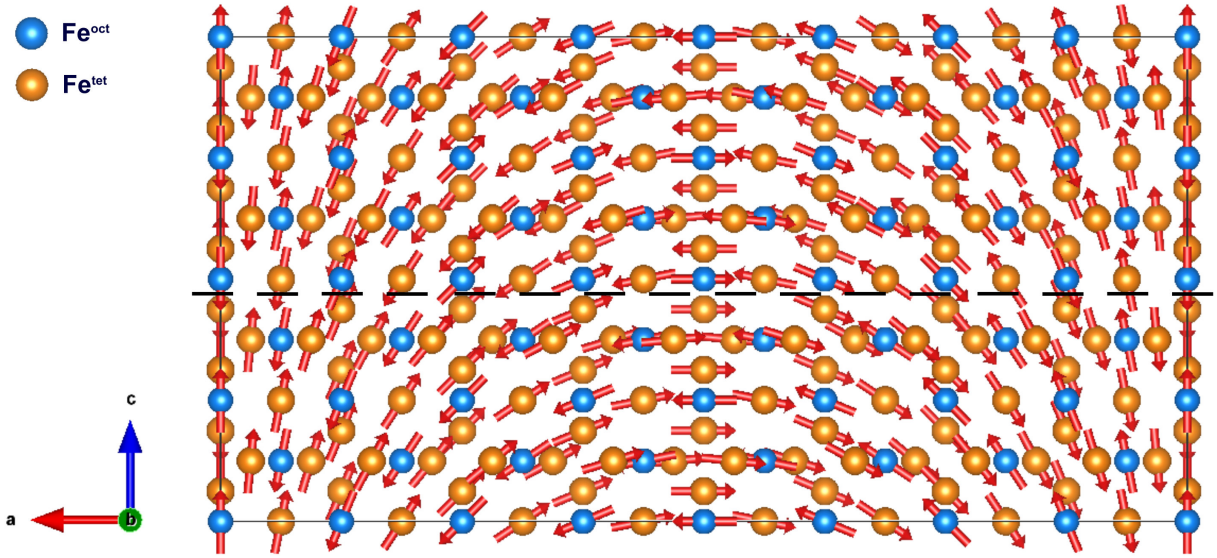

Figure 4.7: $4 \times 1 \times 2$ supercell of GIG mimicking the SAF magnetic structure. Arrows represent magnetic moment directions at each magnetic site and the dashed line represents the interface between two layers.

the magnetic moments along a direction that is perpendicular to the normal of the domain wall). In this way, one can also have ferromagnetic interaction between octahedral and tetrahedral Fe ions at the center of the DW but with a much smaller magnetic moments. For instance, according to the spin-order-induced polarization equation, $\overrightarrow{P} = \sum_{<i,j>} \overrightarrow{P}^{ij}_{es} \overrightarrow{S}_i \cdot \overrightarrow{S}_j$, one can estimate to have electric polarization of $\approx 3 \times 10^{-7} C/m^2$ if the aforementioned component of the magnetic moment of the Fe ions at the center of the DW shrinks to the value of 0.0055 μB, independently of the size of the domain walls or the supercell. Furthermore, to address the importance of DW's normal direction, we take into account [-120] direction that was considered in experimental observation [108]. We estimate the DW-induced polarization of a $2 \times 1 \times 1$ GIG system with a DW's normal direction lying along the pseudo-cubic [-120] direction, using the polarization coefficient vectors in our general model, $\overrightarrow{P} = \sum_{<i,j>} \overrightarrow{P}^{ij}_{es} \overrightarrow{S}_i \cdot \overrightarrow{S}_j$. The estimated polarization for this [-120]-oriented DW is found to be -0.015 C/m^2. Such polarization value is larger than that of the $2 \times 1 \times 1$ supercell with [100]-oriented DW (-0.01 C/m^2) because the DW length is longer in the [-120] DW-oriented case, therefore implying that there are more ferromagnetic interactions between octahedral and tetrahedral Fe ions for the [-120]-oriented DW.

Next, we look into the possibilities of how our finding can be exploited in experimental setups. In order to do that, let us envision two layers of GIG films that have Neel-type DW structure and aligned antiparallel to each other. Note that this type of structure is called "synthetic antiferromagnetic" (SAF) structure and has been used in some recent experimental works [148, 152, 153]. Such structure is illustrated in Fig. (4.6) and any two neighboring magnetic moments of the same Fe ions along the z-direction would be antiparallel to each other and spin rotation direction in the Neel-type DW is reversed between these two layers (up and bottom). Since in this case, DW is along the z-direction, and throughout such DW, especially in the middle of the DW, magnetic moments of octahedral Fe ion in the one layer and the magnetic moments of tetrahedral Fe in the other layer are starting to align along the same direction (see Fig. (4.6)). Therefore, the interface between 2 layers along the DW

or the z-axis will have ferromagnetic interaction between octahedral and tetrahedral Fe ions and such setup is very similar to the DW condition that is considered in our study. In fact, we constructed $4 \times 1 \times 2$ supercells of GIG mimicking the SAF magnetic structure as shown in Fig. (4.7) and estimated the electric polarization using the polarization coefficient vectors, $\overrightarrow{P}_{es}^{ij}$, in our model. Our results yield a DW-induced polarization that is basically aligned along the c-axis (there are small amount of polarization along other directions since there is Neel-type DW in this supercell) and with a value of 0.0368 C/m^2. Note that the $4 \times 1 \times 2$ supercell mostly consists of DWs as shown in Fig. (4.1). Consequently, if one considers much larger supercells, especially along the c-axis (thus decreasing the ratio between the volume occupied by the DW and the volume of the whole supercell), the polarization value will decrease accordingly.

4.5 Summary

Here, we studied different supercells of rare-earth iron garnet systems with domain walls with means of investigation via first-principle calculations. The main results are as follows: (1) all the studied supercells are found to have a DW-induced electrical polarization along the direction of the normal of the domain walls; (2) such polarization neither requires the existence of magnetism at the rare-earth sites nor non-collinear magnetism to exist, which is in contrast to what was previously proposed in previous studies. It rather originates from a (magnetoelectric) symmetric exchange-striction mechanism involving ferromagnetic interactions between octahedral and tetrahedral Fe ions at the DW. Such magnetoelectric mechanism can be explained with the analytical form of $\overrightarrow{P} = \sum_{<i,j>} \overrightarrow{P}_{es}^{ij} \overrightarrow{S}_i \cdot \overrightarrow{S}_j$, which can also be used to compute the electrical polarization for magnetic domains having a more realistic size than the ones chosen here (because of computational limitations). We hope that these findings provide a deeper understanding of origin of magnetoelectricity in RIG systems, and domain wall engineering, and will encourage experimental confirmation of our findings using methods such as PUND (Positive Up Negative Down) [154] that was used in Ref.

[155], or the Dielectric Leakage Current Compensation (DLCC) [156] and the Double-Wave Method (DMW) [157].

5 Epitaxial strain effect on the Curie and magnetization compensation temperatures of RIG systems

5.1 Introduction

As introduced in Chapter 4, rare-earth Iron Garnets have been extensively studied, due to their complex magnetic structure, high Curie temperature ($T_C > 500K$), relatively large band gap (≈0.8eV) and chemical stability [8, 100, 116–125]. And as we showed in Chapter 4, RIGs develop some peculiar magnetoelectric effect when there is magnetic DW in them. Plus, there are other exciting properties that occur in RIGs and are getting more attention in the spintronic community such as the magnetization compensation temperature. The magnetization compensation temperature, T_M, appears due to the different temperature dependence of rare-earth and iron sublattices, as introduced in Chapter 4. Recently, T_M has gained a lot of interest due to its possible applications in information storage, thermomagnetic switching and laser induced switching [121, 127–129]. Thus, tuning such temperature is highly desired for application purposes, especially if one succeeds in bringing T_M to room temperature (i.e., ≈ 300K). In fact, T_M of terbium iron garnet (TIG) has been reported to change from 248.6K to 335K when grown on Gadolinium Gallium Garnet substrate which induces a compressive strain of 0.5% on the TIG films. Such impressive enhancement is believed to be caused by an extrinsic effect, namely the octahedral sites being occupied by a mixture of Fe^{3+} and Tb^{4+} ions in such (111) TIG films [116]. Likewise, the deviation from perfect stoichiometry (which is an extrinsic effect) was reported to be the deriving force behind the strain-induced changes in T_M of RIG films in the 60s and 70s [124, 125]. Furthermore, ferrimagnetic insulators such as RIGs have gained a lot of interest due to the realization of achieving a high quality thin films with perpendicular magnetization using a variety of fabrication techniques [158–161]. Such latter property of RIGs has led to the experimental observation of efficient current-induced control of magnetization, [162–164] current-driven domain wall motion [165], and high temperature quantum anomalous Hall effect in ferri-

magnetic insulator/topological insulator heterostructures [166]. Unlike the commonly used ferromagnetic conductors, ferrimagnetic insulators have a smaller heat dissipation as well as writing current.

Thus, the objective of the studies in this chapter, is to study whether epitaxial strain can influence the magnetization compensation temperature (and Curie temperature, T_C, too, if possible) in rare-earth iron garnets films. Moreover, we wish to look and unveil the origins of such hypothetical tunings, including what kind of magnetic moments (among those of the rare-earth ions and two types of Fe ions) are mostly responsible for them.

Here, we will focus on how epitaxial (001) strain can affect the structural and magnetic properties, including T_M and T_C, of GIG films. In order to do that we employ the presently-developed effective Hamiltonian (see details in the Methods section of this chapter), with all its coefficients being extracted from first-principles calculations. With that, we will reveal and explain why misfit strain can indeed drastically and intrinsically affect T_M and T_C in RIG systems.

5.2 Methods

First, we chose Gadolinium as a rare-earth in our RIG system and studied both bulk and epitaxial (001) films made of Gadolinium Iron Garnet (GIG) as a function of temperature and misfit strain. GIG has been chosen due to having the highest T_M among all RIGs at 286K [8] which is already close to room temperature, thus being the most applicable RIG to have room temperature T_M. Here, an epitaxial strain ranging from -3% (compressive strain) to +3% (tensile strain) was considered for (001) GIG films, which is realistic [120]. Technically, we use periodic boundary conditions along any direction, including the out-of-plane one. Consequently, we model the sole effect of epitaxial strain on magnetic properties of (001) GIG films (which can help to better understand epitaxial films [167–169]), thus results of this study should be applicable to RIG films that are neither not too thin (to avoid surface effect) nor too thick (that is, the thickness should be below the critical thickness

above which structural relaxation of the in-plane lattice vectors begins to occur). Note that such latter critical thickness has been reported to be a couple of nanometers in some RIG films [120, 170].

As detailed in Chapter 2.3, we use an effective magnetic Hamiltonian to describe the magnetic interactions in GIG films. However, in this study, we do not consider spin-orbit coupling and only consider up-to 2nd order interactions. Such assumptions are taken due to the fact that, as we will see below, collinear magnetism can already well reproduce Curie and compensation temperatures in GIG system. Thus, the effective magnetic Hamiltonian considered here is as follows

$$H = H_1^{ex} + H_2^{ex} \tag{5.1}$$

with

$$H_1^{ex} = \frac{1}{2} \sum_{<i,j>_1} J_{1,ij} \hat{S}_i \cdot \hat{S}_j$$

$$H_2^{ex} = \frac{1}{2} \sum_{<i,j>_2} J_{2,ij} \hat{S}_i \cdot \hat{S}_j$$

where H_1^{ex} and H_2^{ex} denote the first and second nearest neighbor exchange couplings between different types of ions. Such interactions will be described in Table (5.2) later on. $S = \frac{5}{2}$ and $S = \frac{7}{2}$ are used for Fe and Gd ions, respectively. The J parameters, which characterize the magnetic exchange couplings, are extracted by performing DFT calculations which is detailed below. Once all the magnetic parameters are found for the GIG bulk and thin films, Eq. (5.1) is then employed in Parallel Tempering Monte Carlo (MC) simulations on $4 \times 4 \times 4$ supercells (each unit cell contains 160 atoms, which implies that our supercell has 10,260 ions, including 4096 magnetic ones) using the heat bath algorithm [171], in order to predict magnetic properties such as the compensation and Curie temperatures. Technically, 2,000 exchange steps are performed in each MC simulation with each exchange step containing 200 sweeps [171].

The DFT calculation setup is similar to the study done in Chapter 4 since the system is

the same. All calculations are carried out via VASP [130] using the projector augmented-wave potentials [131]. The following electrons are treated as valence states for each ion: O 2s and 2p, Fe 3d and 4s, and Gd 5p, 5d and 6s. The generalized gradient approximation (GGA), together with the revised Perdew-Burke-Ernzerhof exchange-correlation functional for solids (PBEsol) [132] is employed with an effective Hubbard U parameter of 4eV for the localized 3d electrons of Fe ions and U = 4eV for the localized 4f electrons of Gd ions. Since the lowest energy collinear spin configuration has tetrahedral Fe ions, Fe^{tet} , arranged antiferromagnetically with respect to the other two sublattices (octahedral Fe, Fe^{oct}, and Gd ions) in bulk GIG [119], we adopt such magnetic configuration for bulk and epitaxial films. For any chosen epitaxial strain for the (001) films, the in-plane lattice vectors are frozen in our calculations with their length being related to the misfit strain. All the other structural degrees of freedom of these films, that are the out-of-plane lattice vector and atomic positions, are allowed to relax. In contrast, all structural degrees of freedom are allowed to relax in the bulk case. Furthermore, the energy cutoff of 500 eV is used, and Monkhorst-Pack k-point mesh is chosen to be $2 \times 2 \times 2$ for the 160-atom cubic unit cell. As mentioned previously, spin-orbit couplings and noncollinear magnetism are not considered in our calculations. Additionally, we numerically checked the effect of single ion anisotropy of all three magnetic sites on properties. We did not find any change in T_M and T_C when single ion anisotropies were included. Structural relaxations are performed until the Hellmann-Feynman force on each atom is less than 5 meV/$\mathring{A}$. The crystal space group of GIG bulk is identified to be $Ia\bar{3}d$ using FINDSYM [79] in our calculations, as consistent with experiments [8]. In contrast, the space group of the GIG films is $I41/acd$, as a result of the considered epitaxy. Our DFT calculations predict that the cubic centrosymmetric structure of GIG bulk has lattice parameters $a = b = c = 12.405\mathring{A}$, which are in 0.5% error range of the experimental value of $12.471\mathring{A}$ [172], and the internal atomic positions that are shown in Table (5.1). For comparison, Table (5.1) further shows such internal atomic positions but for a film experiencing a -1% compressive strain. The Wyckoff positions of Fe^{tet} and Gd ions

in bulk GIG are splitting into different positions under the influence of strain (such splitting gives rise to more distinct magnetic interactions in the films than in the bulk, as shown in Table (5.2).

Table 5.1: Atomic positions in the unit cell of the bulk GIG and (001) GIG films under a -1% compressive strain.

		Wyckoff position	x	y	z
Bulk case	O	96h	0.972	0.056	0.150
	Fe^{oct}	16a	0.000	0.000	0.000
	Fe^{tet}	24d	0.375	0.000	0.250
	Gd	24c	0.125	0.000	0.250
Film under a compressive strain of -1%	O	32g	0.972	0.056	0.149
		32g	0.149	0.972	0.057
		32g	0.557	0.650	0.472
	Fe^{oct}	16c	0.000	0.000	0.000
	Fe^{tet}	16e	0.375	0.000	0.250
		8a	0.000	0.250	0.375
	Gd	16e	0.125	0.000	0.250
		8b	0.000	0.250	0.125

The exchange coupling coefficients, J, of Eq. (5.1) are extracted from our DFT calculations for the bulk and any studied strain (-3% to +3%), using the four-state energy mapping method. Overall, there are 10 different couplings in the bulk structure, including first-nearest neighbor (1NN) and second-nearest neighbor magnetic couplings (2NN), within a bond length of 5.6Å. Four of them were numerically found (when running MC simulations) to have a minimal or no influence on magnetic behavior. Thus, we considered only the following six couplings in all our MC calculations that show noticeable influence on overall magnetic property: 1NN tetrahedral Fe (Fe^{tet}) – octahedral Fe (Fe^{oct}), 1NN $Fe^{tet} - Gd$, 1NN $Fe^{tet} - Fe^{tet}$, 1NN $Fe^{oct} - Gd$, 1NN $Fe^{oct} - Fe^{oct}$ and 2NN $Fe^{tet} - Gd$. These six interactions are listed in Table (5.2) in the bulk case, starting with the coupling that has the strongest coupling strength. It is also important to know that the listed first-nearest neighbor J parameter between tetrahedral Fe and Gd ions has been enhanced by a factor of 1.95 with respect to its DFT-extracted parameter, in order to reproduce the experimen-

Table 5.2: Calculated (renormalized) exchange coupling coefficients J for the bulk GIG and (001) GIG films under a -1% compressive strain.

	Without strain	-1%	1%
Coupling	J (meV)	J (meV)	
1NN $Fe^{oct} - Fe^{tet}$	7.456000	7.852000	7.244000
		7.836000	7.100000
		7.716000	7.060000
1NN $Fe^{tet} - Gd$	0.807857	0.958286	0.835714
		0.924857	0.702000
		0.774429	0.663000
1NN $Fe^{tet} - Fe^{tet}$	0.332000	0.368000	0.316000
		0.352000	0.304000
1NN $Fe^{oct} - Gd$	-0.105714	-0.102857	-0.108571
		-0.102857	-0.105714
		-0.117143	-0.094286
1NN $Fe^{oct} - Fe^{oct}$	0.096000	0.096000	0.092000
		0.096000	0.092000
2NN $Fe^{tet} - Gd$	-0.062857	-0.057143	-0.062857
		-0.054286	-0.062857
		-0.062857	-0.068571

tal result of T_M of Ref. [8] for the bulk system. Note that we numerically found out that only considering this renormalized 1NN J coefficient between tetrahedral Fe and Gd ions in our MC calculations yields an underestimatation of T_M by about 35K but also makes the agreement with experiments for the total magnetization-versus-temperature curve worst, in the bulk case. Such enhancement of this J parameter is also systematically used in our MC calculations for epitaxial (001) thin films. Furthermore, studied GIG films becomes tetragonal under epitaxial strain with the $I41/acd$ space group, the aforementioned six different magnetic couplings of the bulk case now become 16 different couplings with different energies. As an example, Table (5.2) further shows these 16 different couplings for the GIG films being under a compressive strain of -1% and a tensile strain of +1%. These J coefficients all increase when going from tensile to compressive strains, except for the one involving a 1NN $Fe^{oct} - Gd$ interaction. Such increasing tendency will be discussed in the context of altering T_M and T_C later on.

5.3 Results

5.3.1 The Bulk properties

MC calculation results for the GIG bulk is reported here. Figure (5.1) and its inset display the total magnetic moment and the specific heat, respectively, as a function of temperature. Figure (5.1) shows that the predicted T_M for the bulk structure is around 286K, which is precisely the fits experimental value of Ref. [8]. Moreover, a clear peak around 560K in the specific heat can be seen, which is indicative of the magnetic phase transition from paramagnetic to ferromagnetic. Such theoretical value of T_C is in very good agreement with the experimental result of 556K [42]. The predicted magnetic moments also remarkably agree with the experiments of Ref. [8] for any measured temperature below 300K, as shown in Fig. (5.1a). Such agreements testify the accuracy of our calculations, once the aforementioned renormalization of a single exchange coupling parameter is accomplished and verifies our assumption of not considering spin-orbit coupling in our calculations. Moreover, Fig. (5.1b) reports the magnetic moment of each individual type of magnetic ion (Fe^{tet}, Fe^{oct}, Gd) as a function of temperature. Below the magnetic phase transition at around 560K, spins of the Fe ions become ordered, with the overall magnetization becoming negative as a result of (i) spins of Fe^{tet} ions being antiferromagnetically aligned with respect to spins of the Fe^{oct} ions (as consistent with the strong and positive value of the J parameter of the 1NN $Fe^{tet} - Fe^{oct}$ interaction listed in Table (5.2) and equal to 7.456 meV) and (ii) Fe^{tet} and Fe^{oct} ions having a 3:2 ratio in the formula unit. Furthermore, as we reach lower temperatures, the spins of the Gd ions start to become ordered (due to having different temperature dependence with respect to the Fe ions) and are antiparallel to those of Fe^{tet} ions, which is in-line with the positive J parameter of 0.808 meV indicated in Table (5.2) for the 1NN Fe^{tet}–Gd interaction. Eventually, the magnetic moment of Gd ions rises as temperature decreases, to a value that completely cancels out the overall magnetic moment deriving from the Fe sublattice, which is the magnetization compensation temperature. Below such T_M, the total magnetic moment

becomes positive (reversal from the negative value above T_M), mostly due to the strong temperature dependency of the Gd magnetic moments. Note also that our Fig. (5.1a) is qualitatively consistent with the temperature behavior of the individual magnetic moments reported for the bulk case in the Supplemental Material of Ref. [118]. On the other hand, our quantitative predictions for the T_M and T_C, as well as for the temperature evolution of the total magnetic moment, better agree with experimental results than the results reported in Ref. [118].

Next, in order to address the residual magnetization above T_C that one can see in the Figs. (5.1a) and (5.1b), we study different supercell sizes in the MC simulations. Such residual magnetization was found to be related to the supercell size and to demonstrate such fact, Fig. (5.1c) shows the total magnetic moment of bulk GIG as a function of temperature for different supercell sizes: $4 \times 4 \times 4$, $6 \times 6 \times 6$ and $8 \times 8 \times 8$. One can clearly see that there is basically no change in the magnetic moment below T_C, as the supercell size changes while the residual magnetization above T_C decreasing in magnitude as the supercell size increases. Hence, in order to save computational cost in our study, all MC calculations ran on a 4x4x4 supercell. Furthermore, if we analyze the J parameters in Table (5.2), the first two couplings (1NN Fe^{tet}–Fe^{oct} and 1NN Fe^{tet}–Gd) have much stronger couplings than the other J parameters, thus one could wonder whether the other magnetic couplings have negligible effect on the total magnetic moment of the system. Thus, to check this hypothesis, we show in Fig. (5.1d) the total magnetic moment of bulk GIG as a function of temperature when only the two strongest magnetic couplings (mentioned above) are included and when all six interactions are included. Note that, here, the modification factor of the coupling, 1NN $Fe^{tet} - Gd$, is increased from 1.95 to 2.21, in order to match the experimental T_M [8]. Results shown in Fig (5.1d) reveal that the magnetic behavior below T_M is almost identical between these two cases, but then starts to change above T_M thus leading to a different T_C value. As a matter of fact, and as evidenced in the inset of Fig. (5.1d), T_C increases by about 50-60K, when only two magnetic couplings are considered, with respect to the T_C where all

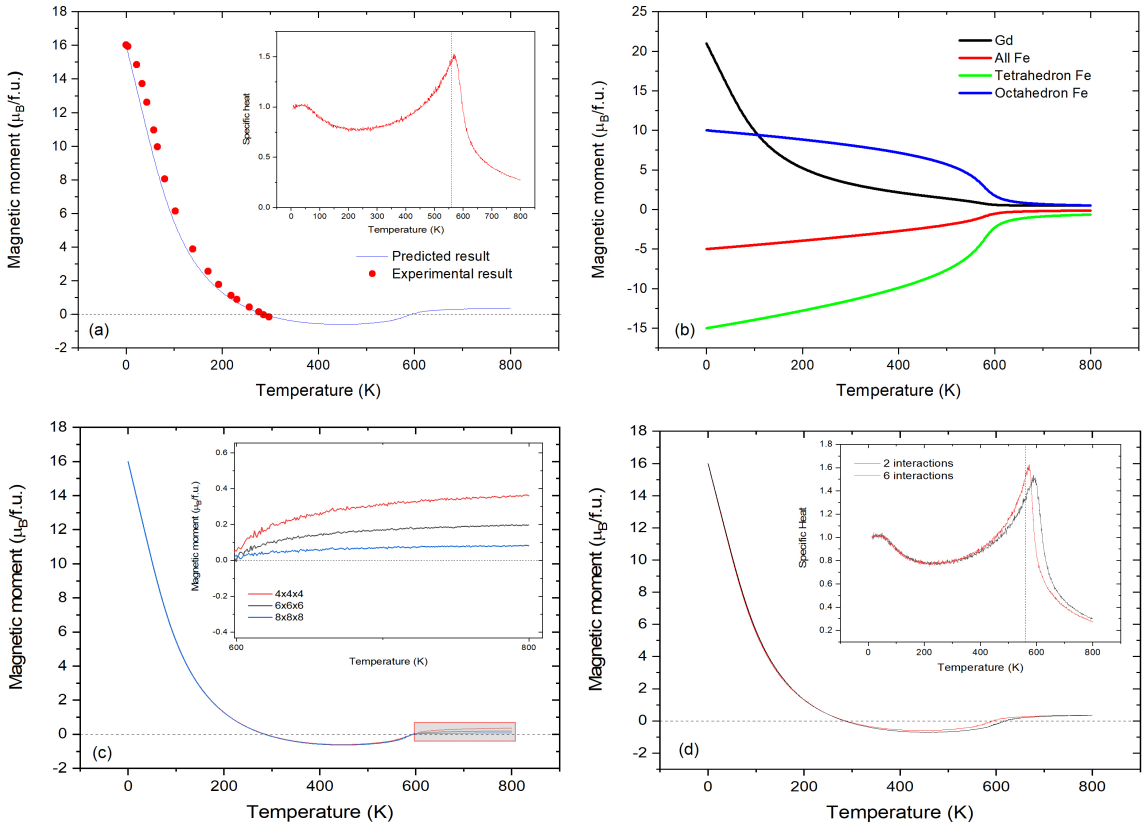

Figure 5.1: Predicted total magnetic moment (Panel a) and individual magnetic moments (Panel b), as a function of temperature in GIG bulk. The data points in Panel (a) show the measurements of Ref. [8]. The inset of Panel (a) displays the temperature dependence of the specific heat (in arb. units). In this inset, the vertical line represents the experimental value of the Curie temperature [9]. (Panel c) Predicted total magnetic moment as a function of temperature in GIG bulk for different supercells. The inset zooms in the gray area above the Curie temperature. (Panel d) The predicted total magnetic moment as a function of temperature in GIG bulk, for which two (red color) and six (black color) magnetic interactions are considered in the calculations. The inset displays the temperature dependence of the specific heat (in arb. units) and the vertical dashed line represents the experimental value of the Curie temperature [9].

six couplings are included. The vertical dashed line in the inset reports the experimental result of Ref. [9] for T_C and therefore affirms that one needs to consider all six magnetic couplings in order to have a better agreement with experimental findings/observations.

5.3.2 The film properties

Now that we know that our model and computed magnetic properties are in good agreement with the experimental results, let us look at the epitaxial (001) GIG thin films. As results show in Fig. (5.2), (001) GIG thin films under epitaxial strain (both compressive and tensile) have both T_M and T_C significantly changing. For example, a compressive strain of -3% enhances T_M from 286K to 400K and T_C from 560K to 680K with respect to the bulk case, while a tensile strain of +3% reduces T_M down to 193K and T_C down to 500K with respect to the bulk values. Indeed, T_M and T_C are found to change almost linearly with respect to epitaxial strain as shown in Fig. (5.3). Especially, one objective of this study is to check whether T_M can be varied around room temperature and it is predicted here that it can be done in the strain window ranging between -1% and +1%, which is precisely the range that includes the misfit strains that should be experienced by GIG on available substrates such Gadolinium Gallium Garnet (GGG), Terbium Gallium Garnet (TGG), and Neodymium Gallium Garnet (NGG) [120]. Such possibility to have T_M around room temperature should be highly beneficial for technologies such as the idea of realization of possible reversal of magnetization by light around the magnetization compensation temperature [8]. Furthermore, misfit strain can also effect strongly on the T_C of GIG and it can also be of importance for, e.g., larger magnitude of the magnetization at room temperature (see insets of Figs. (5.2a) and (5.2c) for compressive and tensile strains of -3% and +3%). Note also that the enhancement of T_M by applying compressive strain is reminiscent of the strengthening of the compensation temperature found in RIG systems but when applying a hydrostatic pressure [125]. However, this comparison has to be taken with a grain of salt since applying hydrostatic pressure is not similar to the application of an epitaxial strain. This is because all three lattice parameters

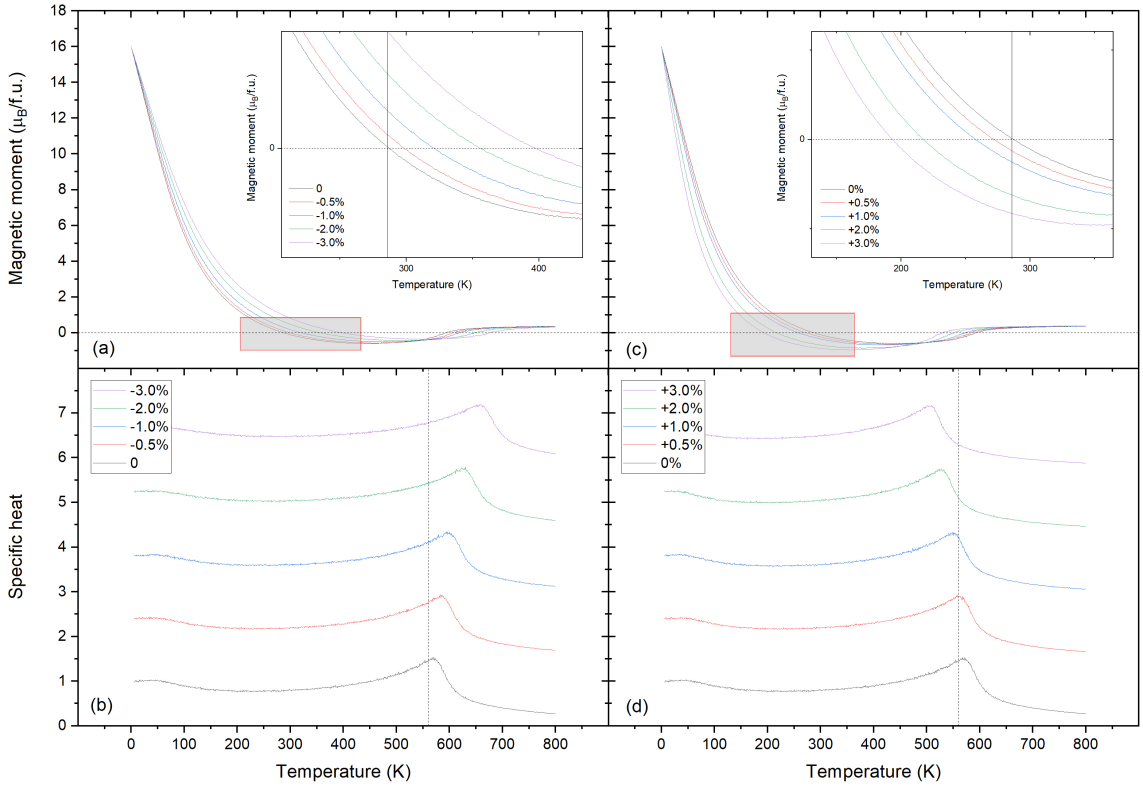

Figure 5.2: Predicted magnetic properties of epitaxial (001) GIG films under epitaxial strains. (Top panels) Total magnetization as a function of temperature with the inset showing the magnified data of the gray box area and the vertical lines represents the experimental value of T_M [8] of GIG bulk. (Bottom panels) Specific heat as a function of temperature for the studies epitaxial strain range. Vertical dashed lines in these bottom panel figures represent the experimental value of the Curie temperature of GIG bulk [9].

typically decrease under increasing hydrostatic pressure while enhancing the magnitude of epitaxial compressive strain usually results in significantly increasing the out-of-plane lattice parameter.

Our results reveal that one can indeed tune T_C and T_M with epitaxial strain in GIG and now, let us look at the microscopic reason behind these changes and try to understand the driving force behind the strain-induced changes. In order to do that, we report (i) in Figs. (5.4a), (5.4b), and (5.4c), the change in the magnitude of the individual magnetic moments of Fe^{oct}, Fe^{tet}, and Gd ions as function of temperature, respectively, for different strains and (ii)

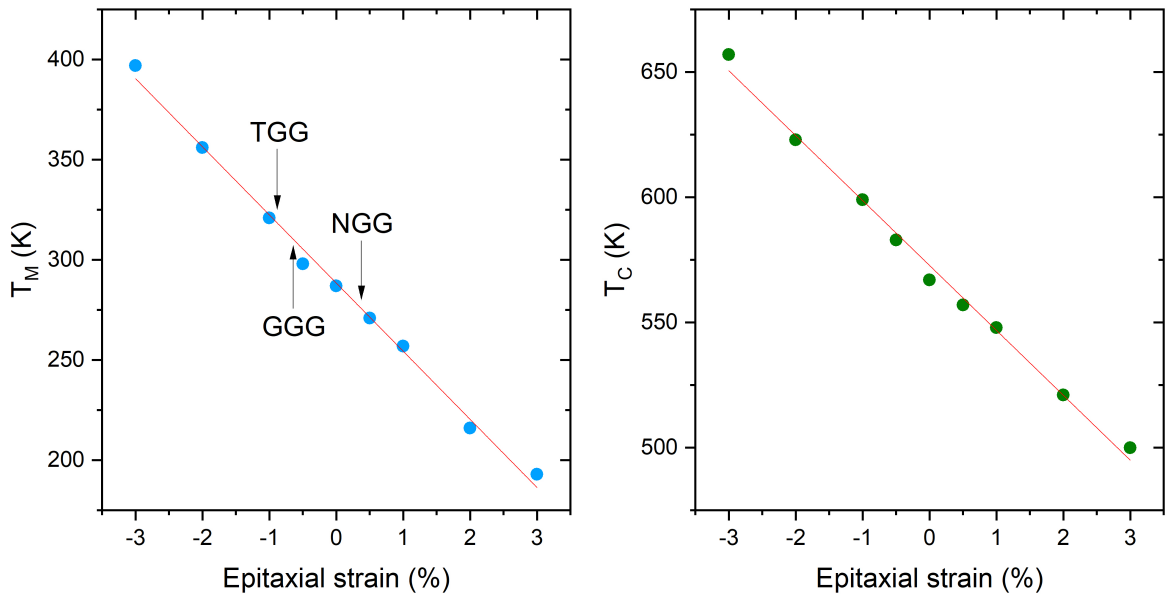

Figure 5.3: Dependence of T_M (Panel a) and TC (Panel b) as functions of the studied epitaxial strain. Misfit strains associated with possible substrates to achieve the tuning of T_M and T_C are shown in Panel (a) by means of arrows: Gadolinium Gallium Garnet (GGG), Terbium Gallium Garnet (TGG) and Neodymium Gallium Garnet (NGG). The red solid lines in both panels represent linear fits of the MC data.

in Fig. (5.4d) the dependence of six (averaged) exchange coupling J parameters on epitaxial strain. Figures (5.4a-c) show that all different magnetic moments are affected by the misfit strain at any temperature but not at same rate. For example, at higher temperatures (i.e., above about 400K), the magnetic moments of Fe^{oct} and Fe^{tet} ions are the ones changing a lot under epitaxial strain while those of the Gd ions are rather small, therefore leading to the aforementioned increase in T_C when going from tensile to compressive strain. Such results of change in a magnetic moments of the two types of Fe ions and concomitant change in T_C can mostly originate from the large enhancement in the first-nearest neighbor J coupling (the strongest coupling in the system) between Fe^{oct} and Fe^{tet} ions when going from +3% to -3%, as evidenced in Fig. (5.4d) and as is also consistent with Table 5.2. On the other hand, at lower temperatures (i.e., below about 300K) and under epitaxial strain, the magnetic moment of Gd is changing significantly with respect to the magnetic moments of the two types of Fe ions, as shown in Figs (5.4a-c). Such difference in temperature dependence

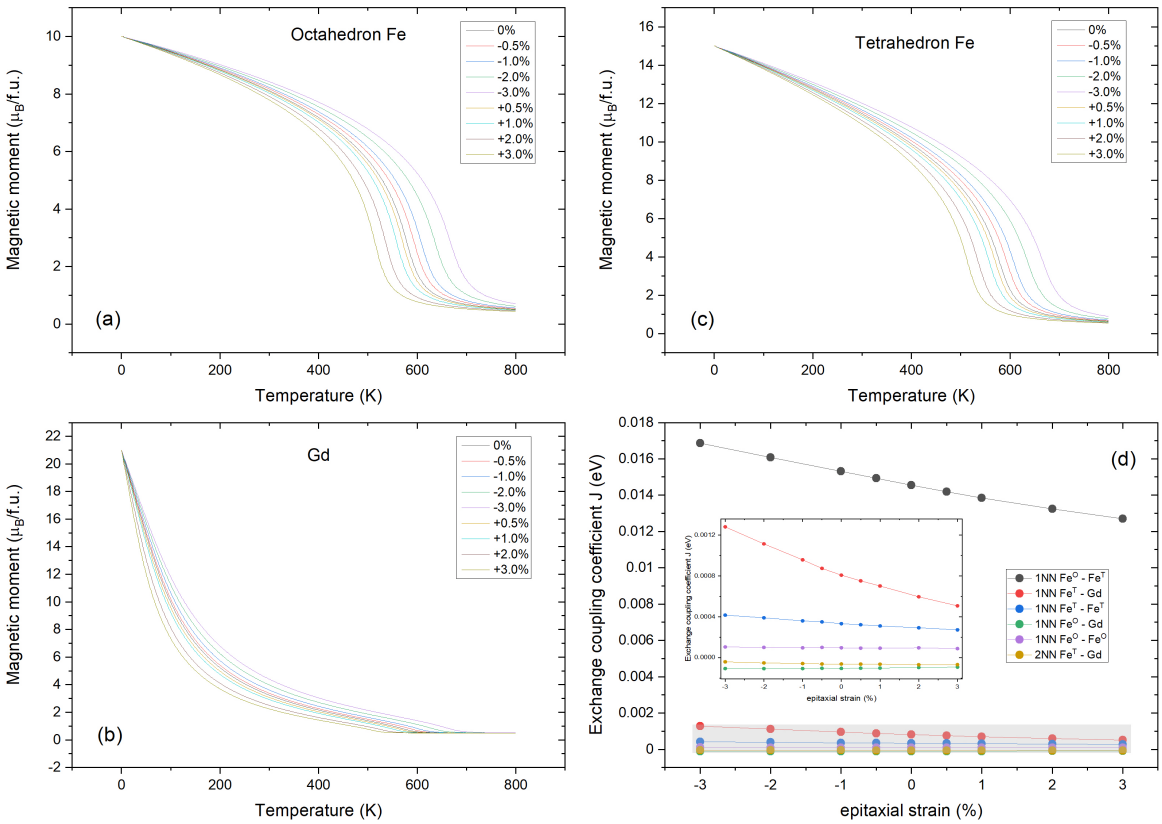

Figure 5.4: Contributions from different magnetic sites to the total magnetization of the system as a function of temperature, for different epitaxial strains (Panels a-c); and dependence of exchange coupling coefficients on epitaxial strain (Panel d). In Panel (d), each exchange coupling parameters are averaged over similar individual parameters. For instance, three different values are averaged for the 1NN Fe^{oct}–Fe^{tet} interaction, as consistent with Table (5.2).

between the Gd and Fe ions results in the increase of T_M when varying strain from positive to negative values (tensile to compressive). Such finding can be traced back to the fact that the magnetic moment of Gd ions is antiferromagnetically coupled with that of the tetrahedral Fe ions, and such specific magnetic interactions has exchange parameters that strengthen when going from +3% to -3% of strain, as revealed by Fig. (5.4d) and Table (5.2). Thus, one can understand such effect by realizing that compressive strain reduces the in-plane distance between the ions, resulting in an enhancement in the exchange interactions (as evidenced by the increase in the J coefficients) that leads to the enhancement in T_M and T_C.

5.4 Summary

Here, we studied the effect of epitaxial strain on the magnetization compensation temperature and Curie temperature of the (001) Gadolinium Iron Garnet films via *ab-initio*-based MC simulations. The changes in the magnetization compensation and Curie temperatures were found to be substantial and linear with respect to the epitaxial strain. Compressive strain is found to enhance these two critical temperatures while the tensile strain decreases them both. We also reveal the microscopic reasons behind these changes and our finding suggest that such strain effects should occur in all Rare-earth Iron Garnet systems. One can even envision to create a magnetization compensation temperature in some RIG systems that do not have it in their bulk form. In fact, such attempt was done in some preliminary experiments on epitaxial Thulium Iron Garnet film [173]. Tuning T_M and T_C should bring substantial advantage for spintronic applications, especially if one succeeds to bring the magnetization compensation temperature close to 300K, as predicted here when growing (001) GIG films on the GGG substrate. It is also very likely that another critical temperature, namely the so-called angular momentum compensation temperature (which can be strongly dependent on the magnetization compensation temperature [174]), can be modified to, e.g., reach room temperature when varying the epitaxial strain in RIG films. In such a case, magnetic-field-controlled antiferromagnetic spin dynamics [175] will occur around

300K, along with an optimization of the speed of the domain walls [33, 176]. Thus, we hope that our findings can be of large benefits to the magnetic community, especially since high-quality RIG films can be nowadays grown [116, 160].

6 Magnetization compensation temperature and topological phases in Mn_4N

6.1 Introduction

In this last section of results of the dissertation, we look at a ferrimagnet that has gained a lot of attention lately thanks to its properties such as perpendicular magnetic anisotropy (PMA) and ultrafast response to external field [177–185]. Such ferrimagnet is Mn_4N that has an antiperovskite structure, which is the same as the perovskite structure but with cations and anions having inverted positions. For example, the one of more known perovskites, $BiFeO_3$, has three times more numerous O ions than the Ba or Fe cations, while in the Sr_3SnO antiperovskite [186], it is reverse with Sr cations being thrice more than O anions (or Sn cations). In antiperovskite ferrimagnet Mn_4N, because Mn cations are at different sites and have unequal magnetic moments, it can be viewed as having the Mn_3MnN stoichiometry with Mn ions on different sites. In general, antiperovskites are found to display a promising properties such as superconductivity [187] and topological band gaps [188–190].

As mentioned in previous chapters, ferrimagnets can have a promising feature called the magnetization compensation temperature which can give rise to the antiferromagnetic-like dynamics in ferrimagnets and lead to high-speed domain walls motion [33, 175]. Plus, ferrimagnets with small M_S and PMA allow them to host ultrasmall and fast skyrmions at room temperature [33, 191, 192] that could lead to a promising achievement of realizing a high-density, low-cost, and energy-efficient skyrmionic device technology.

Despite its recent gain of interest, Mn_4N (or any other antiperovskite ferrimagnet) have not been reported (to be best of our knowledge) to possess a magnetization compensation temperature or any magnetic topological defects. Finding such properties in Mn_4N would potentially lead to a new door for designing spintronic devices and revealing the driving mechanism behind them is of high importance for future technology and fundamental science. Thus, it is timely to wonder if antiperovskite ferrimagnet Mn4N has such properties and what

are the driving mechanism behind them. Does the driving mechanism differ from the dipole-dipole interactions [193] or Dzyaloshinskii-Moriya interactions [194]? If yes, finding such a mechanism will deepen/broaden the understanding of topologies and magnetism.

Hence, in this chapter, we answer all these open questions by performing first-principles calculations and *ab-initio* based Monte Carlo simulations. The main results of our findings are as follows: (i) existence of a sizeable magnetization compensation temperature that is driven by the different temperature behavior of three types of magnetic Mn ions; and (ii) metastable topological states such as nanometric hedgehog-anti-hedgehog pairs (HAPs) that are induced by frustrated exchange interactions in the system.

6.2 Structure

A neutron diffraction experiment [185] revealed two types of magnetic configurations in Mn_4N. The one shown in Fig. (6.1a) and used for this study is denoted as the Type-B structure. In Type-B structured Mn_4N, the spins of Mn I and Mn II are aligned parallel to each other while being antiparallel to the spins of Mn III (A,B). On the other hand, so-called Type-A structure exhibits spins of Mn II and Mn III to be aligned parallel to each other but antiparallel to those of Mn I. Our first-principles calculations results (at 0K) predict that the Type-B structure has lower energy than Type-A structure which is consistent with previous studies of Refs. [118, 178]. Thus the Type-B structure has been chosen in this study.

6.3 Methods

All first-principles calculations are carried out within the framework of DFT as implemented in VASP [130] using the projector augmented-wave potentials [131]. The generalized gradient approximation (GGA), altogether with the Perdew-Burke-Ernzerhof exchange-correlation functional [49, 57], is employed with an effective Hubbard U parameter of 0.54 eV for the localized 3d electrons of Mn ions. Such Hubbard U value was chosen in order to have the in-plane lattice constant, a_{ip}, and the c/a axial ratio close to the experimental values of a_{ip}

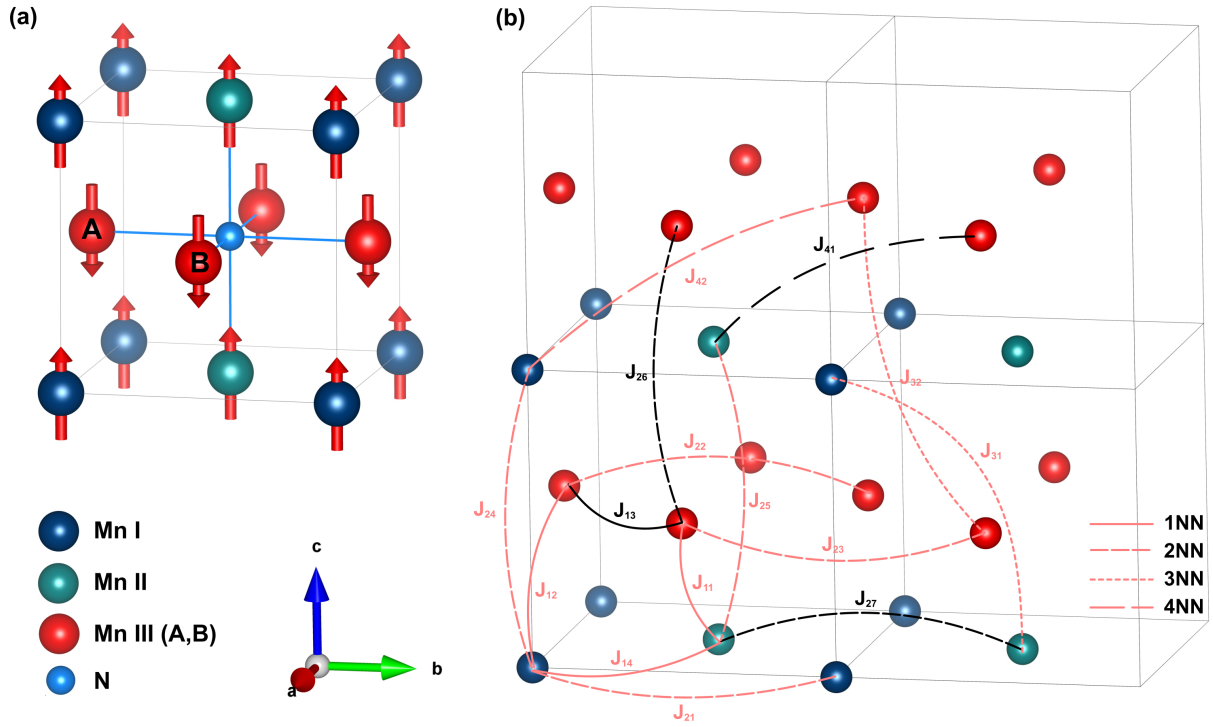

Figure 6.1: Panel (a) illustrates the schematic of atomic arrangements and Type-B magnetic arrangement in the Mn_4N unit cell. The spins of the Mn III atoms are arranged antiparallel to the spins of the Mn I and Mn II atoms. Panel (b) shows the $2 \times 1 \times 2$ supercell of Mn_4N where it displays all the different J parameters that are considered in this study. The frustrated exchange J parameters are colored in black

= 3.89Å and c/a ≈0.99 for the Type-B structure described previously, respectively [185]. Our choice of U gives a_{ip} and c/a ratio to be 3.897Å and 0.98, respectively. The energy cutoff is selected to be 800 eV and the Monkhorst-Pack k-point mesh is taken to be 13×13. Structural relaxations are performed until the Hellmann-Feynman force on each atom is less than 0.001 eV/Å. All calculations include spin-orbit coupling and provide the following magnetic moments in each unit cell at 0K for the Type-B structure: 3.6 μ_B for Mn I, 1.16 μ_B for Mn II, and -3.01 μ_B for both Mn III ions (i.e., A and B), respectively. The four-state energy mapping method [60, 195] is used to obtain the magnetic exchange coupling parameters (J) and single ion anisotropy (SIA) coefficients in 3x3 matrix forms. A $3 \times 3 \times 3$ supercell with $4 \times 4 \times 4$ k-point mesh and high energy cut (800eV) were used to accurately extract the J parameters between the magnetic sites. Note that all our calculations include spin-orbit coupling.

Here, we utilized the magnetic effective Hamiltonian (Eqs. (2.14)) described in Chapter (2.3) with its parameters extracted from the first-principles calculations. Spins (S) are set to be 1 and their values are absorbed by the magnetic exchange coupling (J) parameters. Parallel tempering Monte Carlo (MC) simulations [171] are performed using the magnetic effective Hamiltonian of Eqs. (2.14). A $12 \times 12 \times 12$ supercell is used and, at each temperature, 160,000 MC sweeps are performed. After collecting statistical properties from MC simulations, a conjugate gradient (CG) method [196] is applied to further optimize the spin configurations and to guarantee that all the predicted phases locate at their energy minimum.

6.4 Results

All the magnetic parameters extracted from the DFT results are reported in Tables (6.1 and 6.2) and the schematics of considered magnetic exchange interactions are shown in Fig. (6.1b). Since the system is metallic with long-range interactions, we carefully checked all the magnetic exchange interactions up to the 6^{th} nearest-neighbor (6NN) interactions. Our results show that an accurate prediction of the magnetic properties of Mn_4N system can be

done by just including interactions up to the 4^{th} nearest-neighbors (4NN), which corresponds to a distance of 4.755Å (note that a_{ip} is 3.89Å). To be precise, as shown in Table (6.1), J_{51}, J_{52}, J_{53}, J_{61}, and J_{63} are found to have positive E (the energy contribution of each 5NN and 6NN J coupling parameter of the total energy of the ferrimagnetic ground state with respect to the paramagnetic state), which thus leads to raising the total energy of the ferrimagnetic ground state with respect to the paramagnetic structure. Moreover, after excluding 5NN and 6NN J parameters in the MC simulations, we found that the Curie (T_C) and the magnetization compensation (T_M) temperatures do not exhibit any significant change. Also, we found that the topological phases, which we will discuss later on, remain stable even without 5NN and 6NN J parameters being included in the MC simulations. Thus, here on, we only consider the magnetic exchange parameters up to 4NN in our study.

Now let us focus on Table (6.1). One can see that most of first nearest-neighbor (1NN) J couplings adopt positive values which is consistent with the ferrimagnetic arrangement in Type-B structure. To be explicit, J_{11} - 1NN interaction between Mn II and Mn III(B) ions are positive and thus favor an antiparallel arrangement between them, as consistent with the ferrimagnetic Type-B structure. Similarly, the J_{12} - 1NN interaction between Mn I and Mn III(A) ions adopt positive values too, which are in-line with the antiparallel alignment between these Mn ion spins within Type-B structure. The J_{14} - 1NN interaction between MnI and MnII ions are negative and adopt a parallel alignment, which once again favors Type-B magnetic arrangement. On the other hand, the J_{13} - 1NN interaction between Mn III(A) and Mn III(B) ions are positive and thus leads to their tendency to prefer a antiparallel arrangement to each other. This tendency of J_{13} couplings contradict with the ferrimagnetic arrangement of such spins within Type-B structure, which explains why it induces a positive (unfavorable) change in energy with respect to the paramagnetic structure (positive E value in Table (6.1)). Note that a exchange coupling parameters such as J_{13} that leads to an increase in the total energy of the system with Type-B structure (with respect to the paramagnetic state), will be called frustrated exchange parameters [197] in here. We

Table 6.1: Calculated magnetic exchange coupling parameters of Mn_4N up till 6^{th} nearest-neighbor Mn-Mn pairs. E is the energy contribution of each J parameters in the total energy of the ferrimagnetic ground state with respect to the paramagnetic state per unit cell. (unit: meV)

Couplings	J_{xx}	J_{yy}	J_{zz}	E
J_{11}	68.410	68.490	68.380	-136.759
J_{12}	58.500	58.200	59.000	-117.999
J_{13}	18.800	18.800	17.600	17.600
J_{14}	-72.510	-72.510	-73.050	-73.049
J_{21}	-90.100	-90.200	-90.200	-45.100
J_{22}	-50.400	-50.400	-50.400	-25.200
J_{23}	-42.800	-42.600	-43.076	-45.100
J_{24}	-34.000	-34.000	-35.000	-8.750
J_{25}	-1.340	-1.340	-2.300	-0.575
J_{26}	5.800	5.600	5.800	2.900
J_{27}	9.010	8.970	8.480	4.240
J_{31}	-1.800	-1.800	-1.800	-25.200
J_{32}	-0.400	-0.400	-0.400	-0.800
J_{41}	-5.300	-5.300	-5.300	21.200
J_{42}	4.600	4.600	4.600	-18.400
J_{51}	5.525	5.525	5.520	5.525
J_{52}	0.547	0.547	0.542	0.547
J_{53}	4.650	4.650	4.650	4.650
J_{54}	-5.486	-5.486	-5.482	-5.486
J_{61}	4.000	4.000	4.000	2.000
J_{62}	0.922	0.922	0.900	-3.125
J_{63}	-3.125	-3.125	-3.120	0.461

found that the parallel alignment between Mn III(A) and Mn III(B) ions within Type-B, despite favoring antiparallel alignment according to J_{13}, mainly originates from the strong positive J_{11} and J_{12} through indirect interactions.

Moreover, let us examine second-nearest-neighbor (2NN) exchange coupling parameters in Table (6.1). They are between in-plane Mn I - Mn I pairs (J_{21}), in-plane Mn III(A) - Mn III(A) pairs (J_{22}), in-plane Mn III(B) - Mn III(B) pairs (J_{23}), out-of-plane Mn I - Mn I pairs (J_{24}), and out-of-plane Mn II - Mn II pairs (J_{25}), which are all negative and thus favor ferromagnetic (FM) interactions between these 2NN pairs, as consistent with Type-B (see

Table 6.2: Calculated DM interactions of the first nearest-neighbor Mn-Mn pairs and SIA parameters of Mn_4N (unit: meV).

	D_x	D_y	D_z
D_{11}	0.050	-0.185	0.005
D_{12}	0.000	-1.050	0.050
D_{13}	-0.050	-0.050	-3.900
D_{14}	0.050	-0.055	0.000
	Axx	Ayy	
Mn I	0.020	0.000	
Mn II	-2.620	-2.640	
Mn III	-0.620	-0.020	

Fig. (6.1b) for the sketch of such couplings). On the other hand, as found in 1NN couplings, we also found frustrated exchange parameters. They are Js between out-of-plane Mn III(B) - Mn III(B) pairs (J_{26}) and in-plane Mn (II) - Mn (II) pair (J_{27}) that adopt positive values leading to an raise in total energy with respect to the paramagnetic state, thus J_{26} and J_{27} are frustrated exchange parameters too. Note that the strongest-in-magnitude magnetic exchange coupling interaction in the Mn_4N system is found to be the 2NN interaction between in-plane Mn I - Mn I pairs, namely the J_{21} term that has a value of -90.1 meV. Furthermore, as shown in Table (6.1), the 3rd nearest neighbor (3NN) and the 4th nearest neighbor (4NN) magnetic exchange coupling parameters are weaker (in magnitude) than the J parameters of 1NN and 2NN. In details, 3NN magnetic exchange coupling parameters between Mn II - Mn I pairs (J_{31}) and Mn III(A) - Mn III(B) pairs (J_{32}) adopt negative values (favoring FM interaction) and the 4NN J parameter between Mn I - Mn III(A) pairs (J_{42}) adopt positive value (favoring antiparallel alignment), which is consistent with the ferrimagnetic Type-B structure. However, the 4NN exchange coupling parameter between Mn II – Mn III(B) ions (J_{41}) is a frustrated exchange parameter with negative value that favors FM interaction despite the ferrimagnetic Type-B structure wants this interaction to be anti-ferromagnetic.

One may wonder about the DMI and SIA parameters in this system with frustration

in it. To answer such question, Table (6.2) shows the DMI and SIA coefficients for the 1NN interactions (higher NN are found to be negligible). As one can see, the extracted DMI vectors for 1NN interactions are almost negligible and such fact is consistent with 1NN spins being aligned almost parallel to each other and there is no heavy element to induce strong spin-orbit coupling, plus, the magnitude of the DMI vectors is about three orders of magnitude smaller than the corresponding 1NN J parameters. The SIA parameters are also found to be almost negligible except the SIA of Mn II, which is the strongest one and is two orders of magnitude smaller than the strongest J value while being of the same order as the strongest DMI parameter.

6.4.1 Magnetization compensation temperature

Now that we have our magnetic coupling parameters extracted from DFT calculations, let us look at the results from our MC simulations. Figure (6.2) reports the specific heat (panel a) and the total normalized magnetization (panel b), as a function of temperature. The specific heat exhibits one peak at a Curie temperature, T_C, around 700K, which is in good agreement with the experimental value of 745K [177]. Such outcome testifies the accuracy of our calculations and our decision to include up to 4NN interactions. Moreover, Fig. (6.2b) reveals that, at $T_C \approx 700K$, each magnetic sublattice begins to be spontaneously magnetized but since the system is ferrimagnetic, the Mn I and Mn II atoms adopt a positive value but the Mn III atoms go negative, as consistent with Type-B. Below T_C and down to about 500K, the magnetizations from the sublattices of Mn I and Mn II ions are dominant, making the total magnetization positive for the system. However, the magnetization magnitude of the Mn II sublattice does not increase much as that of the Mn I and, especially, Mn III sublattices as the temperature lowers. As consequence of such feature, the total magnetization changes its sign at around 496K which reveals a compensation temperature, T_M, in Mn_4N. Note that we are not aware of any findings of T_M in pure Mn_4N system, but a recent experimental study of Mn_4N (001) thin films grown on GaN (0001) substrate (for which Mn_4N is likely

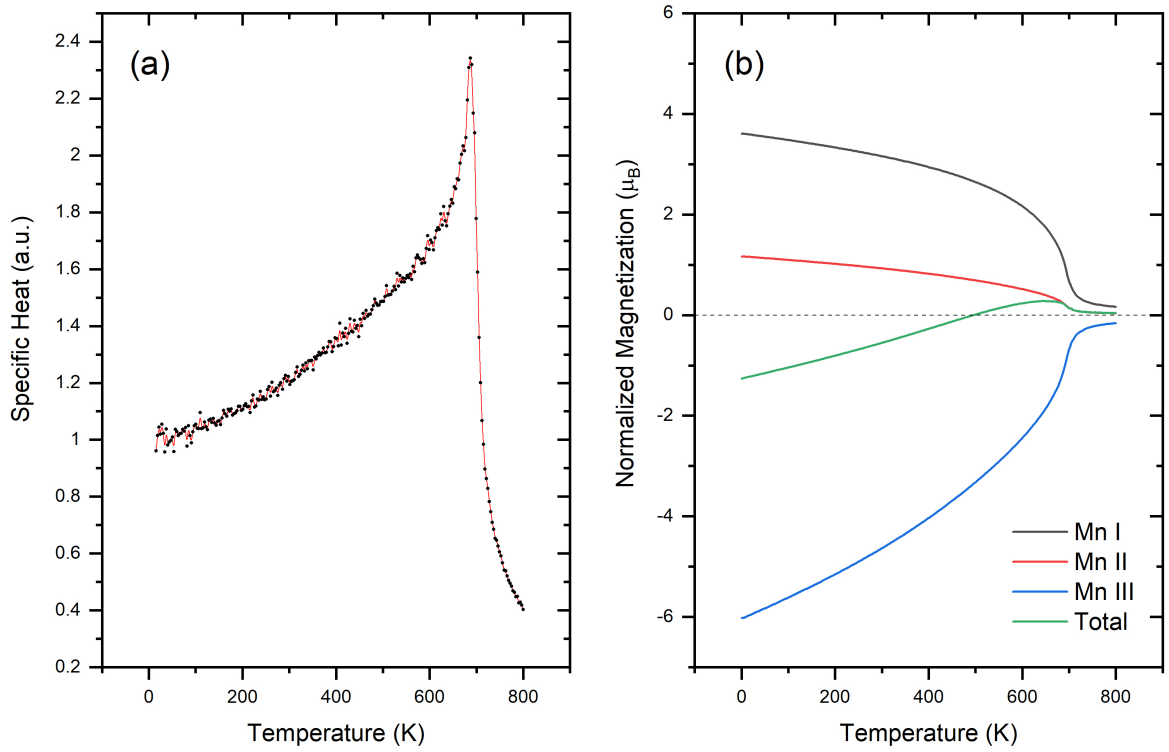

Figure 6.2: Magnetic properties as function of temperature from MC simulations. Panel (a) shows the specific heat (arb. units) and panel (b) displays the normalized total magnetic moment, as well as, the individual magnetic moments, as a function of a temperature. Note that the normalization of the individual magnetic moments in panel (b) is done to reproduce their DFT values at 0K.

elastically relaxed, i.e., does not experience any significant strain, due to its large 16% lattice mismatch with GaN) reports a sign flip from n-type to p-type in the anomalous Hall resistance hysteresis loop between 225C to 300C [198]. Interestingly, such sign flip in the anomalous Hall effect can be explained by the existence of a magnetization compensation temperature, and the reported temperature range for this sign flip is consistent with our predicted T_M of 496K. Such facts, as well as the magnetization compensation temperature experimentally found in Mn_4N system by "simply" doping it with Co, Ni, In and Sn [199–201], strongly suggest that T_M has been overlooked/missed in pure Mn_4N, before our current study.

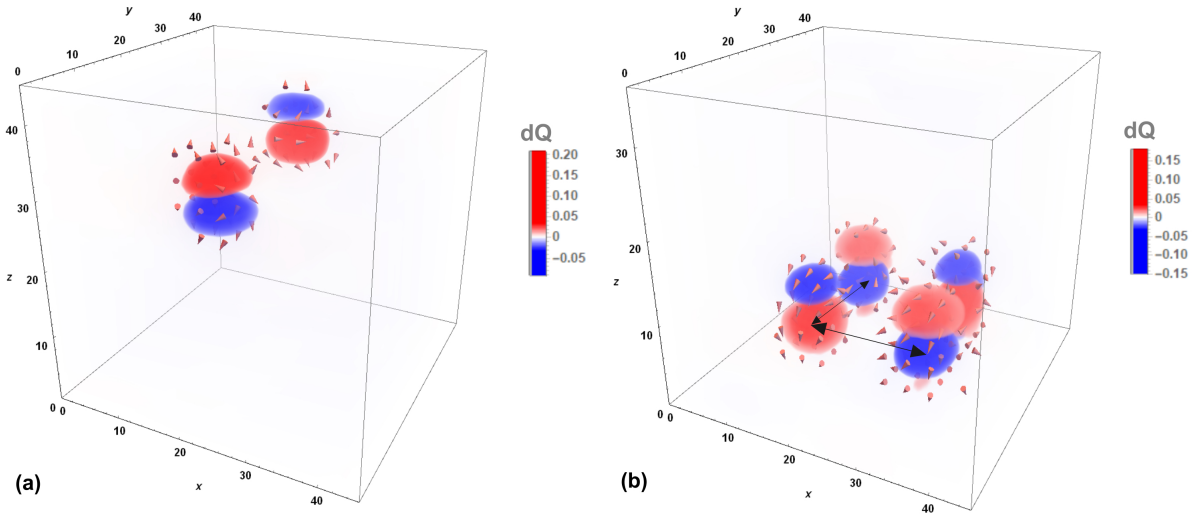

Figure 6.3: Distribution of topological charge Q and spin textures of two different states possessing hedgehog-anti-hedgehog pairs, as found from MC simulations at low temperatures. Panel (a) and (b) show a state with two and four of such pairs, respectively, within the used supercell. The red and blue colors represent opposite signs for Q, and the arrows represent the spin patterns. Note that all the blank spaces within the supercell consists of the ferrimagnetic ground state of M_n4N.

6.4.2 Topological phases

Our MC calculation results reveal a metastable states such as HAPs [202], in addition to the ferrimagnetic Type-B ground state. HAPs were previously observed in the compounds such MnGe [202] and $MnSi_{1-x}Ge_x$ [203], but never in antiperovskites (to the extend of our knowledge). The spin texture and distribution of topological charge, Q, of the newly found HAPs are shown in Fig. (6.3) for a small temperature, using the definition of Berg and Lüstcher [204] for discrete lattice spins [205]. Each hedgehog and anti-hedgehog have a area of $\approx 8\mathring{A} \times 8\mathring{A}$ in the (x,y) plane, and the distance between the bottom of one defect to the top of the other defect forming the hedgehog-anti-hedgehog pair is $\approx 10\mathring{A}$ along the c-axis. Panel (b) of Fig. (6.3) shows a hedgehog-anti-hedgehog lattice, with the overall distance between the core of the hedgehog in one pair and the core of the anti-hedgehog in the nearest pairs being $\approx 18\mathring{A}$ and such distances are illustrated by the black arrows in it. Note that such nanometric topological defects are very promising/appealing for nanoelectronics

with a fact that a cubic-lattice skyrmion was observed to be ≈3nm in MnGe [202], and could lead to novel functionality and devices [206]. Surprisingly, we are not aware of any previous reports on topological states in Mn_4N. Here, the spins of the hedgehog and anti-hedgehog topological states predicted have components parallel to the surface, in addition to the whirling of spins around its core, which is reminiscent of the hedgehog and anti-hedgehogs found in MnGe [202] and $MnSi_{1-x}Ge_x$ [203]. Furthermore, the energy differences between topological spin textures shown in Fig. (6.3) and the ferrimagnetic (Type-B) ground state are rather small, namely about 3 meV/Mn. and 0.5 meV/Mn, respectively. It is thus likely that these topological states can be observed by applying a magnetic field, as similar to the three-dimensional chiral magnetic texture called the hedgehog lattice seen under external magnetic field in MnGe compound [202, 203].

Next, let us focus on revealing the microscopic origin behind currently found HAPs states in Mn_4N. In order to do that, we compute the relative decomposed energy contributions of each J parameter toward the formation of HAPs (shown in Fig. (6.3a)) with respect to the ferrimagnetic ground state, and show it in Fig. (6.4). The decomposed energy contributions are the energy contribution from each J parameter toward the total energy difference between two states. For example, below equation shows the total energy difference between HAPs state and the ferrimagnetic ground state (FGS):

$\Delta E = (\sum_{<i,j>^A}^{1NN-4NN} \sum_{\alpha}^{x,y,z} J^A_{\alpha\alpha} S^{\alpha}_i S^{\alpha}_j)_{HAPs} - (\sum_{<i,j>^A}^{1NN-4NN} \sum_{\alpha}^{x,y,z} J^A_{\alpha\alpha} S^{\alpha}_i S^{\alpha}_j)_{FGS}$

and the relative decomposed energy contributions are derived from this equation but by considering the separate effect of each J parameter on such total energy difference. Due to their hindered feature, the two exchange frustrated J parameters, J_{26} and J_{41}, are found to have a negative decomposed energy showing their tendency toward the metastable HAPs' phase over the ferrimagnetic ground state. To check whether such frustrated exchange coupling parameters are the main source behind the HAPs state, we ran MC calculations followed by the CG method from the metastable HAPs state (shown in Fig. (6.3a)), but by flipping the signs of the frustrated J_{26} and J_{41}, to nullify their magnetic exchange frustration in the

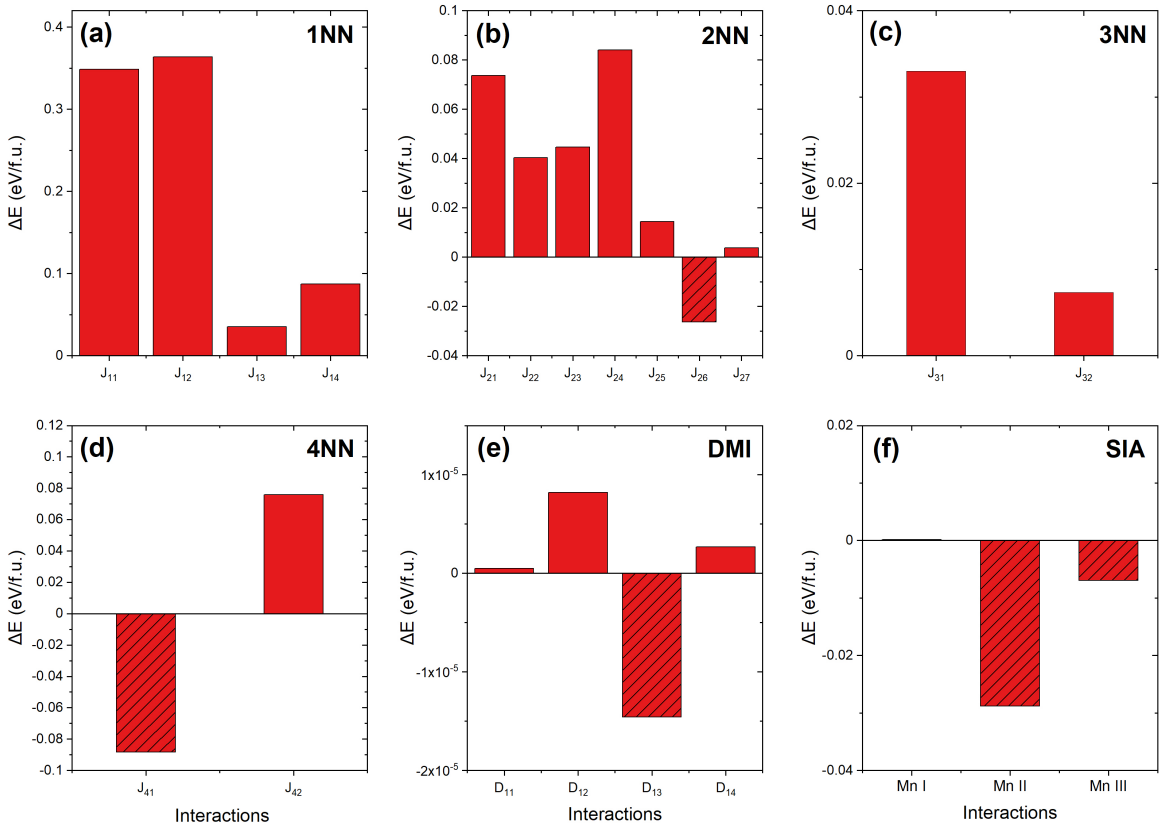

Figure 6.4: The relative-decomposed energy contributions of all J parameters for 1NN (a), 2NN (b), 3NN (c), 4NN (d), DMI (e) and SIA (f) for the hedgehog anti-hedgehog pairs shown in Fig. (6.3a). The relative decomposed energies of J parameters, DMI vectors and SIA that have negative values are shown via stripe patterns.

system. Such change in sign does not make these exchange coupling parameters frustrated anymore. As a result, we find a disappearance of the HAPs state and only the ferrimagnetic ground state remains. Furthermore, we also check the individual contribution of each frustrated Js and find that J_{41} is the main contributor to the formation of HAPs pairs which can also be explained by the findings shown in Fig. (6.4) that J_{41} has about 4 times lower decomposed energy contribution with respect to J_{26}.

Furthermore, we checked the relative decomposed energy contributions of SIA (Fig. 6.4f) and DMI vectors (Fig. (6.4e)). The decomposed energies contributions of SIA of Mn II and Mn III have negative values and thus favor the formation of HAPs. Specially, the decomposed energy contribution of SIA of Mn II is calculated to be the strongest but also to contribute to the formation of HAPs on a scale that is comparable to that of frustrated J_{26}. The DMI vector (D_{13}), corresponding to an interaction between the 1NN Mn III(A) and Mn III(B) ions, that also share the frustrated J_{13} parameter, is also found to have a negative energy which shows that it further contributes to the stabilization of the topological state. However, the contribution from D_{13} is rather weak since the decomposed energy from it is about three orders smaller than the decomposed energies of J_{26} and J_{41} interactions. In fact, we numerically checked the effect of SIA and DMI vectors on the formation of the HAPs by not considering them in our MC simulations and we do not find any noticeable change in the formation of HAPs (i.e., we still find topological states without them). Such fact that HAPs states remain, even when SIA and DMI vectors with a negative decomposed energy contributions are switched off, demonstrates that SIA and DMI are not the main contributors to the formation of these topological pairs and indicates that they are much less important than J_{41}. Such result is unusual since DMI is typically considered as the microscopic reason behind the stabilization of (non-collinear) topological states such as skyrmion [207], anti-skyrmion [208], and bimerons [209–211]. Our numerical experiments by means of MC simulations indicated above, along with Fig. (6.4), reveal that it is the frustrated exchange coupling parameters, namely J_{41} parameter with some lesser extent of the frustrated J_{26}

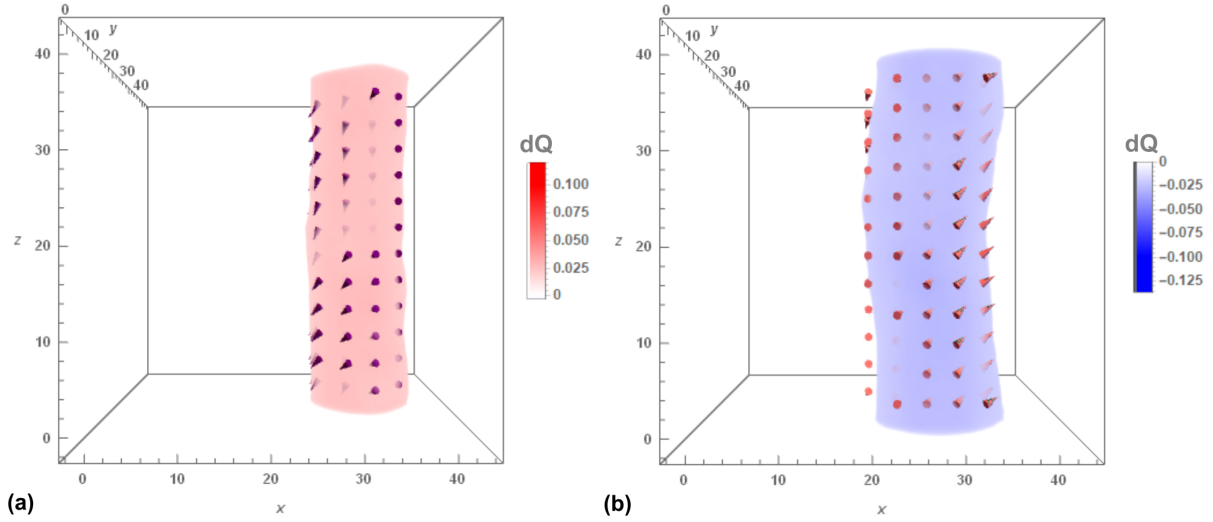

Figure 6.5: Distribution of topological charge Q and spin textures of two different skyrmion tubes. Panel (a) and (b) show the Q distribution of skyrmion tubes having opposite-in-sign topological charges (indicated in red and blue colors, respectively), with the arrows representing the spin textures

coefficient, that stabilizes such topological HAPs states in Mn_4N. Also, our present finding allows one to realize a connection between antiperovskites and (i) some other systems such as $NiGa_2S_4$, $Bi_3Mn_4O_{12}(NO_3)$, Gd_2PdSi_3, $GdRu_2Si_2$, and Pd/Fe/Ir (111) for which the competition between magnetic exchange interactions that go beyond nearest-neighbor interaction stabilizes skyrmion lattices [197, 212–221] and (ii) with pyrochlore lattice for which a recent work [222] predicted that hedgehog lattice can be induced by frustration.

Moreover, we also observed other topological states, namely skyrmion tubes, in our MC calculations. Figure (6.5) shows the distribution of topological charge Q and spin textures of two different skyrmion tubes with different polarity that was found from MC simulations at low temperatures. The diameter for these skyrmion tubes is found to be ≈ 10Å. In other words, these skyrmion tubes have an area of $\approx 10\mathring{A} \times 10\mathring{A}$ in the (x,y) plane, and form in the entirety of the supercell along the z-axis (which is the c-axis of the unit cell). Same as for the HAPs states, we report in Fig. (6.6) the relative decomposed energy contributions of J_{13} and J_{27} toward the formation of HAPs and the skyrmion tube state with respect to the

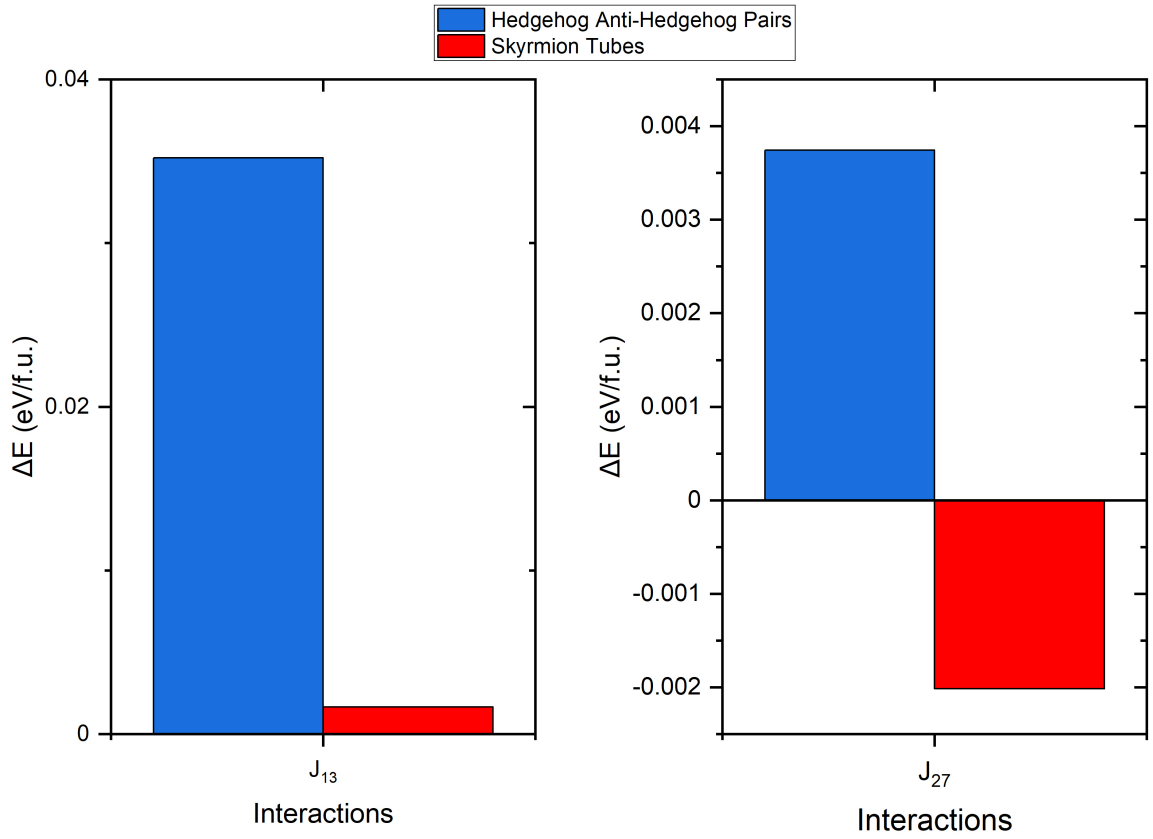

Figure 6.6: The relative-decomposed energy contributions of J_{13} and J_{27} for the hedgehog anti-hedgehog pairs and skyrmion tube states are shown in Fig. (6.3a) and Fig. (6.5), respectively

ferrimagnetic ground state. J_{13} and J_{27} were selected to be shown here due to the following reason: (i) J_{27} disfavor the hedgehog-anti-hedgehog pair state however favors the skyrmion tube state (with negative decomposed energy) with respect to the ferrimagnetic ground state; and (ii) J_{13} (note that this is a frustrated exchange coupling parameter) disfavors both HAPs and, to a much smaller extent, the skyrmion tube state, with respect to the ferrimagnetic ground state. As for the frustrated J_{41}, it was also found to favor skyrmion tube state however the decomposed energy contribution of J_{41} towards skyrmion tube state was found to be four times smaller than its contribution toward HAPs. Such fact also explains that after the CG method, skyrmion tube state was reluctant to disappear in MC simulations.

6.5 Summary

In this chapter, we studied the magnetic properties and topological spin textures of antiperovskite ferrimagnet Mn_4N by means of *ab-initio*-based simulations. The main results are as follows: (1) a sizeable magnetization compensation temperature, T_M, is found around 496K within the ferrimagnetic Type-B structure (this T_M could be tuned towards a room temperature by growing $Mn4N$ thin films on various substrates, as predicted for epitaxial films made of rare-earth iron garnet systems [135]); (2) a newly found nanometric-sized hedgehog-anti-hedgehog pairs were revealed; (3) topological states in Mn_4N system was found to be stabilized by frustrated exchange coupling parameters, mainly by J_{41} which is between 4NN Mn II and Mn III(B) ions. Such findings of our work indicate that frustration can play a critical role to largely reduce the size of topological defects (i.e., to reach nanometric-sized), which is of large benefits to advanced spintronics. We hope our predictions will motivate experimental confirmations of our findings of T_M and hedgehog-anti-hedgehog pairs in antiperovskite ferrimagnet Mn_4N, attract attention toward a very promising family of compounds of antiperoskite ferrimagnets, and will be put to use to design novel spintronic devices.

7 Summary and Outlook

In this dissertation, we did several studies on the cross coupling between structural and spin degrees of freedom in multiferroic and ferrimagnetic compounds by means of first-principles calculations and *ab-initio*-based Monte Carlo simulations. The study of magnetoelectric effects arising from different sources were covered in Chapters 3 and 4, and the examination of magnetic and topological properties of two different ferrimagnets were accomplished in Chapters 5 and 6. Note that summary of each study was included at the end of each chapter and brief summaries are as follows: (Chapter 3) a large enhancement of linear magnetoelectric coupling coefficient was found at the edge of the morphotrophic phase boundary, that was found to be associated with the large enhancement in the electric susceptibility tensor; (Chapter 4) a magnetic domain-wall induced magnetoelectric effect was found to neither require the existence of magnetism at the rare-earth sites nor non-collinear magnetism to exist, and it is rather identified to originate from a symmetric exchange-striction mechanism; (Chapter 5) the epitaxial strain effect is found to enhance magnetic properties of Rare-earth Iron Garnets by having a magnetization compensation temperature at room temperature; and (Chapter 6) previously overlooked magnetization compensation temperature and topological states were identified, and topological phases were found to be stabilized by a frustration in Mn_4N. We believe that the results from our studies shed lights to a number of different problems via comprehensive investigations and also carve a pathway for experimental studies checking the predictions of our results. Furthermore, our studies open up many new questions that are worth investigation by means of theory or experiment. They are as follows:

- Our result reveal that one can enhance the magnetoelectric coupling when there is an increase in magnetic susceptibility and we believe such effect can be observed in a ferromagnetic morphotrophic phase boundary such as the one found in Ref. [91].

- The domain-wall-induced magnetoelectric effect is found to be not depended on the

rare-earth ions, thus one could question what would happen at the interface of different rare-earth iron garnets or the interface of rare-earth iron garnet with different compounds having heavy ions. We believe the latter could lead to interesting spin-orbit coupling effects.

- Since the topological states in Mn_4N is found to be stabilized by the frustration in the system, it would be worthwhile to investigate whether epitaxial strain or doping can enhance this frustration, therefore potentially leading to more stable topological states at higher temperatures.

- Lastly, Rare-earth Iron Garnets have another exciting property called perpendicular magnetic anisotropy (PMA). PMA describes the magnetic anisotropy of the system when the direction of easy axes is perpendicular to the film surface but the direction of the hard axis is in-plane of the film. PMA makes applications more compact as density-wise and drives the switching current threshold lower as compared to a magnet with in-plane anisotropy [223–225]. The anisotropy energy of a magnetic thin film contains three terms that can alter the magnetic easy axis of the film that are related to the shape, magnetoelastic and magnetocrystalline anisotropy energies. By engineering these three terms, one can promote PMA. For example, the magnetoelastic anisotropy can induce PMA if there is a combination of a positive magnetostriction coefficient and in-plane compressive strain or a negative magnetostriction coefficient and in-plane tensile strain. Strain-induced PMA in Rare-earth Iron Garnets has been explored experimentally. However there are no theoretical studies, especially via first-principles calculations, that have been done yet (to the extend of our knowledge). In fact, we started to look at how epitaxial strain (both (001) and (111)) influence the magnetic easy axis to induce PMA in Rare-earth Iron Garnet systems. Followings are some of the preliminary results that were computed via first-principles calculations.

Let us define the PMA energy as the difference between energies with their easy axis along in-plane and out-plane directions. Here, the in-plane directions are pseudo-cubic [100] and [1-10] directions for (001) and (111) films, respectively, and out-plane directions are pseudo-cubic [001] and [111] directions for (001) and (111) films, respectively. Figure S1 shows the

Figure 7.1: PMA of different Rare-earth Iron Garnets (Gadolinium, Europium, Thulium, and Terbium) for both (001) and (111) epitaxial strains.

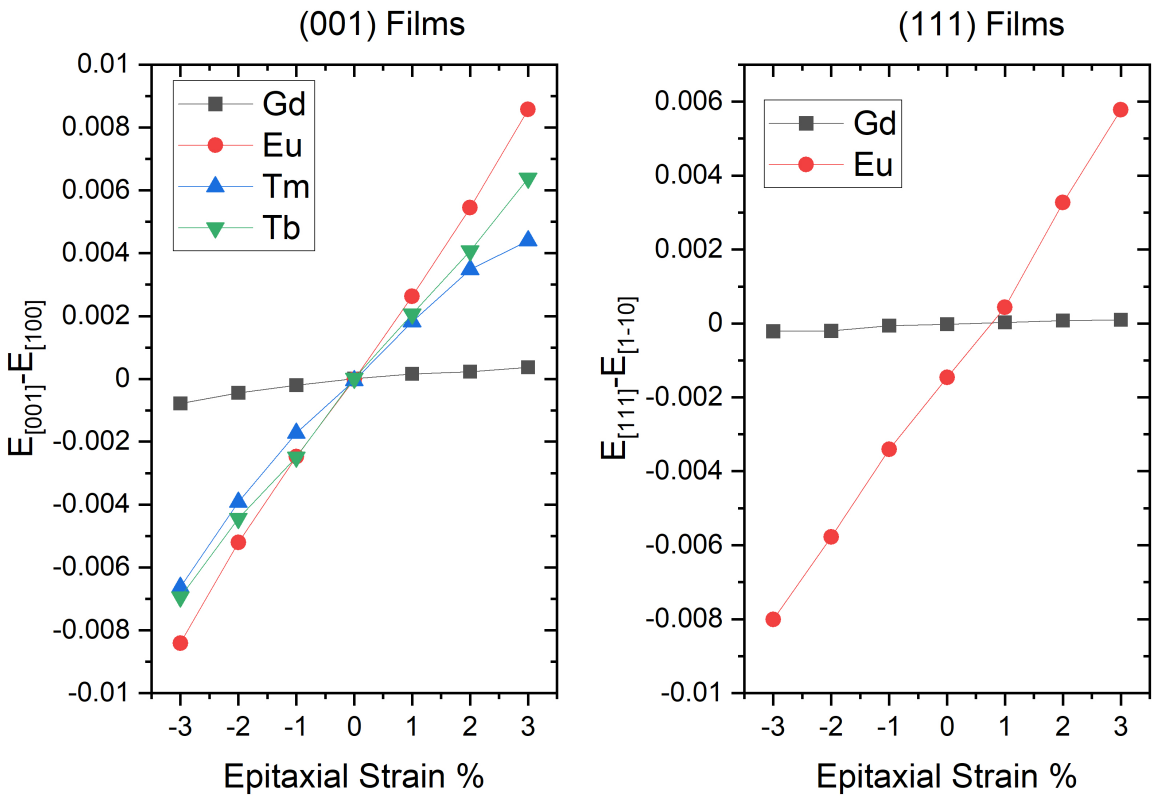

PMA energy of different Rare-earth Iron Garnets (Gadolinium, Europium, Thulium, and Terbium) for both (001) and (111) epitaxial strains. One can see that both growth direction can influence the PMA and for both cases, compressive strain is found to enhance PMA in the studied Rare-earth Iron Garnets.

A Copyright Information

Copyright policies of the American Physical Society (APS)

American Physical Society
Reuse and Permissions License

09-Nov-2021

This license agreement between the American Physical Society ("APS") and Temuujin Bayaraa ("You") consists of your license details and the terms and conditions provided by the American Physical Society and SciPris.

Licensed Content Information

License Number:	**RNP/21/NOV/046502**
License date:	09-Nov-2021
DOI:	10.1103/PhysRevB.103.L060103
Title:	Giant linear magnetoelectric effect at the morphotropic phase boundary of epitaxial ${\mathrm{Sr}}_{0.5}{\mathrm{Ba}}_{0.5}{\mathrm{MnO}}_{3}$ films
Author:	Temuujin Bayaraa et al.
Publication:	Physical Review B
Publisher:	American Physical Society
Cost:	USD $ 0.00

Request Details

Does your reuse require significant modifications: No

Specify intended distribution locations:	United States
Reuse Category:	Reuse in a thesis/dissertation
Requestor Type:	Author of requested content
Items for Reuse:	Whole Article
Format for Reuse:	Electronic

Information about New Publication:

University/Publisher:	University of Arkansas
Title of dissertation/thesis:	Interplay Between the Lattice and Spin Degrees of Freedom in Magnetoelectric and Magnetic Materials
Author(s):	Temuujin Bayaraa
Expected completion date:	Dec. 2021

License Requestor Information

Name:	Temuujin Bayaraa
Affiliation:	Individual
Email Id:	tbayaraa@uark.edu
Country:	United States

American Physical Society
Reuse and Permissions License

10-Nov-2021

This license agreement between the American Physical Society ("APS") and Temuujin Bayaraa ("You") consists of your license details and the terms and conditions provided by the American Physical Society and SciPris.

Licensed Content Information

License Number:	**RNP/21/NOV/046535**
License date:	10-Nov-2021
DOI:	10.1103/PhysRevLett.125.067602
Title:	Magnetic-Domain-Wall-Induced Electrical Polarization in Rare-Earth Iron Garnet Systems: A First-Principles Study
Author:	Temuujin Bayaraa et al.
Publication:	Physical Review Letters
Publisher:	American Physical Society
Cost:	USD $ 0.00

Request Details

Does your reuse require significant modifications: No

Specify intended distribution locations:	United States
Reuse Category:	Reuse in a thesis/dissertation
Requestor Type:	Author of requested content
Items for Reuse:	Whole Article
Format for Reuse:	Electronic

Information about New Publication:

University/Publisher:	University of Arkansas
Title of dissertation/thesis:	Interplay Between the Lattice and Spin Degrees of Freedom in Magnetoelectric and Magnetic Materials
Author(s):	Temuujin Bayaraa
Expected completion date:	Dec. 2021

License Requestor Information

Name:	Temuujin Bayaraa
Affiliation:	Individual
Email Id:	tbayaraa@uark.edu
Country:	United States

American Physical Society
Reuse and Permissions License

10-Nov-2021

This license agreement between the American Physical Society ("APS") and Temuujin Bayaraa ("You") consists of your license details and the terms and conditions provided by the American Physical Society and SciPris.

Licensed Content Information

License Number:	**RNP/21/NOV/046536**
License date:	10-Nov-2021
DOI:	10.1103/PhysRevB.100.214412
Title:	Tuning magnetization compensation and Curie temperatures in epitaxial rare earth iron garnet films
Author:	Temuujin Bayaraa et al.
Publication:	Physical Review B
Publisher:	American Physical Society
Cost:	USD $ 0.00

Request Details

Does your reuse require significant modifications: No

Specify intended distribution locations:	United States
Reuse Category:	Reuse in a thesis/dissertation
Requestor Type:	Author of requested content
Items for Reuse:	Whole Article
Format for Reuse:	Electronic

Information about New Publication:

University/Publisher:	University of Arkansas
Title of dissertation/thesis:	Interplay Between the Lattice and Spin Degrees of Freedom in Magnetoelectric and Magnetic Materials
Author(s):	Temuujin Bayaraa
Expected completion date:	Dec. 2021

License Requestor Information

Name:	Temuujin Bayaraa
Affiliation:	Individual
Email Id:	tbayaraa@uark.edu
Country:	United States

American Physical Society
Reuse and Permissions License

18-Nov-2021

This license agreement between the American Physical Society ("APS") and Temuujin Bayaraa ("You") consists of your license details and the terms and conditions provided by the American Physical Society and SciPris.

Licensed Content Information

License Number:	**RNP/21/NOV/046893**
License date:	18-Nov-2021
DOI:	10.1103/PhysRevLett.127.217204
Title:	Magnetization Compensation Temperature and Frustration-Induced Topological Defects in Ferrimagnetic Antiperovskite ${\mathrm{Mn}}_{4}\mathrm{N}$
Author:	Temuujin Bayaraa, Changsong Xu, and L. Bellaiche
Publication:	Physical Review Letters
Publisher:	American Physical Society
Cost:	USD $ 0.00

Request Details

Does your reuse require significant modifications: No

Specify intended distribution locations:	United States
Reuse Category:	Reuse in a thesis/dissertation
Requestor Type:	Author of requested content
Items for Reuse:	Whole Article
Format for Reuse:	Electronic

Information about New Publication:

University/Publisher:	University of Arkansas
Title of dissertation/thesis:	Interplay Between the Lattice and Spin Degrees of Freedom in Magnetoelectric and Magnetic Materials
Author(s):	Temuujin Bayaraa
Expected completion date:	Dec. 2021

License Requestor Information

Name:	Temuujin Bayaraa
Affiliation:	Individual
Email Id:	tbayaraa@uark.edu
Country:	United States

Bibliography

[1] N. A. Spaldin, Science **309**, 391 (2005), ISSN 0036-8075, URL https://www.science.orghttps://www.sciencemag.org/lookup/doi/10.1126/science.1113357.

[2] W. Eerenstein, N. D. Mathur, and J. F. Scott, Nature **442**, 759 (2006), ISSN 0028-0836, URL http://www.nature.com/doifinder/10.1038/nature05023.

[3] J. Barker and U. Atxitia, Journal of the Physical Society of Japan **90**, 081001 (2021), ISSN 0031-9015, URL https://doi.org/10.7566/JPSJ.90.081001https://journals.jps.jp/doi/10.7566/JPSJ.90.081001.

[4] F. Sun, D. Chen, X. Gao, and J.-M. Liu, Journal of Materiomics **7**, 281 (2021), ISSN 23528478, URL https://linkinghub.elsevier.com/retrieve/pii/S2352847820303038.

[5] T. Bayaraa, Y. Yang, H. J. Zhao, J. Íñiguez, and L. Bellaiche, Physical Review Materials **2**, 084404 (2018), ISSN 2475-9953, URL https://link.aps.org/doi/10.1103/PhysRevMaterials.2.084404.

[6] A. S. Borovik-Romanov, H. Grimmer, and M. Kenzelmann, in *International Tables for Crystallography D* (2013), vol. D, pp. 106–152, URL http://xrpp.iucr.org/cgi-bin/itr?url{_}ver=Z39.88-2003{&}rft{_}dat=what=chapter{&}volid=Db{&}chnumo=1o5{&}chvers=v0001http://xrpp.iucr.org/cgi-bin/itr?url{_}ver=Z39.88-2003{&}rft{_}dat=what{%}3Dchapter{%}26volid{%}3DDb{%}26chnumo{%}3D1o5{%}26chvers{%}3Dv0001.

[7] Y. Fang, Y. Q. Song, W. P. Zhou, R. Zhao, R. J. Tang, H. Yang, L. Y. Lv, S. G. Yang, D. H. Wang, and Y. W. Du, Scientific Reports **4**, 3860 (2015), ISSN 2045-2322, URL http://www.nature.com/articles/srep03860.

[8] S. Geller, J. P. Remeika, R. C. Sherwood, H. J. Williams, and G. P. Espinosa, Physical Review **137**, A1034 (1965), ISSN 0031-899X, URL https://link.aps.org/doi/10.1103/PhysRev.137.A1034.

[9] K. P. Belov, E. V. Talalaeva, and G. A. Yarkho, Sov. Phys. JETP **25**, 989 (1967).

[10] H. Schmid, Ferroelectrics **162**, 317 (1994), ISSN 0015-0193, URL http://www.tandfonline.com/doi/abs/10.1080/00150199408245120.

[11] T. Kimura, T. Goto, H. Shintani, K. Ishizaka, T. Arima, and Y. Tokura, Nature **426**, 55 (2003), ISSN 0028-0836, URL http://www.nature.com/articles/nature02018.

[12] J. Wang, J. B. Neaton, H. Zheng, V. Nagarajan, S. B. Ogale, B. Liu, D. Viehland, V. Vaithyanathan, D. G. Schlom, U. V. Waghmare, et al., Science (New York, N.Y.) **299**, 1719 (2003), ISSN 1095-9203, URL http://www.ncbi.nlm.nih.gov/pubmed/12637741.

[13] M. Fiebig, Journal of Physics D: Applied Physics **38**, R123 (2005), ISSN

0022-3727, URL http://stacks.iop.org/0022-3727/38/i=8/a=R01?key=crossref.debaec7d983bfa8c9af8c02008b6e621.

[14] J. Íñiguez, Physical Review Letters **101**, 117201 (2008), ISSN 0031-9007, URL https://link.aps.org/doi/10.1103/PhysRevLett.101.117201.

[15] J. C. Wojdeł and J. Íñiguez, Physical Review Letters **103**, 267205 (2009), ISSN 0031-9007, URL https://link.aps.org/doi/10.1103/PhysRevLett.103.267205.

[16] E. Bousquet, N. A. Spaldin, and K. T. Delaney, Physical Review Letters **106**, 107202 (2011), ISSN 0031-9007, URL https://link.aps.org/doi/10.1103/PhysRevLett.106.107202.

[17] A. M. Essin, J. E. Moore, and D. Vanderbilt, Physical Review Letters **102**, 146805 (2009), ISSN 0031-9007, URL https://link.aps.org/doi/10.1103/PhysRevLett.102.146805.

[18] A. M. Essin, A. M. Turner, J. E. Moore, and D. Vanderbilt, Physical Review B **81**, 205104 (2010), ISSN 1098-0121, URL https://link.aps.org/doi/10.1103/PhysRevB.81.205104.

[19] A. Malashevich, I. Souza, S. Coh, and D. Vanderbilt, New Journal of Physics **12**, 053032 (2010), ISSN 1367-2630, URL http://stacks.iop.org/1367-2630/12/i=5/a=053032?key=crossref.5eb5e36c11551267d867854a49e46ee6.

[20] A. Malashevich, S. Coh, I. Souza, and D. Vanderbilt, Physical Review B **86**, 094430 (2012), ISSN 1098-0121, URL https://link.aps.org/doi/10.1103/PhysRevB.86.094430.

[21] A. Scaramucci, E. Bousquet, M. Fechner, M. Mostovoy, and N. A. Spaldin, Physical Review Letters **109**, 197203 (2012), ISSN 0031-9007, URL https://link.aps.org/doi/10.1103/PhysRevLett.109.197203.

[22] M. Mostovoy, A. Scaramucci, N. A. Spaldin, and K. T. Delaney, Physical Review Letters **105**, 087202 (2010), ISSN 0031-9007, URL https://link.aps.org/doi/10.1103/PhysRevLett.105.087202.

[23] S. Prosandeev, I. A. Kornev, and L. Bellaiche, Physical Review B **83**, 020102 (2011), ISSN 1098-0121, URL https://link.aps.org/doi/10.1103/PhysRevB.83.020102.

[24] D. Rahmedov, D. Wang, J. Íñiguez, and L. Bellaiche, Physical Review Letters **109**, 037207 (2012), ISSN 0031-9007, URL https://link.aps.org/doi/10.1103/PhysRevLett.109.037207.

[25] J. C. Wojdeł and J. Íñiguez, Physical Review Letters **105**, 037208 (2010), ISSN 0031-9007, URL https://link.aps.org/doi/10.1103/PhysRevLett.105.037208.

[26] S. S. P. Parkin, Annual Review of Materials Science **25**, 357 (1995), ISSN 0084-6600, URL https://www.annualreviews.org/doi/abs/10.1146/annurev.ms.25.080195.002041http://www.annualreviews.org/doi/10.1146/annurev.ms.25.080195.002041.

[27] M. N. Baibich, J. M. Broto, A. Fert, F. N. Van Dau, F. Petroff, P. Etienne, G. Creuzet, A. Friederich, and J. Chazelas, Physical Review Letters **61**, 2472 (1988), ISSN 0031-9007, URL https://journals.aps.org/prl/abstract/10.1103/PhysRevLett.61.2472https://link.aps.org/doi/10.1103/PhysRevLett.61.2472.

[28] G. Binasch, P. Grünberg, F. Saurenbach, and W. Zinn, Physical Review B **39**, 4828 (1989), ISSN 0163-1829, URL https://journals.aps.org/prb/abstract/10.1103/PhysRevB.39.4828https://link.aps.org/doi/10.1103/PhysRevB.39.4828.

[29] J. E. Hirsch, Physical Review Letters **83**, 1834 (1999), ISSN 0031-9007, URL https://journals.aps.org/prl/abstract/10.1103/PhysRevLett.83.1834https://link.aps.org/doi/10.1103/PhysRevLett.83.1834.

[30] V. Edelstein, Solid State Communications **73**, 233 (1990), ISSN 00381098, URL https://linkinghub.elsevier.com/retrieve/pii/003810989090963C.

[31] J. C. R. Sánchez, L. Vila, G. Desfonds, S. Gambarelli, J. P. Attané, J. M. De Teresa, C. Magén, and A. Fert, Nature Communications **4**, 2944 (2013), ISSN 2041-1723, URL https://www.nature.com/articles/ncomms3944http://www.nature.com/articles/ncomms3944.

[32] S. Bader and S. Parkin, Annual Review of Condensed Matter Physics **1**, 71 (2010), ISSN 1947-5454, URL https://www.annualreviews.org/doi/abs/10.1146/annurev-conmatphys-070909-104123http://www.annualreviews.org/doi/10.1146/annurev-conmatphys-070909-104123.

[33] L. Caretta, M. Mann, F. Büttner, K. Ueda, B. Pfau, C. M. Günther, P. Hessing, A. Churikova, C. Klose, M. Schneider, et al., Nature Nanotechnology **13**, 1154 (2018), ISSN 1748-3387, URL http://www.nature.com/articles/s41565-018-0255-3.

[34] J. Finley and L. Liu, Applied Physics Letters **116**, 110501 (2020), ISSN 0003-6951, URL https://aip.scitation.org/doi/abs/10.1063/1.5144076http://aip.scitation.org/doi/10.1063/1.5144076.

[35] A. Kirilyuk, A. V. Kimel, and T. Rasing, Reviews of Modern Physics **82**, 2731 (2010), ISSN 0034-6861, URL https://link.aps.org/doi/10.1103/RevModPhys.82.2731.

[36] J. Walowski and M. Münzenberg, Journal of Applied Physics **120**, 140901 (2016), ISSN 0021-8979, URL https://aip.scitation.org/doi/abs/10.1063/1.4958846http://aip.scitation.org/doi/10.1063/1.4958846.

[37] R. J. Zeches, M. D. Rossell, J. X. Zhang, A. J. Hatt, Q. He, C.-H. Yang, A. Kumar, C. H. Wang, A. Melville, C. Adamo, et al., Science (New York, N.Y.) **326**, 977 (2009), ISSN 1095-9203, URL http://www.ncbi.nlm.nih.gov/pubmed/19965507.

[38] J. X. Zhang, Q. He, M. Trassin, W. Luo, D. Yi, M. D. Rossell, P. Yu, L. You, C. H. Wang, C. Y. Kuo, et al., Physical Review Letters **107**, 147602 (2011), ISSN 0031-9007, URL https://link.aps.org/doi/10.1103/PhysRevLett.107.147602.

[39] Q. He, Y. H. Chu, J. T. Heron, S. Y. Yang, W. I. Liang, C. Kuo, H. J. Lin, P. Yu, C. W. Liang, R. J. Zeches, et al., Nature Communications **2**, 225 (2011), ISSN 2041-1723, URL http://www.nature.com/doifinder/10.1038/ncomms1221.

[40] Z. Chen, Z. Luo, C. Huang, Y. Qi, P. Yang, L. You, C. Hu, T. Wu, J. Wang, C. Gao, et al., Advanced Functional Materials **21**, 133 (2011), ISSN 1616301X, URL http://doi.wiley.com/10.1002/adfm.201001867.

[41] M. Dawber, K. M. Rabe, and J. F. Scott, Reviews of Modern Physics **77**, 1083 (2005), ISSN 0034-6861, URL https://journals.aps.org/rmp/abstract/10.1103/RevModPhys.77.1083https://link.aps.org/doi/10.1103/RevModPhys.77.1083.

[42] D. G. Schlom, L.-Q. Chen, C.-B. Eom, K. M. Rabe, S. K. Streiffer, and J.-M. Triscone, Annual Review of Materials Research **37**, 589 (2007), ISSN 1531-7331, URL https://www.annualreviews.org/doi/abs/10.1146/annurev.matsci.37.061206.113016http://www.annualreviews.org/doi/10.1146/annurev.matsci.37.061206.113016.

[43] J. C. Agar, S. Pandya, R. Xu, A. K. Yadav, Z. Liu, T. Angsten, S. Saremi, M. Asta, R. Ramesh, and L. W. Martin, MRS Communications **6**, 151 (2016), ISSN 2159-6859, URL https://www.cambridge.org/core/journals/mrs-communications/article/frontiers-in-strainengineered-multifunctional-ferroic-materials/95E71B1B18C06C02A60359A580051DA3http://link.springer.com/10.1557/mrc.2016.29.

[44] P. S. Wang and H. J. Xiang, Physical Review X **4**, 011035 (2014), ISSN 2160-3308, URL https://journals.aps.org/prx/abstract/10.1103/PhysRevX.4.011035https://link.aps.org/doi/10.1103/PhysRevX.4.011035.

[45] N. W. Ashcroft and Mermin N. David, *Solid State Physics* (Holt Rinehart and Winston, New York, 1976), ISBN 9780030839931.

[46] P. Hohenberg and W. Kohn, Physical Review **136**, B864 (1964), ISSN 0031-899X, URL https://link.aps.org/doi/10.1103/PhysRev.136.B864.

[47] W. Kohn and L. J. Sham, Physical Review **140**, A1133 (1965), ISSN 0031-899X, URL https://link.aps.org/doi/10.1103/PhysRev.140.A1133.

[48] J. P. Perdew and A. Zunger, Physical Review B **23**, 5048 (1981), ISSN 0163-1829, URL https://link.aps.org/doi/10.1103/PhysRevB.23.5048.

[49] J. P. Perdew, K. Burke, and M. Ernzerhof, Physical Review Letters **77**, 3865 (1996), ISSN 0031-9007, URL https://link.aps.org/doi/10.1103/PhysRevLett.77.3865.

[50] G. Dresselhaus, Physical Review **100**, 580 (1955), ISSN 0031-899X, URL https://journals.aps.org/pr/abstract/10.1103/PhysRev.100.580https://link.aps.org/doi/10.1103/PhysRev.100.580.

[51] RASHBA and E., Sov. Phys.-Solid State **2**, 1109 (1960), URL https://ci.nii.ac.jp/

naid/10018760249.

[52] A. I. Lichtenstein, M. I. Katsnelson, and G. Kotliar, Physical Review Letters **87**, 067205 (2001), ISSN 0031-9007, URL https://journals.aps.org/prl/abstract/10.1103/PhysRevLett.87.067205https://link.aps.org/doi/10.1103/PhysRevLett.87.067205.

[53] J. Braun, J. Minár, H. Ebert, M. I. Katsnelson, and A. I. Lichtenstein, Physical Review Letters **97**, 227601 (2006), ISSN 0031-9007, URL https://journals.aps.org/prl/abstract/10.1103/PhysRevLett.97.227601https://link.aps.org/doi/10.1103/PhysRevLett.97.227601.

[54] A. Grechnev, I. Di Marco, M. I. Katsnelson, A. I. Lichtenstein, J. Wills, and O. Eriksson, Physical Review B **76**, 035107 (2007), ISSN 1098-0121, URL https://journals.aps.org/prb/abstract/10.1103/PhysRevB.76.035107https://link.aps.org/doi/10.1103/PhysRevB.76.035107.

[55] S. Chadov, J. Minár, M. I. Katsnelson, H. Ebert, D. Ködderitzsch, and A. I. Lichtenstein, EPL (Europhysics Letters) **82**, 37001 (2008), ISSN 0295-5075, URL www.epljournal.orghttps://iopscience.iop.org/article/10.1209/0295-5075/82/37001.

[56] J. Hubbard, Proceedings of the Royal Society of London. Series A. Mathematical and Physical Sciences **276**, 238 (1963), ISSN 0080-4630, URL https://royalsocietypublishing.org/doi/abs/10.1098/rspa.1963.0204https://royalsocietypublishing.org/doi/10.1098/rspa.1963.0204.

[57] A. I. Liechtenstein, V. I. Anisimov, and J. Zaanen, Physical Review B **52**, R5467 (1995), ISSN 0163-1829, URL https://link.aps.org/doi/10.1103/PhysRevB.52.R5467.

[58] S. L. Dudarev, G. A. Botton, S. Y. Savrasov, C. J. Humphreys, and A. P. Sutton, Physical Review B **57**, 1505 (1998), ISSN 0163-1829, URL https://link.aps.org/doi/10.1103/PhysRevB.57.1505.

[59] T. Moriya, Physical Review **120**, 91 (1960), ISSN 0031899X.

[60] H. Xiang, C. Lee, H.-J. Koo, X. Gong, and M.-H. Whangbo, Dalton Trans. **42**, 823 (2013), ISSN 1477-9226, URL http://xlink.rsc.org/?DOI=C2DT31662E.

[61] R. Resta, Ferroelectrics **136**, 51 (1992), ISSN 0015-0193, URL http://www.tandfonline.com/doi/abs/10.1080/00150199208016065.

[62] R. Resta, Reviews of Modern Physics **66**, 899 (1994), ISSN 0034-6861, URL https://link.aps.org/doi/10.1103/RevModPhys.66.899.

[63] R. D. King-Smith and D. Vanderbilt, Physical Review B **47**, 1651 (1993), ISSN 0163-1829, URL https://link.aps.org/doi/10.1103/PhysRevB.47.1651.

[64] R. Ramesh and N. A. Spaldin, Nature Materials **6**, 21 (2007), ISSN 1476-1122, URL http://www.nature.com/articles/nmat1805.

[65] D. Khomskii, Physics **2**, 20 (2009), ISSN 1943-2879, URL http://link.aps.org/doi/10.1103/Physics.2.20https://link.aps.org/doi/10.1103/Physics.2.20.

[66] D. Pantel, S. Goetze, D. Hesse, and M. Alexe, Nature Materials **11**, 289 (2012), ISSN 14764660.

[67] R. O. Cherifi, V. Ivanovskaya, L. C. Phillips, A. Zobelli, I. C. Infante, E. Jacquet, V. Garcia, S. Fusil, P. R. Briddon, N. Guiblin, et al., Nature Materials **13**, 345 (2014), ISSN 14764660.

[68] H. J. Zhao, W. Ren, Y. Yang, J. Íñiguez, X. M. Chen, and L. Bellaiche, Nature Communications **5**, 4021 (2014), ISSN 2041-1723, URL http://www.nature.com/doifinder/10.1038/ncomms5021.

[69] A. Kumar, G. L. Sharma, R. S. Katiyar, R. Pirc, R. Blinc, and J. F. Scott, Journal of Physics: Condensed Matter **21**, 382204 (2009), ISSN 0953-8984, URL https://iopscience.iop.org/article/10.1088/0953-8984/21/38/382204.

[70] J. F. Scott, *Room-temperature multiferroic magnetoelectrics* (2013).

[71] D. Evans, A. Schilling, A. Kumar, D. Sanchez, N. Ortega, M. Arredondo, R. Katiyar, J. Gregg, and J. Scott, Nature Communications **4**, 1534 (2013), ISSN 2041-1723, URL http://www.nature.com/articles/ncomms2548.

[72] O. Diéguez and J. Iñiguez, Physical Review Letters **107**, 057601 (2011), ISSN 10797114, 1105.2043.

[73] K. Oka, T. Koyama, T. Ozaaki, S. Mori, Y. Shimakawa, and M. Azuma, Angewandte Chemie International Edition **51**, 7977 (2012), ISSN 14337851, URL http://doi.wiley.com/10.1002/anie.201202644.

[74] C. M. Fernández-Posada, H. Amorín, C. Correas, O. Peña, M. Algueró, and A. Castro, Journal of Materials Chemistry C **3**, 2255 (2015), ISSN 20507526.

[75] C. M. Fernández-Posada, A. Castro, J.-M. Kiat, F. Porcher, O. Peña, M. Algueró, and H. Amorín, Nature Communications **7**, 12772 (2016), ISSN 2041-1723, URL http://www.nature.com/articles/ncomms12772.

[76] P. Mandal, M. J. Pitcher, J. Alaria, H. Niu, P. Borisov, P. Stamenov, J. B. Claridge, and M. J. Rosseinsky, Nature **525**, 363 (2015), ISSN 14764687.

[77] G. Kresse and J. Furthmüller, Physical Review B **54**, 11169 (1996), ISSN 0163-1829, URL https://link.aps.org/doi/10.1103/PhysRevB.54.11169.

[78] T. Moriya, Physical Review Letters **4**, 228 (1960), ISSN 0031-9007, URL https://link.aps.org/doi/10.1103/PhysRevLett.4.228.

[79] H. T. Stokes and D. M. Hatch, J. Appl. Cryst. J. Appl. Cryst **38**, 237 (2005), ISSN 0021-8898, URL http://journals.iucr.org/j/services/authorservices.html.

[80] M. Ye and D. Vanderbilt, Physical Review B **89**, 064301 (2014), ISSN 1098-0121, URL https://link.aps.org/doi/10.1103/PhysRevB.89.064301.

[81] M. Ye and D. Vanderbilt, Physical Review B **92**, 035107 (2015), ISSN 1098-0121, URL https://link.aps.org/doi/10.1103/PhysRevB.92.035107.

[82] H. Tian, L. Bellaiche, and Y. Yang, Physical Review B **100**, 220103(R) (2019), ISSN 24699969.

[83] E. Kita, K. Siratori, and A. Tasaki, Journal of Applied Physics **50**, 7748 (1979), ISSN 00218979, URL http://scitation.aip.org/content/aip/journal/jap/50/B11/10.1063/1.326810.

[84] A. Togo and I. Tanaka, Scripta Materialia **108**, 1 (2015), ISSN 13596462, 1506.08498.

[85] H. Sakai, J. Fujioka, T. Fukuda, D. Okuyama, D. Hashizume, F. Kagawa, H. Nakao, Y. Murakami, T. Arima, A. Q. R. Baron, et al., Physical Review Letters **107**, 1 (2011), ISSN 00319007.

[86] G. F. Ruse and S. Geller, Journal of Crystal Growth **29**, 305 (1975), ISSN 00220248.

[87] M. Kawasaki, K. Takahashi, T. Maeda, R. Tsuchiya, M. Shinohara, O. Ishiyama, T. Yonezawa, M. Yoshimoto, and H. Koinuma, Science **266**, 1540 (1994), ISSN 00368075, URL https://science.sciencemag.org/content/266/5190/1540https://science.sciencemag.org/content/266/5190/1540.abstract.

[88] A. Edström and C. Ederer, Physical Review Research **2**, 043183 (2020), ISSN 2643-1564, URL https://link.aps.org/doi/10.1103/PhysRevResearch.2.043183.

[89] A. Edström and C. Ederer, Physical Review Letters **124**, 167201 (2020), ISSN 0031-9007, URL https://link.aps.org/doi/10.1103/PhysRevLett.124.167201.

[90] A. Edström and C. Ederer, Physical Review Materials **2**, 104409 (2018), ISSN 2475-9953, 1807.04777, URL https://journals.aps.org/prmaterials/abstract/10.1103/PhysRevMaterials.2.104409https://link.aps.org/doi/10.1103/PhysRevMaterials.2.104409.

[91] S. Yang, H. Bao, C. Zhou, Y. Wang, X. Ren, Y. Matsushita, Y. Katsuya, M. Tanaka, K. Kobayashi, X. Song, et al., Physical Review Letters **104**, 197201 (2010), ISSN 00319007.

[92] A. I. Popov, Z. V. Gareeva, F. A. Mazhitova, and R. A. Doroshenko, Journal of Magnetism and Magnetic Materials **461**, 128 (2018), ISSN 03048853.

[93] Y. Geng, H. Das, A. L. Wysocki, X. Wang, S. W. Cheong, M. Mostovoy, C. J. Fennie, and W. Wu, Nature Materials **13**, 163 (2014), ISSN 14761122.

[94] M. Matsubara, S. Manz, M. Mochizuki, T. Kubacka, A. Iyama, N. Aliouane, T. Kimura, S. L. Johnson, D. Meier, and M. Fiebig, Science **348**, 1112 (2015), ISSN

10959203.

[95] S. Matzen and S. Fusil, *Domains and domain walls in multiferroics* (2015).

[96] M. Fiebig, T. Lottermoser, D. Fröhlich, A. V. Goltsev, and R. V. Pisarev, Nature **419**, 818 (2002), ISSN 0028-0836, URL http://www.nature.com/articles/nature01077.

[97] F. Kagawa, M. Mochizuki, Y. Onose, H. Murakawa, Y. Kaneko, N. Furukawa, and Y. Tokura, Physical Review Letters **102**, 057604 (2009), ISSN 00319007, 0902.1411.

[98] D. Meier, *Functional domain walls in multiferroics* (2015).

[99] T. Xu, T. Shimada, Y. Araki, J. Wang, and T. Kitamura, Nano Letters **16**, 454 (2016), ISSN 1530-6984, URL https://pubs.acs.org/doi/10.1021/acs.nanolett.5b04113.

[100] A. I. Popov, Z. V. Gareeva, and A. K. Zvezdin, Physical Review B **92**, 144420 (2015), ISSN 1098-0121, URL https://link.aps.org/doi/10.1103/PhysRevB.92.144420.

[101] J. Fontcuberta, V. Skumryev, V. Laukhin, X. Granados, and E. K. Salje, Scientific Reports **5**, 1 (2015), ISSN 20452322.

[102] I. P. Lobzenko, P. P. Goncharov, and N. V. Ter-Oganessian, Journal of Physics Condensed Matter **27**, 246002 (2015), ISSN 1361648X, 1501.06372.

[103] Z. V. Gareeva, O. Diéguez, J. Íñiguez, and A. K. Zvezdin, physica status solidi (RRL) - Rapid Research Letters **10**, 209 (2016), ISSN 18626254, URL http://doi.wiley.com/10.1002/pssr.201510273.

[104] A. I. Popov, K. A. Zvezdin, Z. V. Gareeva, F. A. Mazhitova, R. M. Vakhitov, A. R. Yumaguzin, and A. K. Zvezdin, Journal of Physics Condensed Matter **28** (2016), ISSN 1361648X.

[105] A. S. Logginov, G. A. Meshkov, A. V. Nikolaev, and A. P. Pyatakov, JETP Letters **86**, 115 (2007), ISSN 0021-3640, URL http://link.springer.com/10.1134/S0021364007140093.

[106] G. Catalan, J. Seidel, R. Ramesh, and J. F. Scott, Reviews of Modern Physics **84**, 119 (2012), ISSN 15390756.

[107] G. V. Arzamastseva, A. M. Balbashov, F. V. Lisovskii, E. G. Mansvetova, A. G. Temiryazev, and M. P. Temiryazeva, Journal of Experimental and Theoretical Physics **120**, 687 (2015), ISSN 10637761.

[108] A. P. Pyatakov, A. K. Zvezdin, A. M. Vlasov, A. S. Sergeev, D. A. Sechin, E. P. Nikolaeva, A. V. Nikolaev, H. Chou, S. J. Sun, and L. E. Calvet, in *Ferroelectrics* (Taylor & Francis Group, 2012), vol. 438, pp. 79–88, ISSN 00150193.

[109] V. Koronovskyy and Y. Vakyla, Electronic Materials Letters **11**, 1028 (2015), ISSN 20936788.

[110] I. Veshchunov, S. Mironov, W. Magrini, V. Stolyarov, A. Rossolenko, V. Skidanov, J.-B. Trebbia, A. Buzdin, P. Tamarat, and B. Lounis, Physical Review Letters **115**, 027601 (2015), ISSN 0031-9007, URL https://link.aps.org/doi/10.1103/PhysRevLett.115.027601.

[111] N. E. Khokhlov, A. E. Khramova, E. P. Nikolaeva, T. B. Kosykh, A. V. Nikolaev, A. K. Zvezdin, A. P. Pyatakov, and V. I. Belotelov, Scientific Reports **7**, 1 (2017), ISSN 20452322.

[112] S. W. Cheong and M. Mostovoy, *Multiferroics: A magnetic twist for ferroelectricity* (2007).

[113] A. P. Pyatakov, D. A. Sechin, A. S. Sergeev, A. V. Nikolaev, E. P. Nikolaeva, A. S. Logginov, and A. K. Zvezdin, EPL **93** (2011), ISSN 02955075.

[114] D. P. Kulikova, T. T. Gareev, E. P. Nikolaeva, T. B. Kosykh, A. V. Nikolaev, Z. A. Pyatakova, A. K. Zvezdin, and A. P. Pyatakov, *The Mechanisms of Electric Field-Induced Magnetic Bubble Domain Blowing* (2018), URL http://doi.wiley.com/10.1002/pssr.201800066.

[115] A. I. Popov, D. I. Plokhov, and A. K. Zvezdin, Physical Review B **90** (2014), ISSN 1550235X, 1411.0384.

[116] E. R. Rosenberg, L. Beran, C. O. Avci, C. Zeledon, B. Song, C. Gonzalez-Fuentes, J. Mendil, P. Gambardella, M. Veis, C. Garcia, et al., Physical Review Materials **2**, 094405 (2018), ISSN 2475-9953, URL https://link.aps.org/doi/10.1103/PhysRevMaterials.2.094405.

[117] K. Shen, Physical Review B **99**, 024417 (2019), ISSN 2469-9950, URL https://link.aps.org/doi/10.1103/PhysRevB.99.024417.

[118] S. Geprägs, A. Kehlberger, F. D. Coletta, Z. Qiu, E.-J. Guo, T. Schulz, C. Mix, S. Meyer, A. Kamra, M. Althammer, et al., Nature Communications **7**, 10452 (2016), ISSN 2041-1723, URL https://www.nature.com/articles/ncomms10452{#}supplementary-information.

[119] R. Nakamoto, B. Xu, C. Xu, H. Xu, and L. Bellaiche, Physical Review B **95**, 024434 (2017), ISSN 2469-9950, URL https://link.aps.org/doi/10.1103/PhysRevB.95.024434.

[120] S. M. Zanjani and M. C. Onbasli, Cite as: AIP Advances **9**, 35024 (2019), URL http://creativecommons.org/licenses/by/4.0/.

[121] M. Deb, P. Molho, B. Barbara, and J.-Y. Bigot, Physical Review B **97**, 134419 (2018), ISSN 2469-9950, URL https://link.aps.org/doi/10.1103/PhysRevB.97.134419.

[122] E. Sawatzky and E. Kay, Journal of Applied Physics **40**, 1460 (1969), ISSN 0021-8979, URL http://aip.scitation.org/doi/10.1063/1.1657720.

[123] E. Sawatzky and E. Kay, Journal of Applied Physics **42**, 367 (1971), ISSN 0021-8979,

URL http://aip.scitation.org/doi/10.1063/1.1659603.

[124] M. Oron, I. Barlow, and W. F. Traber, Journal of Materials Science **4**, 271 (1969), ISSN 0022-2461, URL http://link.springer.com/10.1007/BF00549928.

[125] D. Bloch, F. Chaissé, and R. Pauthenet, Journal of Applied Physics **38**, 1029 (1967), ISSN 0021-8979, URL http://aip.scitation.org/doi/10.1063/1.1709474.

[126] W. Haubenreisser, Kristall und Technik **14**, 1490 (1979), ISSN 00234753, URL http://doi.wiley.com/10.1002/crat.19790141215.

[127] H. Adachi and H. Ino, Nature **401**, 148 (1999), ISSN 0028-0836, URL http://www.nature.com/articles/43634.

[128] Y. Cao, S. Cao, W. Ren, Z. Feng, S. Yuan, B. Kang, B. Lu, and J. Zhang, Applied Physics Letters **104**, 232405 (2014), ISSN 0003-6951, URL http://aip.scitation.org/doi/10.1063/1.4882642.

[129] H. J. Zhao, J. Íñiguez, X. M. Chen, and L. Bellaiche, Physical Review B **93**, 014417 (2016), ISSN 2469-9950, URL https://link.aps.org/doi/10.1103/PhysRevB.93.014417.

[130] G. Kresse and D. Joubert, Physical Review B **59**, 1758 (1999), ISSN 0163-1829, URL https://link.aps.org/doi/10.1103/PhysRevB.59.1758.

[131] P. E. Blöchl, Physical Review B **50**, 17953 (1994), ISSN 0163-1829, URL https://link.aps.org/doi/10.1103/PhysRevB.50.17953.

[132] J. P. Perdew, A. Ruzsinszky, G. I. Csonka, O. A. Vydrov, G. E. Scuseria, L. A. Constantin, X. Zhou, and K. Burke, Physical Review Letters **100**, 136406 (2008), ISSN 0031-9007, URL https://link.aps.org/doi/10.1103/PhysRevLett.100.136406.

[133] O. Diéguez, O. E. González-Vázquez, J. C. Wojdeł, and J. Íñiguez, Physical Review B **83**, 094105 (2011), ISSN 1098-0121, URL https://link.aps.org/doi/10.1103/PhysRevB.83.094105.

[134] C. Xu, Y. Yang, S. Wang, W. Duan, B. Gu, and L. Bellaiche, Physical Review B **89**, 205122 (2014), ISSN 1098-0121, URL https://link.aps.org/doi/10.1103/PhysRevB.89.205122.

[135] T. Bayaraa, C. Xu, D. Campbell, and L. Bellaiche, Physical Review B **100**, 214412 (2019), ISSN 2469-9950, URL https://doi.org/10.1103/PhysRevB.100.214412https://link.aps.org/doi/10.1103/PhysRevB.100.214412.

[136] I. Dzyaloshinsky, Journal of Physics and Chemistry of Solids **4**, 241 (1958), ISSN 0022-3697, URL https://www.sciencedirect.com/science/article/abs/pii/0022369758900763.

[137] A. I. Popov, Z. V. Gareeva, A. K. Zvezdin, T. T. Gareev, A. S. Sergeev, and A. P. Pyatakov, Ferroelectrics **509**, 32 (2017), ISSN 0015-0193, URL https://www.tandfonline.

com/doi/full/10.1080/00150193.2017.1292111.

[138] N. Hur, S. Park, S. Guha, A. Borissov, V. Kiryukhin, and S. W. Cheong, Applied Physics Letters **87** (2005), ISSN 00036951.

[139] M. Mercier, Proceedings of the Symposium on Magnetoelectric Interaction Phenomena in Crystals, Seattle, Wash, USA (1973).

[140] M. J. Cardwell, Physica Status Solidi (b) **45**, 597 (1971), ISSN 03701972, URL http://doi.wiley.com/10.1002/pssb.2220450223.

[141] S. Hirakata, M. Tanaka, K. Kohn, E. Kita, K. Siratori, S. Kimura, and A. Tasaki, Journal of the Physical Society of Japan **60**, 294 (1991), ISSN 0031-9015, URL http://journals.jps.jp/doi/10.1143/JPSJ.60.294.

[142] H. Ogawa, E. Kita, Y. Mochida, K. Kohn, S. Kimura, A. Tasaki, and K. Siratori, Journal of the Physical Society of Japan **56**, 452 (1987), ISSN 0031-9015, URL http://journals.jps.jp/doi/10.1143/JPSJ.56.452.

[143] R. V. Pisarev, B. B. Krichevtsov, V. N. Gridnev, V. P. Klin, D. Frohlich, and C. Pahlke-Lerch, Journal of Physics: Condensed Matter **5**, 8621 (1993), ISSN 0953-8984, URL http://stacks.iop.org/0953-8984/5/i=45/a=015?key=crossref.d8471a14923ca01265570052c84b5118.

[144] V. E. Koronovskyy, S. M. Ryabchenko, and V. F. Kovalenko, Physical Review B - Condensed Matter and Materials Physics **71** (2005), ISSN 10980121.

[145] Y. Kohara, Y. Yamasaki, Y. Onose, and Y. Tokura, Physical Review B - Condensed Matter and Materials Physics **82** (2010), ISSN 10980121.

[146] A. S. Logginov, G. A. Meshkov, A. V. Nikolaev, E. P. Nikolaeva, A. P. Pyatakov, and A. K. Zvezdin, Applied Physics Letters **93**, 182510 (2008), ISSN 0003-6951, URL http://aip.scitation.org/doi/10.1063/1.3013569.

[147] Y. Naito, K. Sato, Y. Yasui, Y. Kobayashi, Y. Kobayashi, and M. Sato, Journal of the Physical Society of Japan **76** (2007), ISSN 00319015.

[148] Y. Yang, H. Xiang, H. Zhao, A. Stroppa, J. Zhang, S. Cao, J. Íñiguez, L. Bellaiche, and W. Ren, Physical Review B **96** (2017), ISSN 24699969.

[149] H. J. Xiang, E. J. Kan, Y. Zhang, M. H. Whangbo, and X. G. Gong, Physical Review Letters **107** (2011), ISSN 00319007.

[150] H. J. Xiang, E. J. Kan, S.-H. Wei, M.-H. Whangbo, and X. G. Gong, Physical Review B **84**, 224429 (2011), ISSN 1098-0121, URL https://link.aps.org/doi/10.1103/PhysRevB.84.224429.

[151] X. Z. Lu, M.-H. Whangbo, S. Dong, X. G. Gong, and H. J. Xiang, Physical Review Letters **108**, 187204 (2012), ISSN 0031-9007, URL https://link.aps.org/doi/10.1103/

PhysRevLett.108.187204.

[152] Z. Yu, C. Wei, F. Yi, and R. Xiong, Nanomaterials **9**, 1538 (2019), ISSN 2079-4991, URL https://www.mdpi.com/2079-4991/9/11/1538.

[153] S. H. Yang, K. S. Ryu, and S. Parkin, Nature Nanotechnology **10**, 221 (2015), ISSN 17483395.

[154] J. F. Scott, L. Kammerdiner, M. Parris, S. Traynor, V. Ottenbacher, A. Shawabkeh, and W. F. Oliver, Journal of Applied Physics **64**, 787 (1988), ISSN 00218979, URL http://aip.scitation.org/doi/10.1063/1.341925.

[155] T. T. Gao, T. L. Sun, X. Q. Liu, H. Y. Zhou, H. Tian, L. Bellaiche, and X. M. Chen, Applied Physics Letters **114**, 212904 (2019), ISSN 00036951, URL http://aip.scitation.org/doi/10.1063/1.5094509.

[156] R. Meyer, R. Waser, K. Prume, T. Schmitz, and S. Tiedke, Applied Physics Letters **86**, 1 (2005), ISSN 00036951, URL http://aip.scitation.org/doi/10.1063/1.1897425.

[157] M. Fukunaga and Y. Noda, Journal of the Physical Society of Japan **77** (2008), ISSN 00319015.

[158] M. Kubota, A. Tsukazaki, F. Kagawa, K. Shibuya, Y. Tokunaga, M. Kawasaki, and Y. Tokura, Applied Physics Express **5**, 103002 (2012), ISSN 1882-0778, URL https://iopscience.iop.org/article/10.1143/APEX.5.103002https://iopscience.iop.org/article/10.1143/APEX.5.103002/meta.

[159] M. Kubota, K. Shibuya, Y. Tokunaga, F. Kagawa, A. Tsukazaki, Y. Tokura, and M. Kawasaki, Journal of Magnetism and Magnetic Materials **339**, 63 (2013), ISSN 03048853, URL https://linkinghub.elsevier.com/retrieve/pii/S030488531300139X.

[160] C. N. Wu, C. C. Tseng, Y. T. Fanchiang, C. K. Cheng, K. Y. Lin, S. L. Yeh, S. R. Yang, C. T. Wu, T. Liu, M. Wu, et al., Scientific Reports **8**, 11087 (2018), ISSN 2045-2322, URL https://www.nature.com/articles/s41598-018-29493-5http://www.nature.com/articles/s41598-018-29493-5.

[161] C. N. Wu, C. C. Tseng, K. Y. Lin, C. K. Cheng, S. L. Yeh, Y. T. Fanchiang, M. Hong, and J. Kwo, AIP Advances **8**, 055904 (2018), ISSN 2158-3226, URL http://aip.scitation.org/doi/10.1063/1.5006673.

[162] C. O. Avci, A. Quindeau, C.-F. Pai, M. Mann, L. Caretta, A. S. Tang, M. C. Onbasli, C. A. Ross, and G. S. D. Beach, Nature Materials **16**, 309 (2017), ISSN 1476-1122, URL http://www.nature.com/articles/nmat4812.

[163] A. Quindeau, C. O. Avci, W. Liu, C. Sun, M. Mann, A. S. Tang, M. C. Onbasli, D. Bono, P. M. Voyles, Y. Xu, et al., Advanced Electronic Materials **3**, 1600376 (2017), ISSN 2199-160X, URL https://onlinelibrary.wiley.com/doi/full/10.1002/aelm.201600376https://onlinelibrary.wiley.com/doi/abs/10.1002/aelm.201600376https:

//onlinelibrary.wiley.com/doi/10.1002/aelm.201600376.

[164] P. Li, J. Kally, S. S.-L. Zhang, T. Pillsbury, J. Ding, G. Csaba, J. Ding, J. S. Jiang, Y. Liu, R. Sinclair, et al., Science Advances **5** (2019), ISSN 2375-2548, URL https://www.science.org/doi/abs/10.1126/sciadv.aaw3415https://www.science.org/doi/10.1126/sciadv.aaw3415.

[165] S. Vélez, J. Schaab, M. S. Wörnle, M. Müller, E. Gradauskaite, P. Welter, C. Gutgsell, C. Nistor, C. L. Degen, M. Trassin, et al., Nature Communications **10**, 4750 (2019), ISSN 2041-1723, URL https://www.nature.com/articles/s41467-019-12676-7http://www.nature.com/articles/s41467-019-12676-7.

[166] C. Tang, C.-Z. Chang, G. Zhao, Y. Liu, Z. Jiang, C.-X. Liu, M. R. McCartney, D. J. Smith, T. Chen, J. S. Moodera, et al., Science Advances **3** (2017), ISSN 2375-2548, URL https://www.science.org/doi/abs/10.1126/sciadv.1700307https://www.science.org/doi/10.1126/sciadv.1700307.

[167] K. J. Choi, M. Biegalski, Y. L. Li, A. Sharan, J. Schubert, R. Uecker, P. Reiche, Y. B. Chen, X. Q. Pan, V. Gopalan, et al., Science (New York, N.Y.) **306**, 1005 (2004), ISSN 1095-9203, URL http://www.ncbi.nlm.nih.gov/pubmed/15528439.

[168] O. Diéguez, S. Tinte, A. Antons, C. Bungaro, J. B. Neaton, K. M. Rabe, and D. Vanderbilt, Physical Review B **69**, 212101 (2004), ISSN 1098-0121, URL https://link.aps.org/doi/10.1103/PhysRevB.69.212101.

[169] N. A. Pertsev, A. G. Zembilgotov, and A. K. Tagantsev, Physical Review Letters **80**, 1988 (1998), ISSN 0031-9007, URL https://link.aps.org/doi/10.1103/PhysRevLett.80.1988.

[170] P. Sellappan, C. Tang, J. Shi, and J. E. Garay, Materials Research Letters **5**, 41 (2017), ISSN 2166-3831, URL https://www.tandfonline.com/doi/full/10.1080/21663831.2016.1195779.

[171] Y. Miyatake, M. Yamamoto, J. J. Kim, M. Toyonaga, and O. Nagai, Journal of Physics C: Solid State Physics **19**, 2539 (1986), ISSN 0022-3719, URL http://stacks.iop.org/0022-3719/19/i=14/a=020?key=crossref.f86923c3c4fa08f2c90e72760e86102e.

[172] G. P. Espinosa, The Journal of Chemical Physics **37**, 2344 (1962), ISSN 0021-9606, URL http://aip.scitation.org/doi/10.1063/1.1733008.

[173] Y. Ma and C. Cen, APS March Meeting 2019, abstract id.R40.013 (2019), URL http://adsabs.harvard.edu/abs/2019APS..MARR40013.

[174] Y. Hirata, D.-H. Kim, T. Okuno, T. Nishimura, D.-Y. Kim, Y. Futakawa, H. Yoshikawa, A. Tsukamoto, K.-J. Kim, S.-B. Choe, et al., Physical Review B **97**, 220403(R) (2018), ISSN 2469-9950, URL https://journals.aps.org/prb/pdf/10.1103/PhysRevB.97.220403https://link.aps.org/doi/10.1103/PhysRevB.97.220403.

[175] K.-J. Kim, S. K. Kim, Y. Hirata, S.-H. Oh, T. Tono, D.-H. Kim, T. Okuno, W. S. Ham, S. Kim, G. Go, et al., Nature Materials **16**, 1187 (2017), ISSN 1476-1122, URL http://www.nature.com/doifinder/10.1038/nmat4990.

[176] S. A. Siddiqui, J. Han, J. T. Finley, C. A. Ross, and L. Liu, Physical Review Letters **121**, 057701 (2018), ISSN 0031-9007, URL https://link.aps.org/doi/10.1103/PhysRevLett.121.057701.

[177] W. J. Takei, R. R. Heikes, and G. Shirane, Physical Review **125**, 1893 (1962), ISSN 0031-899X, URL https://journals.aps.org/pr/abstract/10.1103/PhysRev.125.1893https://link.aps.org/doi/10.1103/PhysRev.125.1893.

[178] S. Isogami, K. Masuda, and Y. Miura, Physical Review Materials **4**, 014406 (2020), ISSN 2475-9953, URL https://journals.aps.org/prmaterials/abstract/10.1103/PhysRevMaterials.4.014406https://link.aps.org/doi/10.1103/PhysRevMaterials.4.014406.

[179] Y. Yasutomi, K. Ito, T. Sanai, K. Toko, and T. Suemasu, Journal of Applied Physics **115**, 17A935 (2014), ISSN 0021-8979, URL http://aip.scitation.org/doi/10.1063/1.4867955.

[180] A. Foley, J. Corbett, A. Khan, A. L. Richard, D. C. Ingram, A. R. Smith, L. Zhao, J. C. Gallagher, and F. Yang, Journal of Magnetism and Magnetic Materials **439**, 236 (2017), ISSN 03048853, URL https://linkinghub.elsevier.com/retrieve/pii/S0304885317301610.

[181] T. Gushi, M. Jovic, J. Pen, S. Ghosh, J.-P. Attane, H. Okuno, O. Fruchart, J. Vogel, T. Suemasu, S. Pizzini, et al., Nano Lett **19**, 22 (2019), URL https://pubs.acs.org/sharingguidelines.

[182] T. Hirose, T. Komori, T. Gushi, A. Anzai, K. Toko, and T. Suemasu, AIP Advances **10**, 025117 (2020), ISSN 2158-3226, URL http://aip.scitation.org/doi/10.1063/1.5141818.

[183] X. Shen, A. Chikamatsu, K. Shigematsu, Y. Hirose, T. Fukumura, and T. Hasegawa, Applied Physics Letters **105**, 072410 (2014), ISSN 0003-6951, URL http://aip.scitation.org/doi/10.1063/1.4893732.

[184] W. Zhou, C. T. Ma, T. Q. Hartnett, P. V. Balachandran, and S. J. Poon, AIP Advances **11**, 015334 (2021), ISSN 2158-3226, URL http://aip.scitation.org/doi/10.1063/5.0032167.

[185] K. Ito, Y. Yasutomi, K. Kabara, T. Gushi, S. Higashikozono, K. Toko, M. Tsunoda, and T. Suemasu, AIP Advances **6**, 056201 (2016), ISSN 2158-3226, URL http://aip.scitation.org/doi/10.1063/1.4942548.

[186] H. Nakamura, D. Huang, J. Merz, E. Khalaf, P. Ostrovsky, A. Yaresko, D. Samal, and H. Takagi, Nature Communications **11**, 1161 (2020), ISSN 2041-1723, URL https://doi.org/10.1038/s41467-020-14900-1http://www.nature.com/articles/

s41467-020-14900-1.

[187] T. He, Q. Huang, A. P. Ramirez, Y. Wang, K. A. Regan, N. Rogado, M. A. Hayward, M. K. Haas, J. S. Slusky, K. Inumara, et al., Nature **411**, 54 (2001), ISSN 00280836, URL www.nature.com.

[188] R. Yu, H. Weng, Z. Fang, X. Dai, and X. Hu, Physical Review Letters **115**, 036807 (2015), ISSN 10797114, 1504.04577, URL https://journals.aps.org/prl/abstract/10.1103/PhysRevLett.115.036807.

[189] Y. Sun, X. Q. Chen, S. Yunoki, D. Li, and Y. Li, Physical Review Letters **105**, 216406 (2010), ISSN 00319007, URL https://journals.aps.org/prl/abstract/10.1103/PhysRevLett.105.216406.

[190] W. F. Goh and W. E. Pickett, Physical Review B **97**, 035202 (2018), ISSN 24699969, 1710.10716, URL https://journals.aps.org/prb/abstract/10.1103/PhysRevB.97.035202.

[191] S. Woo, K. M. Song, X. Zhang, Y. Zhou, M. Ezawa, X. Liu, S. Finizio, J. Raabe, N. J. Lee, S.-I. Kim, et al., Nature Communications **9**, 959 (2018), ISSN 2041-1723, 1703.10310, URL www.nature.com/naturecommunicationshttp://www.nature.com/articles/s41467-018-03378-7.

[192] Y. Quessab, J.-W. Xu, C. T. Ma, W. Zhou, G. A. Riley, J. M. Shaw, H. T. Nembach, S. J. Poon, and A. D. Kent, Scientific Reports **10**, 7447 (2020), ISSN 2045-2322, URL https://doi.org/10.1038/s41598-020-64427-0http://www.nature.com/articles/s41598-020-64427-0.

[193] T. Garel and S. Doniach, Physical Review B **26**, 325 (1982), ISSN 01631829, URL https://journals.aps.org/prb/abstract/10.1103/PhysRevB.26.325.

[194] N. Nagaosa and Y. Tokura, *Topological properties and dynamics of magnetic skyrmions* (2013), URL www.nature.com/naturenanotechnology.

[195] C. Xu, B. Xu, B. Dupé, and L. Bellaiche, Physical Review B **99**, 104420 (2019), ISSN 2469-9950, URL https://link.aps.org/doi/10.1103/PhysRevB.99.104420.

[196] M. Hestenes and E. Stiefel, Journal of Research of the National Bureau of Standards **49**, 409 (1952), ISSN 0091-0635.

[197] T. Okubo, S. Chung, and H. Kawamura, Physical Review Letters **108**, 017206 (2012), ISSN 0031-9007, 1109.6161, URL https://journals.aps.org/prl/abstract/10.1103/PhysRevLett.108.017206https://link.aps.org/doi/10.1103/PhysRevLett.108.017206.

[198] Z. Zhang, Y. Cho, M. Gong, S.-T. Ho, J. Singhal, J. Encomendero, X. Li, H. Lee, H. G. Xing, and D. Jena, IEEE Transactions on Magnetics pp. 1–1 (2021), ISSN 0018-9464, URL https://ieeexplore.ieee.org/document/9446920/.

[199] T. Komori, T. Hirose, T. Gushi, K. Toko, a. Hanashima, L. Vila, J.-P. Attanè,

K. Amemiya, and T. Suemasu, Journal of Applied Physics **127**, 043903 (2020), ISSN 0021-8979, URL https://aip.scitation.org/doi/abs/10.1063/1.5128635http://aip.scitation.org/doi/10.1063/1.5128635.

[200] H. Mitarai, T. Komori, T. Hirose, K. Ito, S. Ghosh, S. Honda, K. Toko, L. Vila, J.-P. Attané, K. Amemiya, et al., Physical Review Materials **4**, 094401 (2020), ISSN 2475-9953, URL https://journals.aps.org/prmaterials/abstract/10.1103/PhysRevMaterials.4.094401https://link.aps.org/doi/10.1103/PhysRevMaterials.4.094401.

[201] M. Mekata, Journal of the Physical Society of Japan **17**, 796 (1962), ISSN 0031-9015, URL https://journals.jps.jp/doi/abs/10.1143/JPSJ.17.796https://journals.jps.jp/doi/10.1143/JPSJ.17.796.

[202] T. Tanigaki, K. Shibata, N. Kanazawa, X. Yu, Y. Onose, H. S. Park, D. Shindo, and Y. Tokura, Nano Letters **15**, 5438 (2015), ISSN 1530-6984, URL https://pubs.acs.org/sharingguidelineshttps://pubs.acs.org/doi/10.1021/acs.nanolett.5b02653.

[203] Y. Fujishiro, N. Kanazawa, T. Nakajima, X. Z. Yu, K. Ohishi, Y. Kawamura, K. Kakurai, T. Arima, H. Mitamura, A. Miyake, et al., Nature Communications **10**, 1059 (2019), ISSN 2041-1723, URL https://doi.org/10.1038/s41467-019-08985-6http://www.nature.com/articles/s41467-019-08985-6.

[204] B. Berg and M. Lüscher, Nuclear Physics, Section B **190**, 412 (1981), ISSN 05503213.

[205] C. Xu, P. Chen, H. Tan, Y. Yang, H. Xiang, and L. Bellaiche, Physical Review Letters **125**, 037203 (2020), ISSN 10797114, URL https://journals.aps.org/prl/abstract/10.1103/PhysRevLett.125.037203.

[206] J. Seidel, *Nanoelectronics based on topological structures* (2019), URL https://doi.org/10.1038/s41563-019-0301-z.

[207] K. Everschor-Sitte, J. Masell, R. M. Reeve, and M. Kläui, Journal of Applied Physics **124**, 240901 (2018), ISSN 10897550, URL https://doi.org/10.1063/1.5048972.

[208] A. K. Nayak, V. Kumar, T. Ma, P. Werner, E. Pippel, R. Sahoo, F. Damay, U. K. Rößler, C. Felser, and S. S. Parkin, Nature **548**, 561 (2017), ISSN 14764687, URL https://www.nature.com/articles/nature23466.

[209] N. Gao, S. G. Je, M. Y. Im, J. W. Choi, M. Yang, Q. Li, T. Y. Wang, S. Lee, H. S. Han, K. S. Lee, et al., Nature Communications **10**, 1 (2019), ISSN 20411723, URL https://doi.org/10.1038/s41467-019-13642-z.

[210] B. Göbel, I. Mertig, and O. A. Tretiakov, *Beyond skyrmions: Review and perspectives of alternative magnetic quasiparticles* (2021), 2005.01390.

[211] C. Xu, J. Feng, S. Prokhorenko, Y. Nahas, H. Xiang, and L. Bellaiche, Physical Review B **101**, 060404(R) (2020), ISSN 2469-9950, 1906.04336, URL https://journals.aps.org/prb/abstract/10.1103/PhysRevB.101.060404https:

//link.aps.org/doi/10.1103/PhysRevB.101.060404.

[212] B. Dupé, M. Hoffmann, C. Paillard, and S. Heinze, Nature Communications **5**, 4030 (2014), ISSN 2041-1723, URL www.nature.com/naturecommunicationshttp://www.nature.com/articles/ncomms5030.

[213] Y. Zhang, C. Xu, P. Chen, Y. Nahas, S. Prokhorenko, and L. Bellaiche, Physical Review B **102**, 241107(R) (2020), ISSN 2469-9950, URL https://journals.aps.org/prb/abstract/10.1103/PhysRevB.102.241107https://link.aps.org/doi/10.1103/PhysRevB.102.241107.

[214] A. O. Leonov and M. Mostovoy, Nature Communications **6**, 8275 (2015), ISSN 2041-1723, 1501.02757, URL www.nature.com/naturecommunicationshttp://www.nature.com/articles/ncomms9275.

[215] S.-Z. Lin and S. Hayami, Physical Review B **93**, 064430 (2016), ISSN 2469-9950, 1512.05012, URL https://journals.aps.org/prb/abstract/10.1103/PhysRevB.93.064430https://link.aps.org/doi/10.1103/PhysRevB.93.064430.

[216] S. Hayami, S.-Z. Lin, and C. D. Batista, Physical Review B **93**, 184413 (2016), ISSN 2469-9950, 1601.02064, URL https://journals.aps.org/prb/abstract/10.1103/PhysRevB.93.184413https://link.aps.org/doi/10.1103/PhysRevB.93.184413.

[217] S.-Z. Lin and C. D. Batista, Physical Review Letters **120**, 077202 (2018), ISSN 0031-9007, 1707.05818, URL https://journals.aps.org/prl/abstract/10.1103/PhysRevLett.120.077202https://link.aps.org/doi/10.1103/PhysRevLett.120.077202.

[218] T. Shimokawa, T. Okubo, and H. Kawamura, Physical Review B **100**, 224404 (2019), ISSN 2469-9950, 1902.01582, URL https://journals.aps.org/prb/abstract/10.1103/PhysRevB.100.224404https://link.aps.org/doi/10.1103/PhysRevB.100.224404.

[219] R. Ozawa, S. Hayami, and Y. Motome, Physical Review Letters **118**, 147205 (2017), ISSN 0031-9007, URL https://journals.aps.org/prl/abstract/10.1103/PhysRevLett.118.147205http://link.aps.org/doi/10.1103/PhysRevLett.118.147205.

[220] T. Kurumaji, T. Nakajima, M. Hirschberger, A. Kikkawa, Y. Yamasaki, H. Sagayama, H. Nakao, Y. Taguchi, T.-h. Arima, and Y. Tokura, Science **365**, 914 (2019), ISSN 0036-8075, 1805.10719, URL http://science.sciencemag.org/https://www.sciencemag.org/lookup/doi/10.1126/science.aau0968.

[221] N. D. Khanh, T. Nakajima, X. Yu, S. Gao, K. Shibata, M. Hirschberger, Y. Yamasaki, H. Sagayama, H. Nakao, L. Peng, et al., Nature Nanotechnology **15**, 444 (2020), ISSN 1748-3387, 2003.00626, URL https://doi.org/10.1038/s41565-020-0684-7http://www.nature.com/articles/s41565-020-0684-7.

[222] K. Aoyama and H. Kawamura, Physical Review B **103**, 014406 (2021), ISSN 2469-9950, 2012.14515, URL https://journals.aps.org/prb/abstract/10.1103/PhysRevB.103.014406https://link.aps.org/doi/10.1103/PhysRevB.103.014406.

[223] J. Z. Sun, Physical Review B **62**, 570 (2000), ISSN 0163-1829, URL https://journals.aps.org/prb/abstract/10.1103/PhysRevB.62.570https://link.aps.org/doi/10.1103/PhysRevB.62.570.

[224] T. Taniguchi, S. Mitani, and M. Hayashi, Physical Review B **92**, 024428 (2015), ISSN 1098-0121, URL https://journals.aps.org/prb/abstract/10.1103/PhysRevB.92.024428https://link.aps.org/doi/10.1103/PhysRevB.92.024428.

[225] L. Liu, C. F. Pai, Y. Li, H. W. Tseng, D. C. Ralph, and R. A. Buhrman, Science **336**, 555 (2012), ISSN 10959203, 1203.2875, URL www.sciencemag.orgsciencevolhttp://science.sciencemag.org/.